The Dissertation Committee for Jinhong Shin Certifies that this is the approved version of the following dissertation:

Growth and Characterization of CVD Ru and Amorphous Ru-P Alloy Films for Liner Application in Cu Interconnect.

Committee:

John G. Ekerdt, Supervisor

Sanjay K. Banerjee

Paul S. Ho

Brian A. Korgel

Charles B. Mullins

Growth and Characterization of CVD Ru and Amorphous Ru-P Alloy Films for Liner Application in Cu Interconnect.

by

Jinhong Shin, B. S.; M. S.

Dissertation

Presented to the Faculty of the Graduate School of
The University of Texas at Austin
in Partial Fulfillment
of the Requirements
for the Degree of

Doctor of Philosophy

The University of Texas at Austin
December, 2007

Dedication

To my Parents and Sisters.

Acknowledgements

I would like to express my very best gratitude to my advisor, Prof. J. G.. Ekerdt, for guiding and encouraging me throughout the past four years in the university. I was impressed not only by his scientific and technological knowledge and insight, but also by his positive attitude confronting problems, willingness to help students, and sincerity. It was also my great pleasure to have a chance to work with Prof. J. M. White. I remember him not only as a distinguished scientist, but also as a person with great personality and energy. I also would like to appreciate Prof. R. A. Jones for synthesizing and providing us a number of great novel compounds. I also thank Prof. G. S. Hwang for his insightful advice and support on the computational analysis. A very special thank goes out for Dr. Yang-Ming Sun who helped me with his profound knowledge and experience on UHV systems and surface science. Without his pivotal advice, my chambers would have remained down forever. I also thank to Dr. Ji-Ping Zhou for training and helping me with TEM analysis.

I owe my gratitude to all of former and present colleagues in the Ekerdt and White groups for their various forms of support and personal kindness during my graduate study. I am especially grateful to Hyunwoo Kim for his valued simulation work that offered important theoretical background and insight for my experiments. He contributed to the several papers published and the chapters in this dissertation. I appreciate Wyatt

Winkenwerder for his surface science study that also contributed to a paper and this dissertation. I also specially thank Luke Henderson for his work and help. And, I appreciate Abdul Waheed and Kyriacos Agapiou for synthesizing and providing precursors. I also would like to extend my gratitude to all of my friends in U.S. and Korea.

Finally and most of all, I wish to express my deepest appreciation for my parents Samkyu Shin and Sookja Yoon for their dedicated support and constant encouragement throughout whole of my life. I also truly thank my older sisters, Sanghee Shin and Sunghee Shin, for their warm-heated care and inspiration. They all made me overcome difficult days, stay confident in myself, and be focused on my graduate study. I dedicate this work to my family.

Growth and Characterization of CVD Ru and Amorphous Ru-P Alloy Films for Liner Application in Cu Interconnect.

Publication No.______________

Jinhong Shin, Ph.D.
The University of Texas at Austin, 2007

Supervisor: John G. Ekerdt

Copper interconnect requires liner materials that function as a diffusion barrier, a seed layer for electroplating, and an adhesion promoting layer. Ruthenium has been considered as a promising liner material, however it has been reported that Ru itself is not an effective Cu diffusion barrier due to its microstructure, which is polycrystalline with columnar grains. The screening study of Ru precursors revealed that all Ru films were polycrystalline with columnar structure, and, due to its strong 3D growth mode, a conformal and ultrathin Ru film was difficult to form, especially on high aspect ratio features.

The microstructure of Ru films can be modified by incorporating P. Amorphous Ru(P) films are formed by chemical vapor deposition at 575 K using a single source precursor, *cis*-$RuH_2(P(CH_3)_3)_4$, or dual sources, $Ru_3(CO)_{12}$ and $P(CH_3)_3$ or $P(C_6H_5)_3$.

The films contain Ru and P, which are in zero-valent states, and C as an impurity. Phosphorus dominantly affects the film microstructure, and incorporating > 13% P resulted in amorphous Ru(P) films. Metastable Ru(P) remains amorphous after annealing at 675 K for 3 hr, and starts recrystallization at ~775 K. The density of states analysis of the amorphous Ru(P) alloy illustrates metallic character of the films, and hybridization between Ru 4d and P 3p orbitals, which contributes to stabilizing the amorphous structure. Co-dosing $P(CH)_3$ with $Ru_3(CO)_{12}$ improves film step coverage, and the most conformal Ru(P) film is obtained with *cis*-$RuH_2(P(CH_3)_3)_4$; a fully continuous 5 nm Ru(P) film is formed within 1 μm deep, 8:1 aspect ratio trenches. First principles density functional theory calculations illustrate degraded Cu/Ru adhesion by the presence of P at the interface, however, due to the strong Ru-Cu bonds, amorphous Ru(P) forms a stronger interface with Cu than Ta and TaN do. Cu diffusion studies at 575 K suggests improved barrier property of amorphous Ru(P) films over polycrystalline PVD Ru.

Table of Contents

List of Tables

List of Figures

List of Illustrations

Chapter 1

Introduction

1.1 OVERVIEW

Since the first creation of an integrated circuit in 1958, the density and performance of microelectronic devices have steadily improved. In 1965, Moore projected that the complexity on an integrated circuit would double approximately every 24 months, which is widely known as Moore's Law [1]. The complexity of devices can be accepted as the number of transistors, the functionality of integrated circuits, or simply the technology node of microelectronic devices. Although it was initially made in the form of an observation and forecast, it has served as a goal for the entire semiconductor industry. For decades, there have been innovations in architecture, manufacturing processes, and materials to improve the functionality and density of the integrated circuits. Included among these are significant innovations in the interconnect, which connects transistors and delivers electrical signal and power. The interconnect is composed of conductive wires and insulating dielectric materials, and, due to the complexity of circuits, the interconnect has multiple layers depending on the device and the technology node. Traditionally, device performance was improved by scaling down the gate length, gate dielectric thickness, and junction depth; and until recently, the interconnect had little impact on the overall device performance. However, continuous feature size scaling and increases in total wiring length due to higher device density brought attention to several issues in the interconnect, such as resistance-capacitance (RC) delay, crosstalk, and power dissipation.

One of the major concerns is the signal delay in interconnects associated with increased RC parasitics. Interconnect related RC delay can be projected using a simple model shown in Illustration 1.1 [2]. Assuming the minimum metal pitch is twice the metal width (W) and the dielectric thickness between metal lines is the same as the metal height (T), the following equation can be used to calculate the RC. L and P denote total line length and pitch, respectively.

$$R = 2\rho L / PT \tag{1.1}$$

$$C = 2\varepsilon\varepsilon_0 (2LT / P + LP / 2T) \tag{1.2}$$

$$RC = 2\rho\varepsilon\varepsilon_0 (4L^2 / P^2 + L^2 / T^2) \tag{1.3}$$

Continuous scaling down of devices to achieve higher density leads to a decrease in P and T, resulting in increased RC delay in the interconnects. Device performance improvement requires more transistors and functional groups, which also degrades the RC property due to longer wires. Since local and intermediate wiring are usually short in length, RC delay is largely determined by the global wiring that connects functional

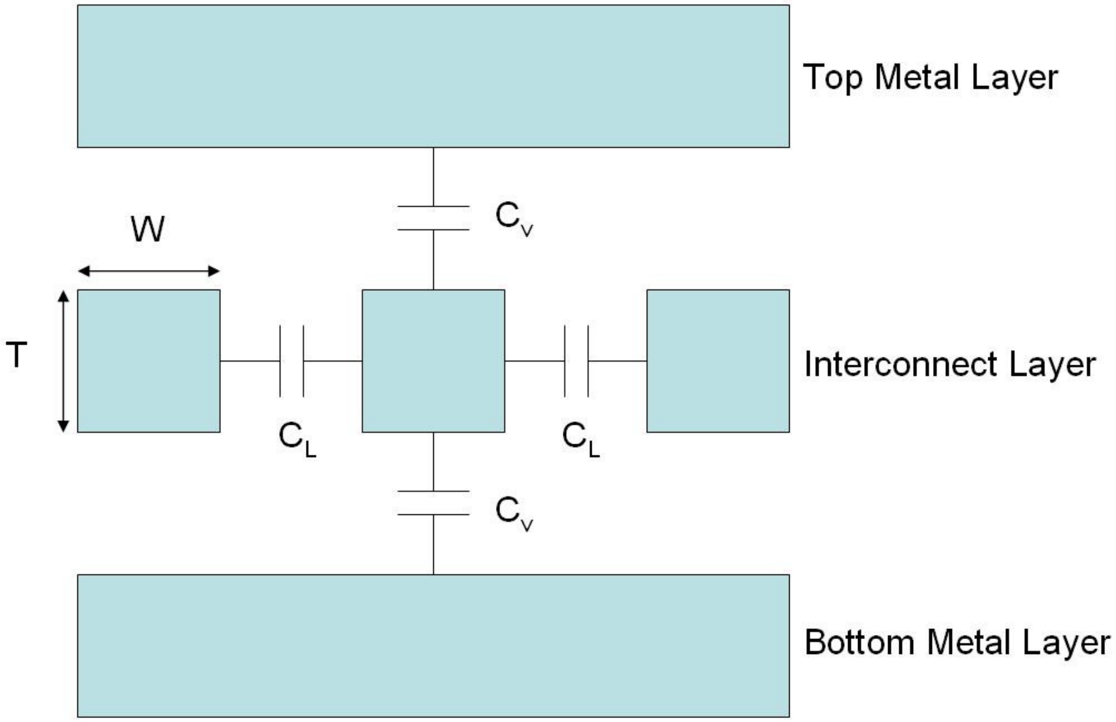

Illustration 1.1   Interconnect system cross-section with parasitic capacitances [2].

blocks. Traditionally, signal delay in transistors has had a dominant impact on operating speed; however, interconnect related RC delay becomes the limiting factor in the technology nodes below 0.25 μm, as shown in Figure 1.1 [3]. While the RC delay can be reduced by employing reverse scaling or repeaters accompanying a larger chip size or more metal levels, the RC delay issue was mitigated by using Cu and low-k dielectrics instead of Al and SiO_2. Equation 1.3 shows that the RC delay can be suppressed by lowering the resistivity of the conductive lines and the dielectric constant of the insulating materials. Cu is an attractive substitute for Al due to its lower electrical resistivity (ρ_{Cu}=1.7 μΩ·cm and ρ_{Al}=2.8 μΩ·cm), and it also offers higher intrinsic electromigration resistance. Several low-k materials have been studied, however SiO_2 based dielectrics have attracted the most interest because of their robust physical and electrical properties. Fluorinated silicate glass (FSG) was the first low-k material, but it offers only slight advantages over undoped silicate glass (USG) due to its k value (k_{FSG}=3.4 – 4.1 and k_{USG}=4.0 – 4.2). In recent years, organosilicate glasses (OSG), which achieves k values less than 3.0 by introducing C and pores to make a microscopically and macroscopically loose structure, were most widely used as the low-k material. In order to lower the total effective capacitance of the interconnect, materials with high k values, like Si_3N_4, were substituted with lower k materials, like SiC_xN_y, or were removed completely. By adopting Cu and low-k material instead of Al and SiO_2, an increase in the RC delay can be dramatically suppressed as shown in Figure 1.1.

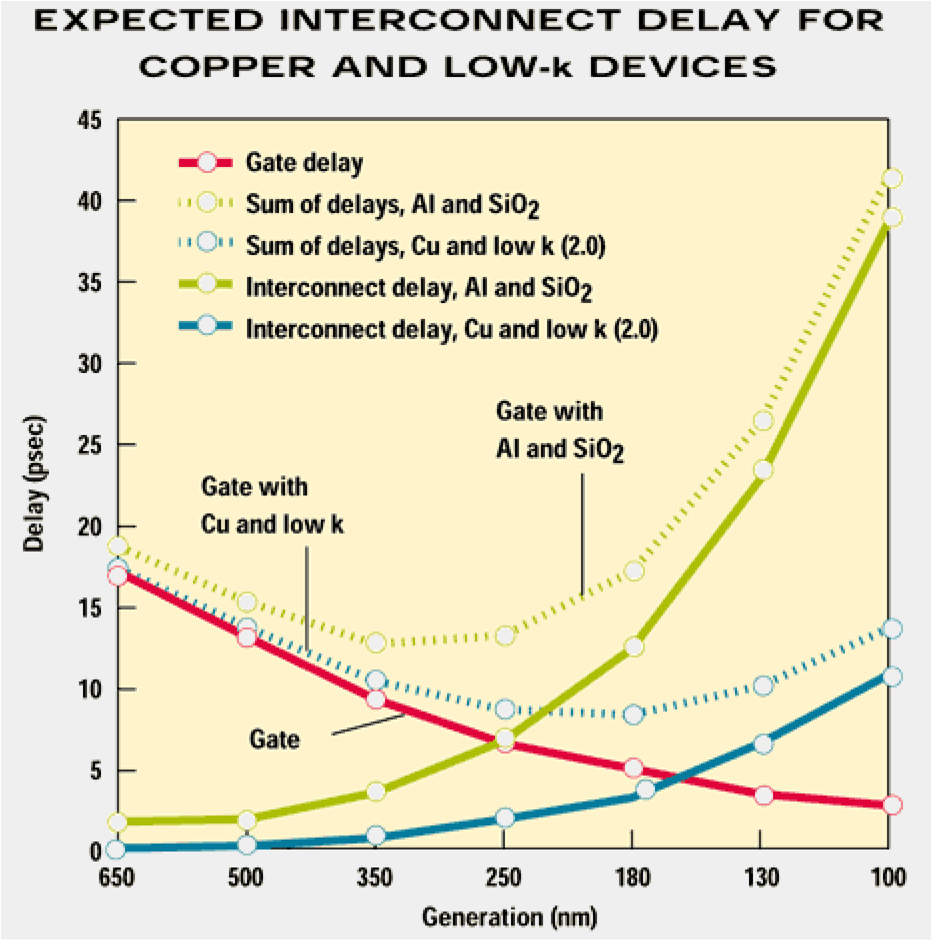

Figure 1.1 Decrease in interconnect delay and improved performance are achieved using Cu and low-k dielectric [3].

Additional performance issues for the interconnect include signal crosstalk and power dissipation. Crosstalk and noise become increasingly important as transistor operating voltage continues to decrease. Unlike the RC delay, signal crosstalk exhibits more impact on the local and intermediate wires rather than the global wires due to their tight line spacing, and is dominated by interconnect sidewall capacitance. Dynamic power consumption due to the periodic switching of capacitors is the main component of the power dissipation, and it is known to follow the relation shown in Equation 1.4 [4].

$$P \propto C \cdot V^2 \cdot f \tag{1.4}$$

where C is capacitance, V is the supply voltage, and *f* is the clock frequency. Lower capacitance can reduce both signal crosstalk and power dissipation, which is achievable by using low-k material or reducing metal height. The later approach can increase RC delay and joule heating due to the higher line resistance, but Cu can mitigate this problem with its higher electrical conductivity.

1.2 BACKGROUND

1.2.1 Cu Interconnect

Implementing Cu brought major changes in the backend of line (BEOL) process of integrated devices. Historically, conductive lines were formed by etching patterned conductive materials like Si- and Cu-doped Al alloy; however, Cu is not easily removable because its etching byproducts are nonvolatile. Some plasma etching systems were developed for Cu etching, but they were not adopted due to their complexity and residue issues of the processes. Instead, the dual damascene process became a mainstream scheme for Cu interconnect. In the damascene process, dielectric films, such as inter-metal dielectrics (IMD), etch stop layers, and dielectric diffusion barriers, are deposited first as blanket films followed by patterning and etching, leaving vias and trenches. These are filled with Cu by electroplating, followed by removal of extra Cu with chemical mechanical polishing (CMP). Dual damascene denotes that via and trench are formed together in single steps of metal deposition and CMP, which provides advantages not only in cost with fewer process steps, but also in the performances by way of lower via resistance and improved reliability.

Illustration 1.2 presents a cross-section of Cu implemented in a dual damascene structure. While Cu offers several advantages, it readily migrates into Si, SiO_2, and low-k dielectrics, especially under an electric field. Cu migration can cause highly adverse effects like increased leakage current, formation of deep trapping levels in Si, and silicide formation, which will cause serious device degradation and failure. In order to prevent these problems, Cu needs to be encapsulated with diffusion barriers as shown in Illustration 1.2.

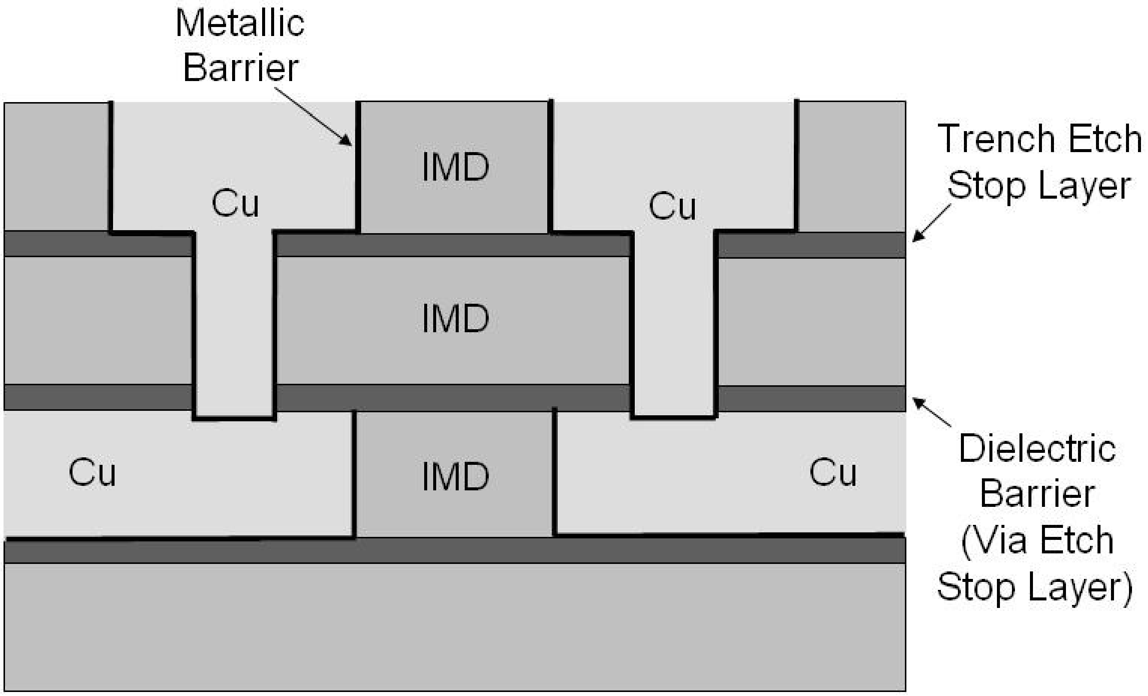

Illustration 1.2 The cross-section of Cu implemented dual damascene structure.

Diffusion barriers can be categorized as metallic and dielectric barriers. Metallic barriers are formed before Cu electroplating, and dielectric diffusion barriers are formed after Cu CMP. Generally, metallic barriers are implemented as a stack, which is frequently called a liner. A liner includes an adhesion promoting layer, which improves adhesion between dielectric film and metallic films, a metallic diffusion barrier that blocks Cu diffusion, and a seed layer, which act as an electrode for Cu electroplating. Plasma enhanced chemical vapor deposition (PE-CVD) Si_3N_4 that blocks Cu penetration effectively was previously used as the dielectric diffusion barrier. However, it has been substituted with PE-CVD SiC_xN_y or SiC_x films to reduce the total capacitance of the interconnects (k_{Si3N4}= ~7, k_{SiCxNy}= ~5, and k_{SiCx} <5) [5,6]. Attempts to replace it with a further lower k material are being made, however issues like etch selectivity, adhesion with both low-k and Cu, and film stability need to be resolved. Especially, since the interface between the dielectric barrier and Cu is reported to be the fastest path for Cu electromigration, forming a strong interface is essential for high electromigration resistance [7]. Hu et al. showed the importance of the dielectric barrier-Cu interface and a process that can improve the interface and electromigration lifetime by the deposition of electroless CoW_xP_y on Cu [8].

1.2.2 Metallic Barriers

The metallic Cu diffusion barrier has larger contact area with Cu than the dielectric barrier, and should satisfy the following critical requirements: (a) it should be able to effectively block Cu penetration, (b) it must be stable, and should not form a compound either with Cu or a dielectric film, (c) low electrical resistivity is desirable to keep Cu line resistance low, (d) good adhesion with both Cu and dielectric films are also needed, (e) no damage to low-k materials is allowed during the deposition process, and (f) a thin and conformal film with good step coverage is needed.

Various barrier materials have been studied, which include refractory metals (Ta, W, and Co), refractory metallic alloys (TiW_x, FeW_x, and $NiMo_x$), refractory metal-silicon alloys ($TiSi_2$, $TaSi_2$, and $CoSi_2$), refractory metal compounds (TiN_x, TaN_x, and WC_x), and refractory metal based ternary compounds (WC_xN_y, $TiSi_xN_y$, and WSi_xN_y) [9]. Most of the studied materials are based on refractory metals because of their high meting point, low diffusivity, and high chemical stability. In recent years, Ta and TaN were most widely used for metallic diffusion barriers due to their superior physical, chemical, and electrical properties. Ta is a refractory metal having a high meting point of 3290 K, and it almost completely immiscible with Cu. Ta films can be grown by physical vapor deposition (PVD) and CVD, and the films are polycrystalline having either bcc α-Ta or tetragonal β-Ta phases. Bulk Ta usually crystallizes in the α phase, however Ta films grown on SiO_2 are known to feature the β phase. The α phase is preferred due to its lower electrical resistivity ($\rho_{\alpha\text{-Ta}}$ = 20 – 30 μΩ·cm and $\rho_{\beta\text{-Ta}}$ = ~180 μΩ·cm), and studies show that Ta can be forced to grow in the α phase by using different substrates or applying surface treatments with the plasma [10,11]. Holloway et al. reported that 50 nm PVD Ta prevented Cu diffusion up to 825 K for 30 min in He [12]. Bias thermal stress (BTS) test performed by Bai et al. showed that 30 nm PVD Ta effectively block Cu diffusion, and over 100 years of mean time to failure (MTTF) was obtained under the 475 K and 0.1 MV/cm condition, which is the typical operating condition of integrated circuits [13]. Ta-nitrides, TaN_x, can be formed by CVD, ALD, and PVD, and exist in various phases including Ta_2N, TaN, Ta_5N_6, Ta_4N_5, and Ta_3N_5, or mixtures of these phases. All phases are chemically stable with their high melting point and heat of formation. The structure of TaN_x depends on the composition and the phase of films, but can described as close-packed Ta atoms with N atoms in interstitial sites, resulting in considerably better barrier properties against Cu diffusion compared to Ta. Oku et al. reported that an 8 nm thick PVD TaN having disordered grain boundaries prevented Cu diffusion after annealing at 975 K for 30 min [14]. The Cu diffusion was controlled by grain boundary diffusion at low temperatures (875 – 1075 K) and bulk diffusion at high temperatures (1075 – 1175 K), and the activation energies for Cu diffusion were 1.3 eV and 2.7 eV, respectively. Compared to Ta, TaN_x has better adhesion with Si and SiO_2, however studies showed that Cu adhesion was less strong because of the presence of N bound to Ta weakening the Cu – Ta bonds at the interface [15]. Combining Ta and TaN_x offers several advantages in adhesion with both dielectric and Cu films, electromigration (EM) resistance, barrier property, and line resistance, and in recent years, TaN_x/Ta stacks are the most commonly used liners for Cu interconnects.

TaN_x/Ta stacks are typically grown with PVD due to its excellent film quality and the reliability of the process. As interconnect features migrate towards sub 100 nm structures, the thickness of liners is quickly decreasing. The International Technology Roadmap for Semiconductors (ITRS) projects the thickness of the barrier/cladding layers for 45 nm and 32 nm node main processing units (MPU) to be merely 3.3 nm and 2.4 nm, respectively [16]. Not only are the barrier capabilities of these thin layers questionable, but the step coverage of PVD films is also an extremely challenging issue even with recent ionized PVD and resputtering techniques. While PVD technologies are limited by its directional nature and the high sticking coefficient of deposited atoms, CVD and atomic layer deposition (ALD) are expected to offer superior step coverage and conformal films on high aspect ratio damascene structures [17]. Extensive studies have been performed on CVD and ALD TaN_x and Ta films such as, PE-CVD Ta with $TaBr_5$ and H_2 [18], PE-ALD Ta with $TaCl_5$ and H_2 [19], PE-CVD TaN with $TaBr_5$, H_2, and N_2 [20], and PE-ALD TaN_x with $TaCl_5$, H_2, and N_2 [21], and PE-ALD TaN_x with pentakis(diethylamino)Ta (PDEAT), H_2, and N_2 [22].

In recent years, Ru has been considered as a liner material in Cu interconnects because of its promising properties. The immiscibility of Ru with Cu and the lack of formation of any inter-metallic compounds make it a potential Cu diffusion layer. Ru is also an attractive material for a Cu seed layer due to its low resistivity, $\rho = 7.1\ \mu\Omega\cdot\mathrm{cm}$, chemical stability in both air and a Cu plating bath [23], and strong adhesion with Cu. The Ru-Cu interface shows ~ 4 times higher interface energy compared to the Ta-Cu interface ($E_{i,\mathrm{Ru-Cu}} = 3.17\ \mathrm{J/m^2}$ and $E_{i,\mathrm{Ta-Cu}} = 0.84\ \mathrm{J/m^2}$, assuming $\gamma_{\mathrm{Cu}(111)} = 1.83\ \mathrm{J/m^2}$), which results in higher activation energy for Cu migration and better EM resistance [24]. However, recent studies show that the barrier capability of Ru is quite suspect; a 20 nm Ru could prevent Cu diffusion up to 725 K, and a 5 nm Ru film lost its barrier property for Cu at temperatures only above 575 K [25,26]. It is now generally accepted that Ru alone may not be a viable Cu diffusion barrier, and using Ru as the Cu seed layer with Cu diffusion barriers like TaN_x or WN_x, is one likely technology solution [27]. Ruthenium films can be grown by CVD or ALD methods using precursors, such as Ru carbonyl ($Ru_3(CO)_{12}$) [28], cyclopentadienyl derivatives e.g., Cp_2Ru [29] or $(EtCp)_2Ru$ [30], and β-diketonates e.g., $Ru(thd)_3$ [31], ($Cp = \eta^5\text{-}C_5H_5$, $EtCp = \eta^5\text{-}C_5H_4Et$, thd = 2,2,6,6-tetramethyl-3,5- heptanedione). Ru films deposited by CVD or PVD methods follow a 3D, Vollmer-Weber growth mechanism, due to its high surface energy ($\gamma_{\mathrm{Ru}(001)} = 3.05\ \mathrm{J/m^2}$) [32] and this leads to polycrystalline, columnar films. The poor barrier properties of Ru films are attributed to this microstructure.

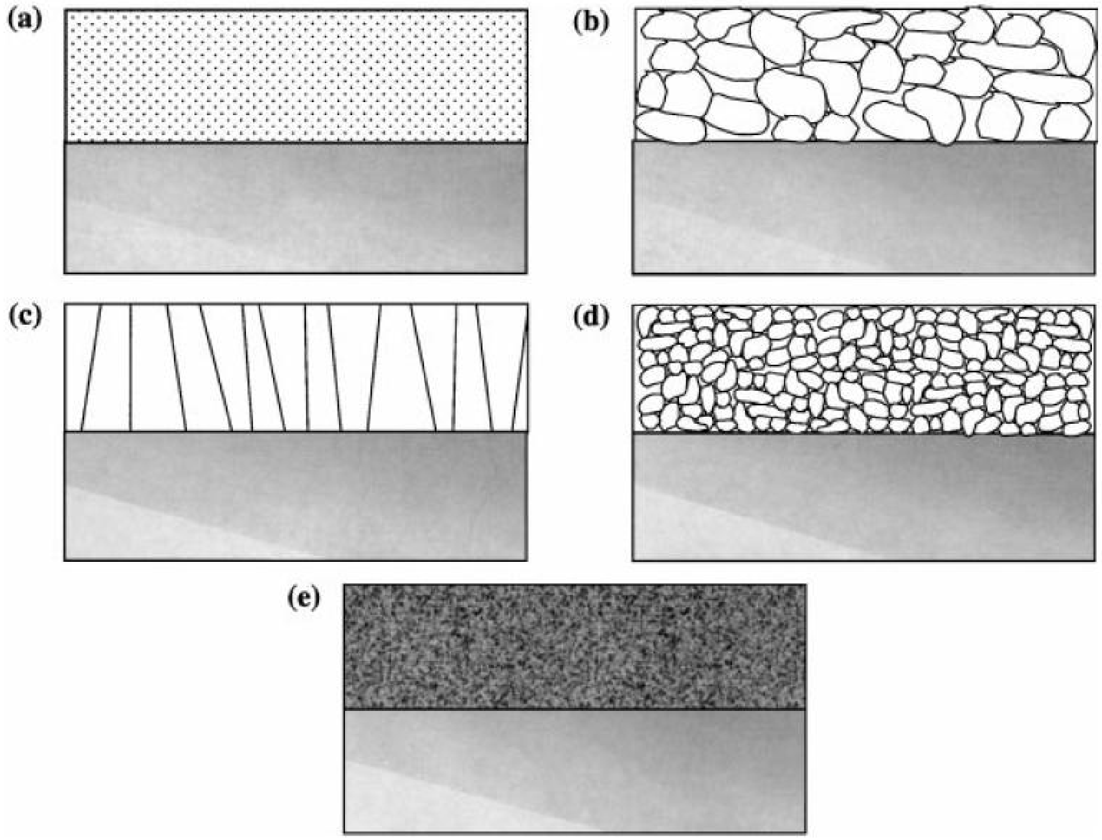

Illustration 1.3 Microstructure of thin films, (a) single crystal, (b) polycrystalline, (c) polycrystalline columnar, (d) nano-crystalline, and (e) amorphous [9].

1.2.3 Amorphous Metal Alloys

Film microstructure can be categorized as single crystal, polycrystalline, or amorphous, as shown in Illustration 1.3 [33]. Single crystal is ideal for the diffusion barrier because Cu diffusion can happen through defects like vacancies and dislocations; however, forming ultra thin single crystalline film on complex and small damascene structures is nearly impossible. The thermal budget, stress, and film stability can be additional problems. Since the grain boundaries in polycrystalline films act as fast paths for Cu diffusion, a polycrystalline microstructure is least desirable for diffusion barriers. The films with columnar structure have grain boundaries extending across the film perpendicularly, and show the worst barrier property due to the shorted diffusion length. The barrier property can be improved by forming nano-crystalline films, which have longer diffusion distances for Cu atoms to penetrate the barrier. Stuffing grain boundaries with impurities can also suppress Cu diffusion by blocking the fast diffusion path [34]. Amorphous microstructure is inherently most suited for barrier applications because of the absence of grain boundaries in the films.

Since the discovery of a metallic glass in the 1960s in $Au_{0.75}Si_{0.25}$ alloy [35], intensive experimental and theoretical efforts have been made to understand formation mechanisms, microstructure, and material properties. A metallic glass can be formed by diverse methods including rapid quenching from a liquid, condensation of vapors, solid state reaction, electron radiation, electrochemical deposition, and mold casting. Metallic glasses can largely be categorized into two groups, pure metallic alloys and metal – metalloid alloys, although many alloy systems recently reported have more complex compositions [36,37]. Generally, the formation of metallic glasses can be explained by a geometrical model based on the topological instabilities induced by atomic size differences among the glass forming elements. Egami et al. suggested that solid solutions having solute concentration above a certain level would not be stable due to the stress enveloped by atomic size difference, and would remain in liquid-like structures under a sufficiently rapid quenching rate [38,39]. It is also known that metallic glasses composed of multiple components having large atomic size differences and good mixing compatibility have high glass forming ability (GFA) [40]. Many bulk metallic glasses having superior GFA that can be formed with slow cooling have multiple alloying components, typically four or more, like $Mg_{54}Cu_{26.5}Ag_{8.5}Gd_{11}$ [41] and $Zr_{41.2}Ti_{13.8}Cu_{12.5}Ni_{10}Be_{22.5}$ [42]. In the case of metal-metalloid glasses, in addition to atomic size effects, chemical interaction between metal and metalloid atoms shows significant influence on the GFA, thermal stability, and short range order (SRO). The electronic structures of transition metal-metalloid glasses like NiP_x and CoP_x are found to be characterized by a relatively narrow transition metal d band close to the Fermi level and a strong bonding-antibonding splitting in the metalloid p band, indicating a strong covalent interaction [43]. Superior thermal stability and a wide range of glass forming compositions in transition metal-metalloid alloys with relatively simple binary or ternary systems are based on the stabilized SRO structure by the strong directional chemical bonding between the components [44,45].

1.3 OBJECTIVE AND OVERVIEW OF CHAPTERS

The objective of the work presented here is to form and characterize CVD Ru and amorphous Ru(P) films for liner applications in Cu interconnect. The precursor screening study reveals that all Ru films have columnar structure which is not suited for the Cu diffusion barrier (Chapter 2). The strong 3D mode growth of CVD Ru films leads to a rougher surface and a less continuous film compared to PVD Ru films (Chapter 3). The microstructure was modified by incorporating P, producing ultrathin and conformal amorphous Ru(P) films, from a single precursor (Chapter 4) and dual chemical sources (Chapter 5). The properties of amorphous Ru(P) films for the liner application are studied (Chapter 4-6). First principles calculations that complement the experiments were performed by Hyunwoo Kim of the G. S. Hwang group, and are included as an integral part of this dissertation since the majority of the chapters are based on journal papers that included both experimental and simulation results. Summarizing commentary and suggestions for future work are described in Chapter 7.

Chapter 2 describes the screening study on new Ru precursors for CVD and atomic layer deposition (ALD). The precursors examined include dodecacarbonyl-triruthenium (Ru-carbonyl), $Ru_3(CO)_{12}$, (η^6-benzene)(η^4-1,3-cyclohexadiene)ruthenium, $Ru(C_6H_6)(C_6H_8)$, (2,4-dimethyl-pentadienyl(ethylcyclopentadienyl)ruthenium (DER), $Ru(C_7H_{11})(C_7H_9)$, and bis(2,4-dimethylpentadienyl)ruthenium (DMPD), $Ru(C_7H_{11})_2$. Film composition, microstructure, surface morphology, step coverage, and suitability for ALD with H_2 are explored. CVD growth with $Ru_3(CO)_{12}$ at 475 K results in Ru films composed of columnar grains. Poor step coverage has been observed due to the high sticking coefficient of $Ru_3(CO)_{12}$, and either using lower substrate temperature (425 K) and co-dosing NH_3 do not improve the step coverage. $Ru(C_6H_6)(C_6H_8)$ starts to decompose to form Ru film at 450 K, and, compared to $Ru_3(CO)_{12}$, smoother films and improved step coverage are obtained due to its higher nucleation density. The DER precursor needs oxygen to form Ru films at 475 K. Film growth in the ALD mode with DER shows that the growth rate is too high for ALD (~1.2 nm/cycle) and is dependent on precursor dosing and purging times, leading to the conclusion that the actual growth mode is likely by CVD. The DMPD precursor starts decomposition at 475 K to form Ru films having hcp structure by X-ray diffraction (XRD) measurements. All films grown with the precursors in this study are polycrystalline Ru having columnar grains, which are not suited for the diffusion barrier application. No precursor shows self limiting adsorption behavior and reactivity with H_2, indicating that the precursors are not suitable for thermal ALD in a reducing atmosphere.

Chapter 3 presents Ru film growth by CVD and PVD on SiO_2 substrates with the goal of realizing ultrathin (< 5nm) and continuous films. CVD Ru films are grown from $Ru_3(CO)_{12}$ precursor at 425 – 525 K, and PVD Ru films are grown with a DC magnetron sputtering system at room temperature. Atomic force microscopy (AFM) reveals the CVD Ru films to have a rougher surface than PVD; RMS roughness of CVD and PVD Ru films are 1.43 nm and 0.11 nm, respectively. A surface coverage versus X-ray photoelectron spectroscopy (XPS) intensity study illustrate that CVD Ru follows strong 3D growth mode. The thickness for the thinnest continuous CVD Ru film on SiO_2 is determined to be ~20 nm by transmission electron microscopy (TEM) analysis. Film thickness and continuity established by XPS and low energy ion scattering spectroscopy (LEISS) shows considerable deviation form the TEM analysis result because of the shadowing effect of He^+ ions by columnar Ru grains during LEISS analysis.

In Chapter 4, chemical vapor deposition growth of amorphous Ru(P) films on SiO_2 containing ~15% P is described. *cis*-Dihydridotetrakis(trimethylphosphine)Ru(II), *cis*-$RuH_2(PMe_3)_4$ (Me = CH_3) was used at growth temperatures ranging from 525 to 575 K. X-ray photoelectron spectroscopy (XPS) shows Ru $3d_{5/2}$ and P $2p_{3/2}$ peaks at 280.0 and 129.8 eV, indicating that both Ru and P are in zero-valent states. The films contain ~10% C as an impurity. Amorphous microstructure of the Ru(P) films is determined by X-ray diffraction (XRD) and transmission electron microscopy (TEM). The films are metastable; remain amorphous upon heating for 3 hr at 675 K, and become increasingly more polycrystalline upon annealing to 775 and 975 K. The P content is related to the growth temperature, with more P found at higher substrate temperatures. Separate surface studies illustrate the trimethylphosphine ligands undergo demethylation and desorb at the growth conditions and readsorb, and subsequently incorporate the P into the Ru film. This also suggests the possibility of using separate Ru and P sources for amorphous Ru(P) film formation. A first principles molecular dynamics study shows that Ru(P) alloys with moderate P content can result in a glassy structure exhibiting the topological and strong chemical short-range order. In the $Ru_{80}P_{20}$ structure, the P-centered polyhedra prefer the tri-capped trigonal prism packing (TTP) phase with Veronoi index <0,3,6,0>. Phosphorus and its manner of incorporatation appear responsible for the amorphous-like character of CVD Ru(P) films.

Chapter 5 presents Ru(P) films grown from dual chemical sources, $Ru_3(CO)_{12}$ and $P(CH_3)_3$ or $P(C_6H_5)_3$ with flowing H_2 or Ar at 575 K. XPS analysis suggest Ru and P are in zero-valent states in Ru(P) films grown from both *cis*-$RuH_2(PMe_3)_4$ and dual chemical sources. The amount of P and C in Ru(P) films depends on the delivery gas and the alkylphoshphine source. Amorphous Ru(P) films as thin as 7 nm are grown on SiO_2 using $Ru_3(CO)_{12}$ and $P(CH_3)_3$ with H_2. The microstructure changed with the percentage P; amorphous films formed provided the percentage of P exceeded ~13%, in a C free basis. Film resistivity was most sensitive to the C impurity, and a 15 nm thick, amorphous film containing 11.2% P and 10.5% C shows a resistivity of 210 $\mu\Omega\cdot$cm. Ion scattering studies reveal that ~0.4 nm PVD Cu, which corresponds 2-3 atomic layers, completely wets amorphous Ru(P) alloy film surface. Density of states (DOS) analysis of the Ru(P) alloy reveals metallic character of the alloy and hybridization between Ru 4d and P 3p orbitals, which contributes to stabilizing the amorphous structure. First principles density functional calculations show Ru and P are intermixable, and predict the amorphous structure should be most stable above 20% P.

In Chapter 6, amorphous Ru(P) films grown at 575 K using a single source precursor, *cis*-$RuH_2(P(CH_3)_3)_4$, or dual sources, $Ru_3(CO)_{12}$ and $P(CH_3)_3$ or $P(C_6H_5)_3$ are studied to explore the effect of P on the film properties required for the liner application. Dosing $P(CH_3)_3$ with $Ru_3(CO)_{12}$ improves film step coverage by the reduced available adsorption sites for $Ru_3(CO)_{12}$, and the most conformal Ru(P) film is obtained with *cis*-$RuH_2(P(CH_3)_3)_4$. Fully continuous 5 nm Ru(P) film is formed within 1 μm deep, 8:1 aspect ratio trenches. Barrier performance is tested using Cu/Ru/Si(100) stacks annealed at 575 K, and sheet resistance was used as a measure of barrier failure. Cu diffusivity in PVD Ru is approximated to be 6.6×10^{-17} cm^2/s at 575 K, which indicates fast Cu diffusion along grain boundaries. While 26 nm polycrystalline PVD Ru failed after 6 hr annealing by Cu penetration, 28 nm amorphous Ru(P) survived after 67 hr annealing. Strong adhesion between Ru(P) and Cu films is observed in an annealing study with 10 nm Cu at 675 K, revealing adhesion strength in the order of Ru(P) alloy > PVD Ta > PVD TaN. First principles density functional calculations suggest 16.7% P degraded adhesion strength by 12% when compared to crystalline Cu/Ru, by the presence of P at the interface. However, due to the strong Ru-Cu bonds, amorphous Ru(P) still forms a stronger interface with Cu than do Ta and TaN to Cu, as observed when annealing 10 nm Cu films on these surfaces at 675 K. From the contact angle data reported and the DFT calculation in this study, adhesion energies of Cu/Ru(P), Cu/Ta, and Cu/TaN are approximated to be 2.59, 2.17, and 1.85 J/m^2, respectively, which are consistent with the annealing study result.

1.4 REFERENCES

[1] G. E. Moore, *Electronics*, **38**, 114 (1965).

[2] M. T. Bohr, *IEEE IEDM Tech. Dig.*, 241 (1995).

[3] L. Peters, *Semiconductor International*, **21**, 64 (1998).

[4] N. Magen, A. Kolodny, U. Weiser, and N. Shamir, *Proceedings of the 2004 international workshop on System level interconnect prediction*, 7 (2004).

[5] P. Xu, K. Huang, A. Patel, S. Rathi, B. Tang, J. Ferguson, J. Huang, C. Ngai, and M. Laboda, *Proceedings of the IEEE 1999 International Interconnect Technology Conference*, 109 (1999).

[6] Y. H. Wang, M. R. Moitreyee, R. Kumar, L. Shen, K. Y. Zeng, J. W. Chai, and J. S.

Pan, *Thin Solid Films*, **460**, 211 (2004).

[7] C.-K. Hu, L. M. Gignac, E. Liniger, C. Detavernier, S. G. Malhotra, and A. Simon, *J. Appl. Phys.*, **98**, 124501 (2005).

[8] C.-K. Hu, L. Gignac, R. Rosenberg, E. Liniger, J. Rubino, C. Sambucetti, A. Domenicucci, X. Chen, and A. K. Stamper, *Appl. Phys. Lett.*, **81**, 1782 (2002).

[9] A. E. Kaloyeros and E. Eisenbraun, *Annu. Rev. Mater. Sci.*, **30**, 363 (2000).

[10] M. Traving, G. Schindler, G. Steinlesberger, W. Steinhoegl, M. Engelhardt, *Semiconductor International* **26**, 73 (2003).

[11] Z. L. Yuan, D.H. Zhang, C.Y. Li, K. Prasad, C.M. Tan, and L.J. Tang, *Thin Solid Films*, **434**, 126, 2003.

[12] K. Holloway, P. M. Fryer, C. Cabral, J. M. Harper, P. J. Bailey, K. H. Kelleher, *J. Appl. Phys.*, **71**, 5433 (1992).

[13] G. Bai, S. Wittenbrock, V. Ochoa, M. Bohr, *Mater. Res. Soc. Symp. Proc.*, **403**, 501 (1996).

[14] T. Oku, E. Kawakami, M. Uekubo, K. Takahiro, S. Yamaguchi, and M. Murakami, *Appl. Surf. Sci.*, **99**, 265 (1996).

[15] H. Simka, S. Shankar, C. Duran, and M. Harverty, *Mater. Res. Soc. Symp. Proc.*, **863**, 283 (2005).

[16] International Technology Roadmap for Semiconductors, 2006 Update, http://public.itrs.net (2006).

[17] S. M. Rossnagel and H. Kim, *Proceedings of the IEEE 2001 International Interconnect Technology Conference*, 3 (2001)

[18] X. Chen, H. L. Frisch, A. E. Kaloyeros, and B. Arkles, *J. Vac. Sci. Technol. B*, **16**, 2887 (1998)

[19] H. Kim, C. Cabral, Jr., C. Lavoie, and S. M. Rossnagel, *J. Vac. Sci. Technol. B*, **20**, 1321 (2002).

[20] X. Chen, H. Frisch, B. Arkles, J. Sullivan, and A. Kaloyeros, *J. Va. Sci. Technol. B*, **17**, 182 (1999).

[21] H. Kim, A. J. Kellock, and S. M. Rossnagel, *J. Appl. Phys*. **92**, 7080 (2002).

[22] H. Kim, C. Detavenier, O. van der Straten, S. M. Rossnagel, A. J. Kellock, and D. G. Park, *J. Appl. Phys.*, **98**, 017308 (2005).

[23] M. W. Lane, C. E. Murray, F. R. McFeely, P. M. Vereecken, and R. Rosenberg, *Appl. Phys. Lett.*, **83**, 2330 (2003).

[24] H. Kim, Y. Naito, T. Koseki, T. Ohba, T. Ohta, Y. Kojima, H. Sato, and Y. Shimogaki, *Jpn. J. Appl. Phys.*, **45**, 2497 (2006).

[25] R. Chan, T. N. Arunagiri, Y. Zhang, O. Chyan, R. M. Wallace, M. J. Kim, T. Q. Hurd,

Electrochem. Solid-State Lett., **7**, G154 (2004)

[26] J. Tan, X. Qu, Q. Xie, Y. Zhou, and G. Ru, *Thin Solid Films*, **504**, 231 (2006). The properties of Ru on Ta-based barriers

[27] S. Rossnagel, *Solid State Technology*, Online Article (www.solid-state.com), February (2005).

[28] Q. Wang, J. G. Ekerdt, D. Gay, Y. Sun, J. M. White, *Appl. Phys. Let*t., **84**, 1380 (2004).

[29] M. Green, M. Gross, L. Papa, K. Schnoes, D. Brasen*, J. Electrochem. Soc.* **132**, 2677 (1985).

[30] Y. Matsui, M. Hiratani, T. Nabatame, Y. Shimamoto, S. Kimura, *Electrochem. Solid-State Lett*. **5**, C18 (2002).

[31] M. Lashdaf, T. Hatanpää, A. O. I. Krause, J. Lahtinen, M. Lindblad, M. Tiitta, Appl. Catal. A, **51**, 241 (2003).

[32] H. L. Skriver, N. M. Rosengaard, *Phys. Rev. B*, **46**, 7157 (1992).

[33] A. E. Kaloyeros and E. Eisenbraun, Annu. *Rev. Mater. Sci*., **30**, 363 (2000).

[34] A. Kohn, M. Eizenberg, Y. Shacham-Diamand, *Appl. Surf. Sci*., **212**, 367 (2003).

[35] W. Klement, R. H. Willens, P. Duwez, *Nature*, **187**, 869 (1960).

[36] A. Inoue, N. Nishiyama, H. Kimura, *Mater. Trans. JIM,* **38**, 179 (1997).

[37] J. Schroers and W. L. Johnson, *Appl. Phys. Lett.*, **84**, 3666 (2004).

[38] T. Egami and Y. Waseda, *J. Non-Cryst. Solids*, **64**, 113 (1984).

[39] D. Wang, U. Geyer, and S. Schneider, *J. Non-Cryst. Solids*, **221**, 222 (1997).

[40] F. Q. Guo, S. J. Poon, and G. J. Shiflet, *J. Appl. Phys.*, **97**, 013512 (2004).

[41] H. Ma, L. L. Shi, J. Xu, Y. Li, E. Ma, *Appl. Phys. Lett.*, **87**, 181915 (2005).

[42] A. Peker and W. L. Johnson, *Appl. Phys Lett.*, **63**, 2342 (1993).

[43] Ch. Hausleitner and J. Hafner, *Phys. Rev. B*, **47**, 5689 (1993).

[44] E.J. O'Sullivan, A.G. Schrott, M. Paunovic, C.J. Sambucetti, J.R. Marino, P.J. Baily, S. Kaja, K.W. Semkow, *IBM J. Res. Dev.*, **42**, 607 (1998).

[45] A. Kohn, M. Eizenberg, Y. Shacham-Diamand, B. Israel, and Y. Sverdlov, *Microelectron. Eng.* **55**, 297 (2001).

Chapter 2

Screening of Ruthenium CVD/ALD Precursors

2.1 INTRODUCTION

Ruthenium metal has been considered for a number of microelectronics applications, including use as a directly plateable copper diffusion barrier in future ultra-large scale integrated circuit (ULSI) processing [1]. Due to the continuing trend of miniaturization in microelectronic devices, the current Cu interconnect scheme comprising a Ta/TaN diffusion barrier and PVD Cu seed layer is expected to encounter scaling difficulties at the 32nm node [2,3]. Future interconnect applications will require ultrathin (< 5nm) continuous films, which may be deposited directly onto a dielectric or onto a refractory material, such as Ta or TaN that functions as the Cu diffusion barrier. Additionally, these films must have low resistivity, high resistance to copper diffusion, and good adhesion to Cu. Several new materials are currently under investigation to meet these requirements, and a composite layer including thin Ru film is one of the promising candidates [4-6]. The advantages are that it has low resistivity, ~7 $\mu\Omega\cdot$cm, and its oxide, RuO_2, is electrically conductive and so Ru can therefore function as a seed layer in addition to a Cu diffusion barrier. The low solubility of Ru in copper can help to keep copper resistance low. It's adhesion to directly electroplated copper films could be potentially beneficial for electromigration performance [7].

Presently, methods for the atomic layer deposition (ALD) or chemical vapor deposition (CVD) of Ru are limited to the use of Ru carbonyl ($Ru_3(CO)_{12}$) [8], cyclopentadienyl derivatives such as Cp_2Ru [9] or $(EtCp)_2Ru$ with O_2 [10] and β-diketonates such as $Ru(thd)_3$ [11] or $Ru(hfac)_2$ with H_2 [12]. (Cp = η^5-C_5H_5, EtCp = η^5-C_5H_4Et, thd = 2,2,6,6-tetramethyl-3,5- heptanedione, hfac = hexafluoroacetylacetonate). A Ru film with a plasma enhanced atomic layer deposition (PE-ALD) with $(EtCp)_2Ru$ and NH_3 was also reported [13]. However, available precursors for Ru film growth with CVD and especially with ALD are quite limited, and growth mechanisms and properties of ultrathin Ru films are not yet well understood.

This chapter describes the research on precursor screening and characterization of the films grown with CVD and ALD methods. It explores the growth mechanisms of ultra thin Ru films on several substrates, and characterization of the films including compositional, structural and electrical properties.

2.2 EXPERIMENTAL DETAILS

The film growth and subsequent surface analysis measurements were carried out in a film deposition and characterization facility, consisting of a load lock chamber, sample transfer system, surface analysis chamber, electrical test chamber, physical vapor deposition (PVD) chamber and chemical vapor deposition (CVD) chamber. A schematic diagram of the UHV system is shown in Illustration 2.1. The film deposition and analysis chambers are connected with the sample transfer chamber having a based pressure of 1×10^{-8} Torr, and samples can get film growth and analysis with exposure to air. PVD chamber is equipped with three independent DC magnetron sputtering guns having with Cu, Ta, and Ru targets. Composite films can be grown by using multiple guns simultaneously, and the PVD system also has radio frequency (RF) sputtering deposition capability. The base pressure of the PVD chamber is 5×10^{-8} Torr. The surface analysis chamber has a base pressure of 1×10^{-9} Torr, and equipped with Physical Instrument (PHI) 3057 XPS system with LEISS capability.

Four Ru precursors were employed in the study: dodecacarbonylruthenium trimer (Ru-carbonyl), $Ru_3(CO)_{12}$, (η^6-benzene)(η^4-1,3-cyclohexadiene)ruthenium, $Ru(C_6H_6)$-(C_6H_8), (2,4-dimethylpentadienyl)(ethylcyclopentadienyl)ruthenium (DER), $Ru(C_7H_{11})$-(C_7H_9), and bis(2,4-Dimethylpentadienyl)ruthenium (DMPD), $Ru(C_7H_{11})_2$ precursors. Ru films were deposited in the CVD chamber, which has a base pressure of 5×10^{-8} Torr, using the Ru-carbonyl and (benzene)(cyclohexadiene)ruthenium precursors. The Ru-carbonyl precursor was loaded into a metal-glass bubbler, and was heated to 355 K. (Benzene)(cyclohexadiene)ruthenium was also loaded in a bubbler and heated to 335 – 355 K. The precursors were delivered to into the CVD chamber through a gas line and

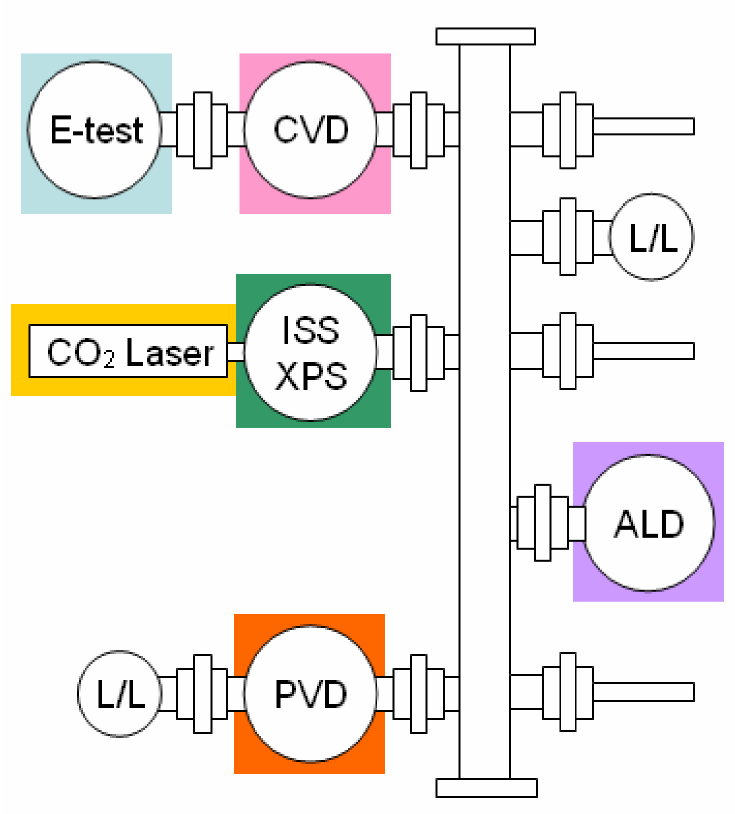

Illustration 2.1 Schematic diagram of the UHV thin film deposition and characterization system.

shower head that were heated 10 degrees higher than the bubbler temperature to avoid precursor condensation. Argon carrier gas at a flow rate of 10 standard cubic centimeters per minute (sccm) was used to sweep the precursor from the bubbler and into the chamber. The substrate was heated between 425 and 525 K, and the chamber pressure was maintained at 50 mTorr during film deposition.

ALD and CVD Ru film deposition tests with the DER precursor were performed using the ALD chamber with the base pressure of 8×10^{-8} Torr. The DER precursor was heated to 335 – 355 K. The gas line and shower head were heated 10 degrees higher than the bubbler temperature, and the chamber was held at 335 to 370 K. The ALD process consisted of repeating cycles, with each cycle involving precursor dosing, purging, reactant dosing, and purging steps. Oxygen was used as the reactant gas. The duration time of each step was varied for different experiments.

Film composition was analyzed *in situ* using a PHI 3057 X-ray photoelectron spectrometer. For X-ray photoelectron spectroscopy (XPS) analysis, Mg Kα X-rays were employed, and pass energies of 117.4 eV and 58.7 eV were employed for survey and for high-resolution scans, respectively. For low energy ion scattering spectroscopy (LEISS) a 1 kV He^+ ion beam was employed; both the incident ion beam and the detector were 30 degrees from the sample normal. In order to obtain a depth profile or to remove surface contamination, some films were sputtered with 5 kV Ar^+ ions at a sample current of 1 μA. *Ex situ* analysis involved transmission electron microscopy (TEM), scanning electron microscopy (SEM) and energy dispersive X-ray spectroscopy (EDS). The film surface morphology was measured using a LEO 1530 scanning electron microscope. TEM was performed with a JOEL 2010F microscope at 200 kV accelerating voltage. The TEM samples were prepared by cutting the samples with a low speed saw, mechanical polishing, and ion milling with a focused ion beam (FIB) system. The final sample thickness was less than 20 nm.

2.3 RESULTS AND DISCUSSION

2.3.1 CVD Ru Film Growth with $Ru_3(CO)_{12}$

Ru-carbonyl, $Ru_3(CO)_{12}$, is an orange colored solid precursor which is stable in air at room temperature. We have previously reported that $Ru_3(CO)_{12}$ precursor decomposes to form pure metallic Ru on SiO_2 and Ta substrates without adding any reactant at temperatures as low as 425 K [14]. Figure 2.1 shows XPS and LEISS scan results of the Ru films grown on SiO_2 substrate with the $Ru_3(CO)_{12}$ precursor as a function of deposition time. The substrate temperature was held at 475 K during the film growth. As deposition time increased, the silicon peak from the SiO_2 substrate decreased, and completely disappeared after 30 min of deposition. The binding energies are consistent with metallic Ru.

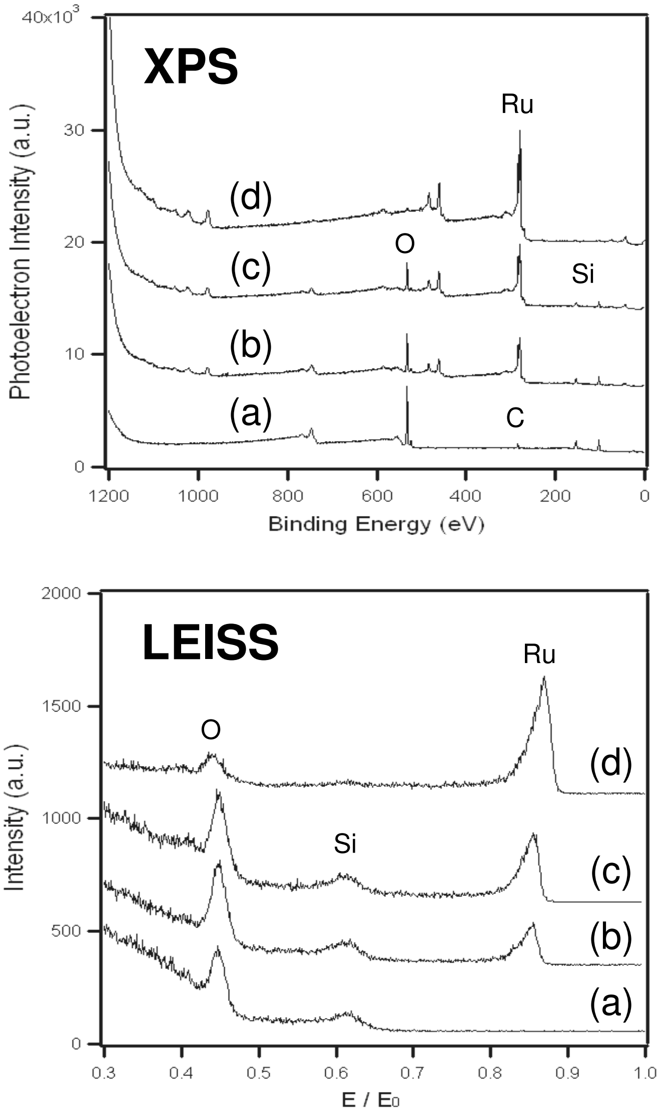

Figure 2.1 XPS (top) and LEISS (bottom) scan results of the Ru films grown on SiO_2 with $Ru_3(CO)_{12}$ as a function of deposition time. (a) no deposition, (b) 10 min, (c) 20 min, (d) 30min.

TEM images of the Ru film grown with $Ru_3(CO)_{12}$ precursor on a Metal 1 trench patterned SiO_2 wafer are shown in Figure 2.2 (a). The sample was deposited at 475 K for 1 hr. The trench width and aspect ratio are 0.20μm and ~5.0, respectively. As part of the TEM sample preparation, BC_xN_y/Pt layers were deposited on the sample after Ru film growth. The Ru film was continuous and the thickness was 31nm at the top of the trenches, however only discontinuous grains were observed at the sidewall and bottom of the trenches. The results indicate that a thermally activated self decomposing CVD process without a reactant gas, such as oxygen or hydrogen, tends to have poor step coverage due to its high sticking coefficient and insufficient precursor migration into deep features. Continuous film formation is also hampered by the three-dimensional growth characteristics of $Ru_3(CO)_{12}$.

Lower substrate temperatures were explored to reduce the precursor reaction rate and improve step coverage [14]. Figure 2.2 (b) shows TEM images of the sample deposited for 1 hr at 425 K, which is the lowest temperature that a Ru film can be grown with $Ru_3(CO)_{12}$. The trench width and aspect ratio were 0.22μm and ~ 4.5, respectively. The 22 nm thickness of this Ru film was slightly lower than the sample grown at 475 K. Lowering the deposition temperature did lower the growth rate (precursor reactivity) and slightly improved step coverage. However the improvement was not significant. Figure 2.2 (c) shows TEM images of the Ru sample grown with the addition of NH_3. Ammonia was used to see if a molecule that would compete for adsorption sites on Ru

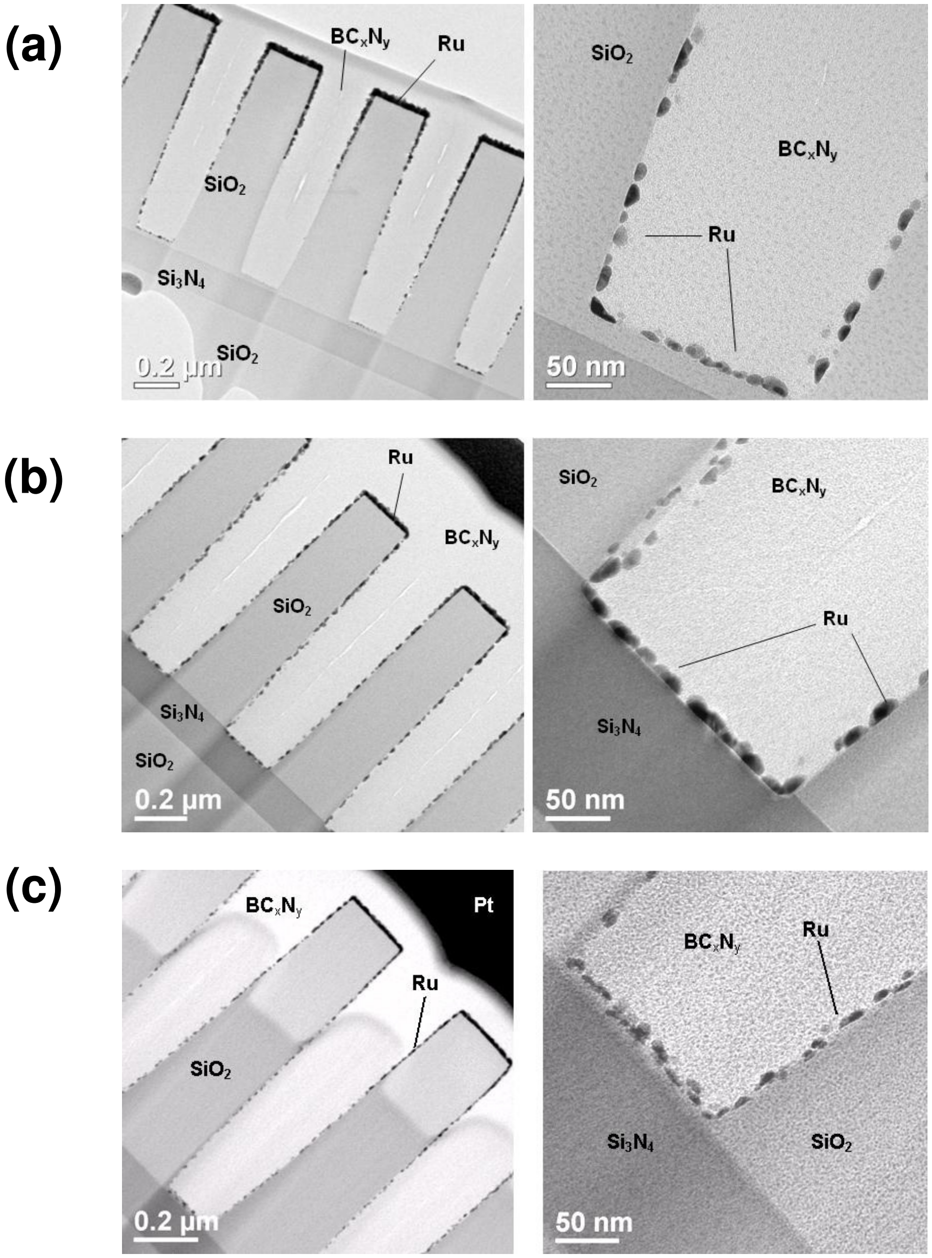

Figure 2.2 TEM images of a CVD Ru grown on a M1 trench patterned SiO_2 substrate with $Ru_3(CO)_{12}$ for 1 hr (a) at 475 K, (b) 425 K, and (c) with NH_3 at 475 K.

with the $Ru_3(CO)_{12}$ and not incorporate into the film, could slow the rate of Ru film growth and improve the coverage. CO was also considered for these studies but experimental complications of delivering CO using stainless steel tubing prevented its use. As shown in Figure 2.2 (c), NH_3 addition did not result in significantly improved step coverage. The film was grown at 475 K for 1 hr, and the trench width was ~ 0.18µm. Ammonia diluted the precursor, *i.e.*, lowered its partial pressure, and slowed the effective growth rate. The film was ~15nm at top and ~10nm at bottom of the trenches. This contrasts with 22 nm on the top at 475 K for 1 hr without NH_3. The images at the bottom illustrate an incomplete Ru layer formed and while NH_3 may have improved step coverage somewhat, the final result is unacceptable – an incomplete film. Throughout the series of experiments exploring step coverage in CVD using the $Ru_3(CO)_{12}$ precursor, it never was possible to realize a continuous film at the bottom of a trench when the film was 15 to 30 nm thick at the top of the trench. This result combined with the lack of any changes in growth rate with the addition of H_2 led us to abandon studies with the $Ru_3(CO)_{12}$ precursor.

2.3.2 CVD Ru Film Growth with $Ru(C_6H_6)(C_6H_8)$

$RuCl_3{\cdot}3H_2O$ 0.32 g (1.23 mmol) was completely dissolved in ethanol (10 mL) in a Schlenk flask under nitrogen. 1,3-Cyclohexadiene (5mL, 52 mmol) and zinc dust (3g, 45 mmol) were added to the above solution and the mixture was stirred for 3 hr at room temperature. The resulting yellow-brown solution was filtered, and the solid residue was washed with hexane (30mL). The solvent of the combined solution was evaporated under reduced pressure and the solid residue obtained was extracted with pentane (2 × 40 mL). The light yellow pentane solution was filtered through a short bed of Celite. Reduction of the volume of the solvent under vacuum to about 4 mL and cooling to 215 K gave light yellow crystals of (η^6-Benzene)(η^4-1,3-Cyclohexadiene)Ruthenium(0). Yield: 75 %. MP: 118-120 ºC. ^{1}H NMR: (acetone-d_6) 5.4 (s, 6H), 4.75(dd, 2H), 3.02(m, 2H), and 1.39(m, 4H) ppm.

$$2RuCl_3 \cdot 3H_2O + 6C_6H_8 + 3Zn \rightarrow 2[Ru(C_6H_6)(C_6H_8)] + 3ZnCl_2 + 2C_6H_{10}$$

Figure 2.3 shows the XPS scan results of the Ru films grown on SiO_2 at 425 – 525 K for 1 hr by thermal decomposition. The minimum temperature for film growth was ~ 450 K and Ru peak intensity increased with higher substrate temperature. Silicon and oxygen peaks from the SiO_2 substrate decreased as substrate temperature increased due to increased surface coverage and thickness of the Ru film, and completely disappeared when the substrate temperature was 525 K. The binding energies of silicon, oxygen and Ru peaks indicate that silicon and oxygen peaks were from the SiO_2 substrate and the Ru was metallic (Ru^0).

The effect of adding H_2 gas along with the precursor during CVD was explored to

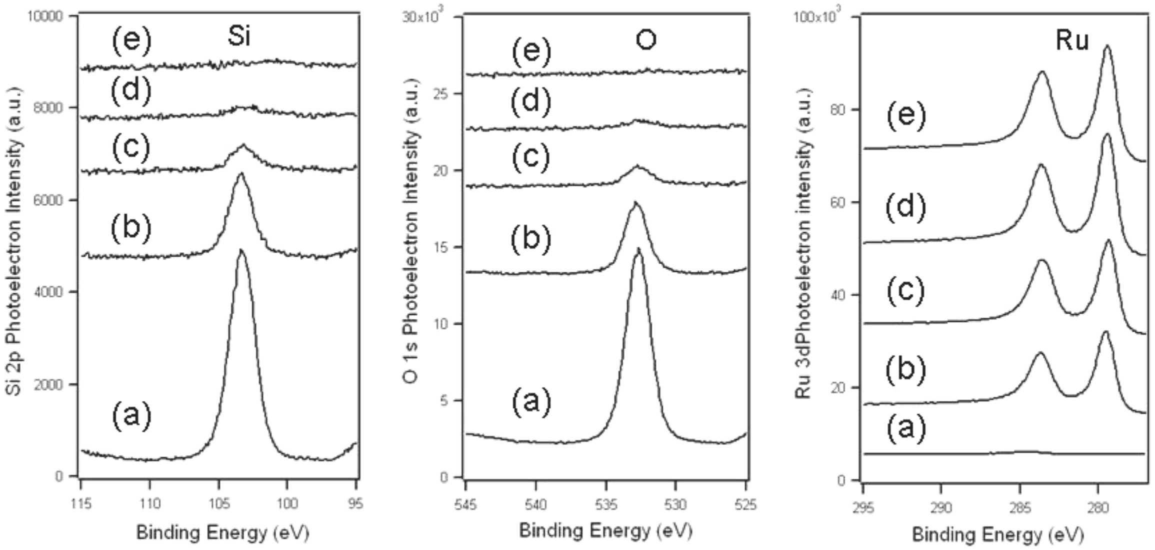

Figure 2.3 XPS Si 2p, O 1s, and Ru 3d peaks of Ru films grown on SiO_2 substrate by thermal decomposition with the $Ru(C_6H_6)(C_6H_8)$ precursor at 425 – 525 K for 1 hr. (a) 425 K, (b) 450 K, (c) 475 K, (d) 500 K, and (e) 525 K.

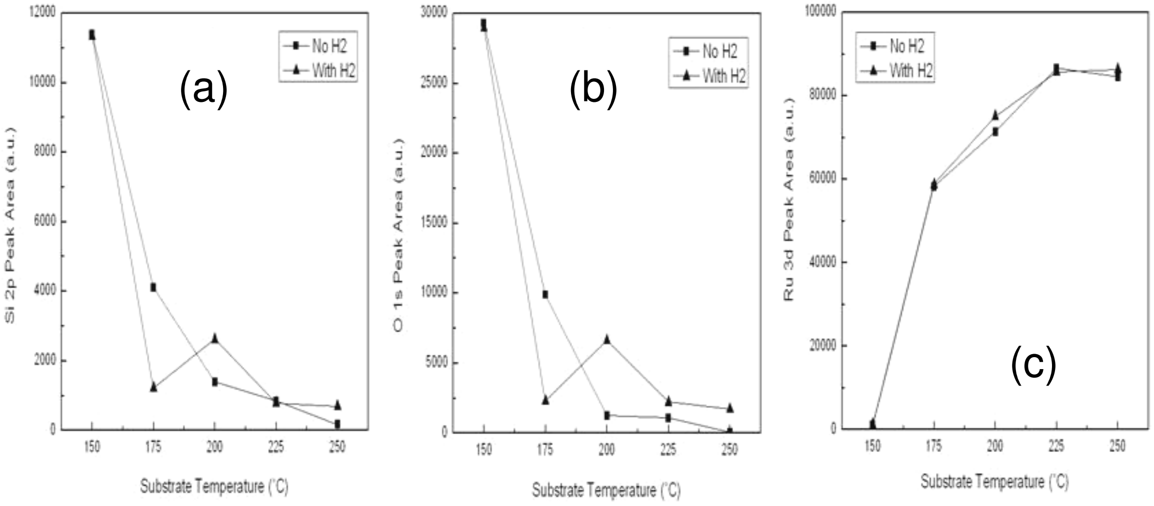

Figure 2.4 XPS intensities of Si 2p, O 1s, and Ru 3d peaks of the Ru films grown from $Ru(C_6H_6)(C_6H_8)$ on SiO_2 at 425 – 525 K for 1 hr with and without H_2. (a) Si 2p peak, (b) O 1s peak, and (c) Ru 3d peak.

determine if the $Ru(C_6H_6)(C_6H_8)$ precursor is applicable for an ALD process with reducing chemistry. The H_2 flow rate was ~10sccm, and the chamber pressure during film growth was maintained at 50 mTorr. The comparison of XPS peak intensities with and without H_2 is shown in Figure 2.4. Any effect of added H_2 on the growth rates is minor, suggesting that H_2 did not react with $Ru(C_6H_6)(C_6H_8)$ and increase the growth rate over the temperature range examined. Since $Ru(C_6H_6)(C_6H_8)$ decomposes at temperatures above 450 K to form Ru film by itself, this precursor will not be applicable for an ALD process with reducing chemistry.

Ideally, the film surface coverage and fraction of free substrate can be obtained with LEISS scan results [15,16]. The disappearance of LEISS peaks the from substrate can be used to estimate that stage in the growth where the growing film becomes completely continuous. However, it should be noted that in cases with three-dimensional films and with an ion gun and detector that are not aligned with the sample surface normal, a shadowing effect caused by the film roughness leads to an underestimation of the free surface (in this case the SiO_2 surface) [17]. Although LEISS has a limitation in addressing surface coverage, combining XPS and LEISS offers useful information about film properties. Figure 2.5 shows surface coverage (established with the ion scattering results) versus the XPS peak intensity ratio I_{Ru} / I_{Si} of the CVD films from $Ru_3(CO)_{12}$, the CVD films from $Ru(C_6H_6)(C_6H_8)$,and PVD Ru films. XPS samples more than the topmost layer and as a film becomes physically thicker, it will

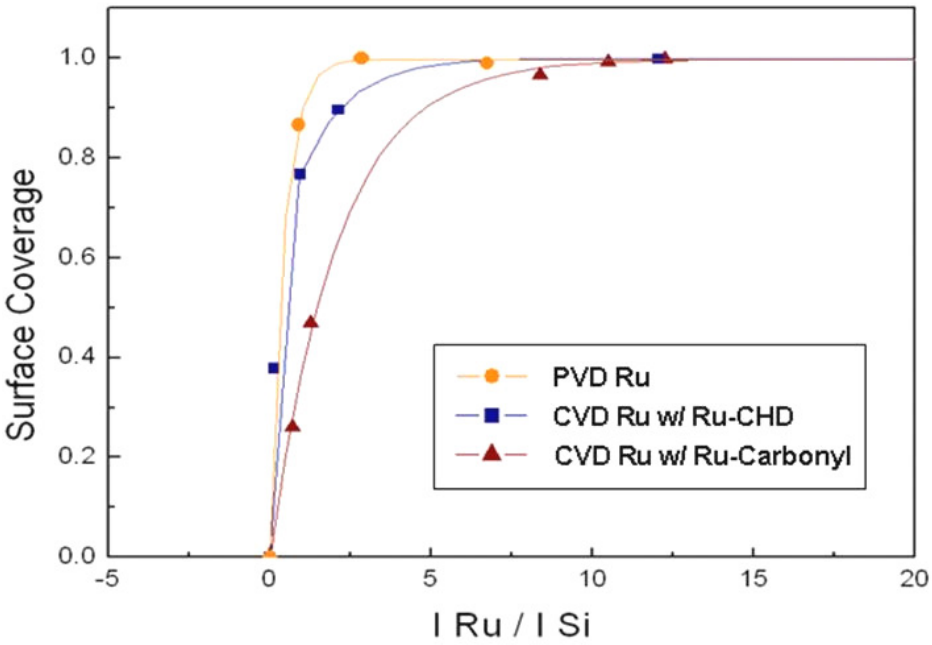

Figure 2.5 Surface coverage based on LEISS intensity ratios for CVD films from $Ru_3(CO)_{12}$ and $Ru(C_6H_6)(C_6H_8)$ grown at 425 K and PVD Ru films as a function of the XPS peak intensity ratio I_{Ru} / I_{Si}.

ultimately cover the substrate to a thickness that precludes the substrate peaks from being detected in XPS. For a 2D film, the surface coverage will approach unity for small I_{Ru} / I_{Si} ratios since the film is uniformly covering the substrate; whereas for a 3D film, larger I_{Ru} / I_{Si} ratios are required to attain complete surface coverage because the substrate continues to be sampled by XPS. The CVD films needed more film growth to achieve complete surface coverage than PVD films due to their strong 3D growth mechanism. The films from $Ru(C_6H_6)(C_6H_8)$ required a lower I_{Ru} / I_{Si} to reach full surface coverage than the films from Ru-carbonyl. This suggests the Ru-carbonyl films should be rougher, *i.e.,* more 3D growth, and likely featured a lower nucleation density than the $Ru(C_6H_6)(C_6H_8)$-based films. This is consistent with AFM and SEM measurement results shown in Figure 2.6 and 2.7 (a) and (b). Root mean square (RMS) surface roughness values of the CVD film with Ru- carbonyl, the CVD film with $Ru(C_6H_6)(C_6H_8)$, and the PVD film were 1.44nm, 0.58nm, and 0.11nm, respectively. The film with $Ru(C_6H_6)(C_6H_8)$ showed a smoother surface and lower roughness value than the film with Ru-carbonyl.

Figure 2.7 (c) shows TEM images of the CVD Ru film deposited with the $Ru(C_6H_6)(C_6H_8)$ precursor in a M1 trench patterned in thermal oxide. The substrate temperature was 505 K, and deposition time was 1 hr. The trench width and aspect ratio were ~0.34μm and ~3.0, respectively. TEOS/Pt layers were formed onto the sample to protect the thin Ru film during TEM sample preparation. Measured film thicknesses

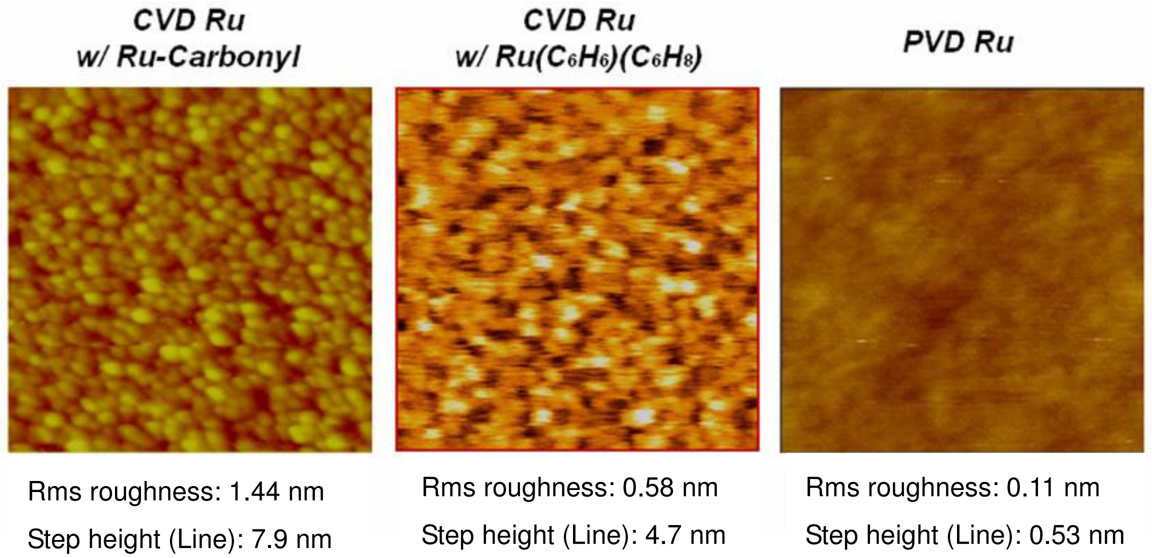

Figure 2.6 AFM scan images and measured RMS roughness values of the CVD Ru films deposited with $Ru_3(CO)_{12}$ and $Ru(C_6H_6)(C_6H_8)$ and a PVD Ru film.

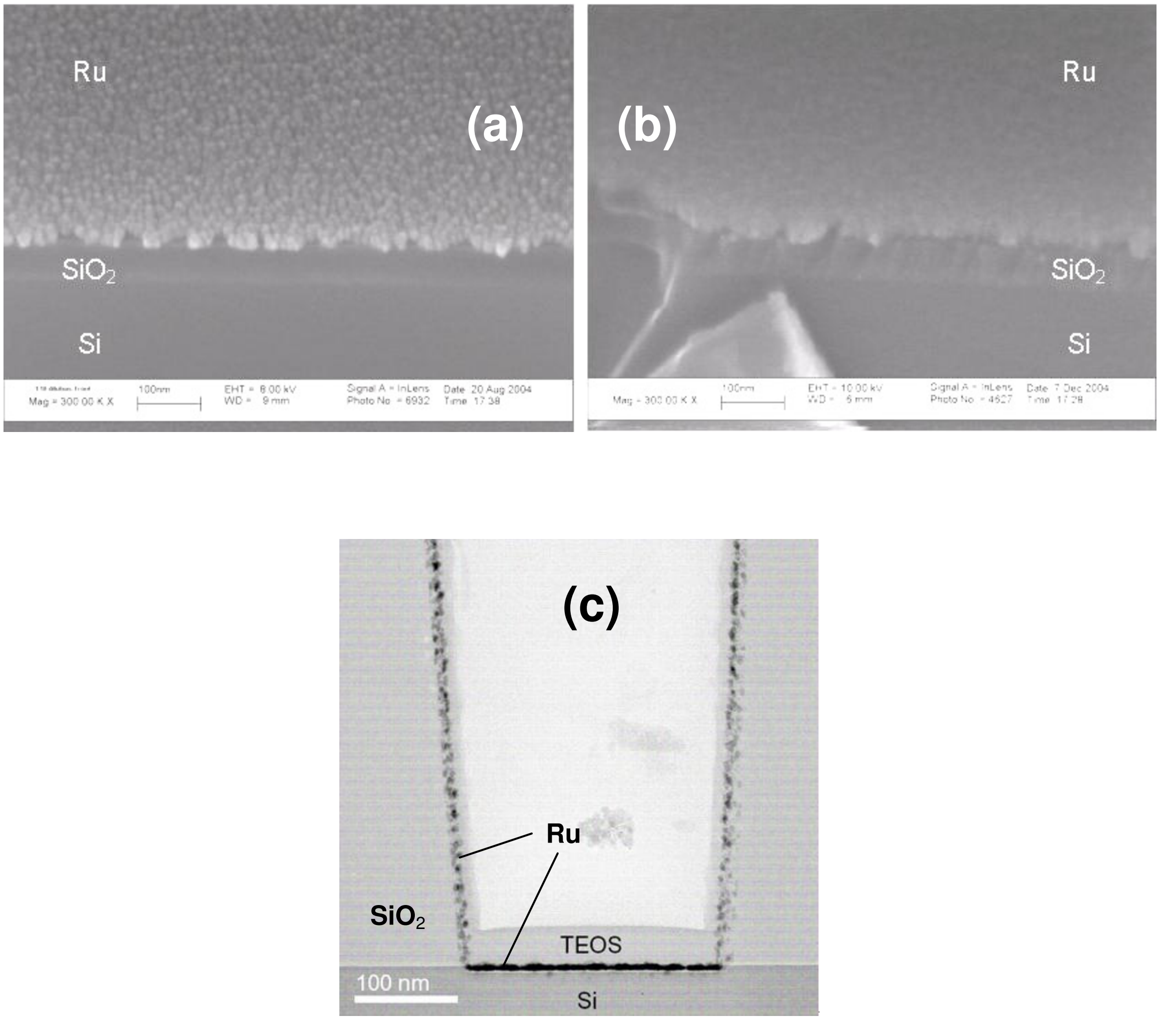

Figure 2.7 (a) SEM images of the CVD Ru films deposited with $Ru_3(CO)_{12}$ and $Ru(C_6H_6)(C_6H_8)$. (b) TEM image of a CVD Ru film grown on trench pattern using $Ru(C_6H_6)(C_6H_8)$ at 505 K for 1 hr.

were 16.6nm, 8.3nm, and 5.8nm at the top, sidewall, and bottom of the trench, respectively. The film at the sidewall was not completely continuous due to insufficient step coverage and insufficient film growth. The thermally activated self decomposing CVD process without reaction gas tends to have poor step coverage due to a high sticking coefficient and a minimal migration of precursor molecules into deep features. Furthermore, the 3D growth inhibits the formation of a continuous thin film. Nonetheless, the Ru films deposited with $Ru(C_6H_6)(C_6H_8)$ showed better step coverage and a more continuity than the films deposited with Ru-carbonyl as shown in Figure 2.2.

2.3.3 CVD/ALD Ru Film Growth with $Ru(C_7H_{11})(C_7H_9)$ - DER

CVD and ALD deposition tests were performed with the $Ru(C_7H_{11})(C_7H_9)$ Ru precursor from TOSOH Corporation. The precursor is referred to as DER based on the chemical name, and is a pale yellow liquid that is stable in air with a melting point of 490 K. It has viscosity of ~6cP at room temperature, and the vapor pressure of $\sim 1.3\times10^{-2}$ Pa at 350 K. According to the reports from TOSOH [18,19], the precursor starts to decompose thermally at 545 K, Ru films can be deposited at 535 – 775 K by CVD without an additional reaction gas, and O_2 addition during CVD leads to smoother films with an apparent higher nucleation density. However, our deposition tests resulted in no Ru film growth without O_2. Figure 2.8 shows the XPS scan results after 1 hr of growth

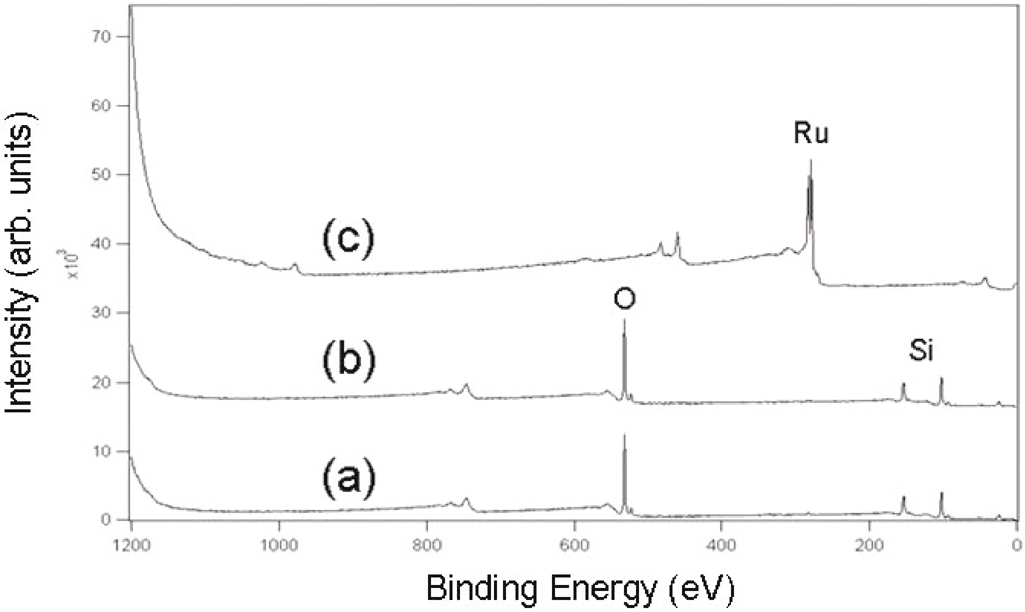

Figure 2.8 XPS scan results of CVD Ru films grown on SiO_2 with the DER precursor. (a) DER only, (b) DER + H_2, and (c) DER + O_2.

at 575 K with DER only, DER + O_2, and DER + H_2. The samples grown with DER only and DER + H_2 did not show a Ru peak, which indicates that there was no Ru film growth. On the other hand, the sample grown with DER + O_2 showed a significant Ru peak on XPS, and SEM inspection revealed a high growth rate, ~ 300Å/min. The inconsistency with the results previously reported by TOSOH is possibly due to the high base pressure of the TOSOH chamber; the chamber may have been contaminated with moisture or O_2. It was concluded that DER needs oxygen to form a Ru film and is therefore not a viable precursor for ALD by reduction at temperatures below 675 K.

Figure 2.9 (a) and (b) shows XPS and LEISS scan results of a Ru sample deposited with DER + O_2 and an ALD process for 50 deposition cycles. The substrate temperature was 575 K, and one deposition cycle consisted of precursor dosing, purging, O_2 dosing, and purging steps for 15 seconds each. The precursor was contained in a saturator at 355 K, and the chamber pressure was ~500 mTorr. XPS and LEISS showed significant Ru peaks and no substrate peaks, thereby indicating complete surface coverage. The deposited film was polycrystalline with a columnar structure and the thickness of the film was ~ 60 nm, as indicated in Figure 2.9 (c). The calculated growth rate was ~1.2 nm/cycle which is too high for an ALD process, given that others report ALD Ru growth rates of ~0.04 nm/cycle.

Figure 2.10 (a) shows XPS scan results of Ru films as a function of precursor

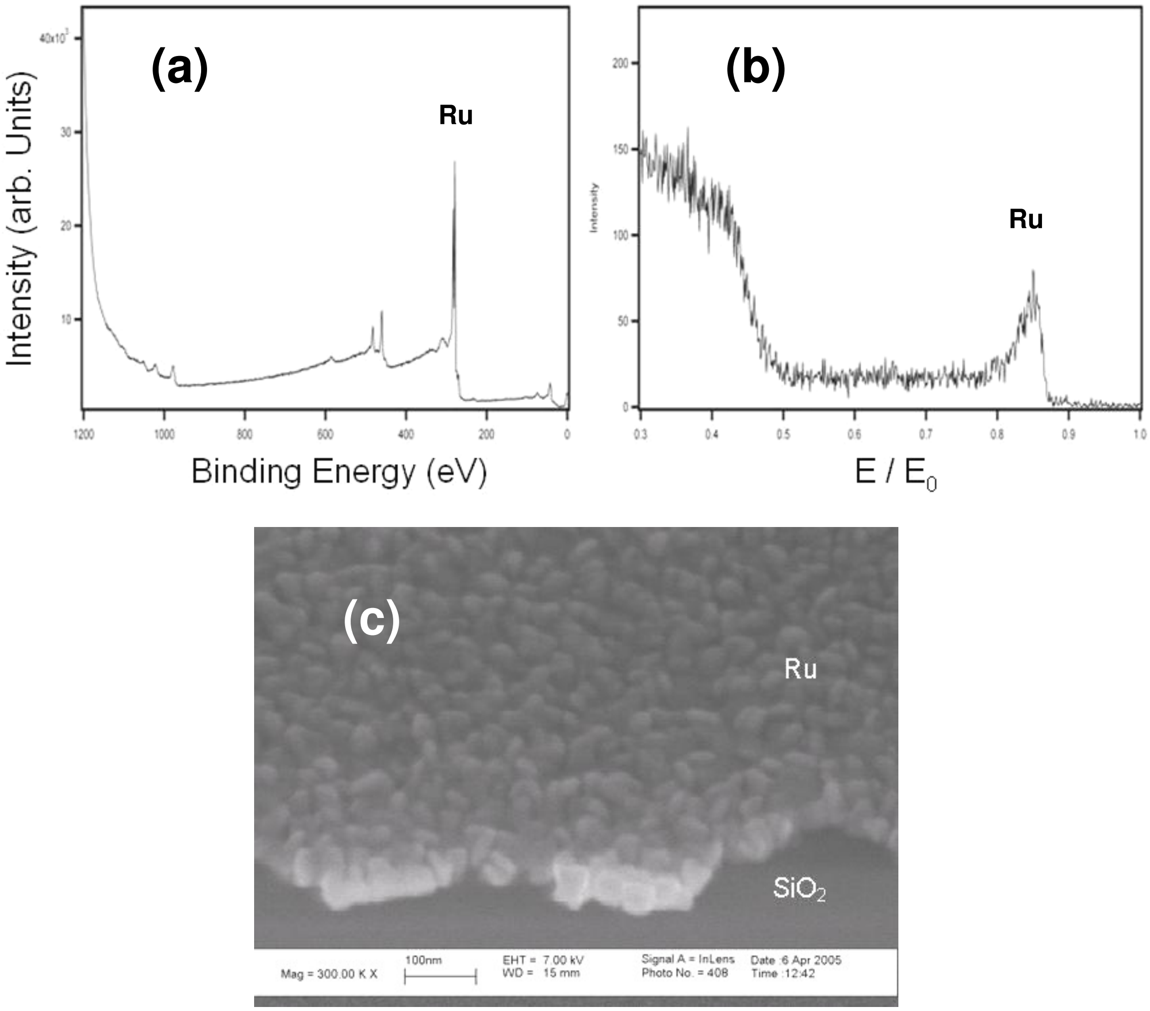

Figure 2.9 (a) XPS scan result, (b) LEISS scan result, and (c) SEM image of Ru film grown with DER + O_2 on a SiO_2 substrate at 575 K for 50 cycles.

dosing time. The samples were deposited at 575 K for 50 cycles and the precursor was dosed for 5, 10, and 15 sec. In this experiment, the purging times were increased to 30 sec. The growth rate of an ALD process should be independent of precursor dosing time because ALD film growth is associated with self-saturating adsorption of precursor molecules. However, XPS showed an increase in the growth rate as the precursor dosing time was increased. The increased growth rate per cycle seems to be due to increased precursor molecules delivered into the reaction chamber by increasing precursor dosing time, which suggests that the film grows by the CVD, not ALD. Figure 2.10 (b) shows XPS and LEISS scan results of the Ru films as a function of purging time after precursor and oxygen dosing steps. The precursor and reactant oxygen dosing times were kept constant at 5 sec, and purging times were changed from 15 to 90 sec. ALD precursor molecules should adsorb onto the substrate, remain on the surface during purging precursor molecules from the reaction chamber or possibly partially desorb during the purging step, and then react with the O_2 reactant to form a film. Purge cycle studies can reveal if the chamber is free of one reactant before the second reactant is admitted. Higher growth rates were realized with decreasing purge times which could indicate significant gas phase hold up of the precursor within dead zones in the reactor or significant hold up of the precursor on the walls of ALD reactor.

An experiment was performed to study the effect of reaction chamber wall temperature and determine if the precursor holdup was associated with adsorption on the

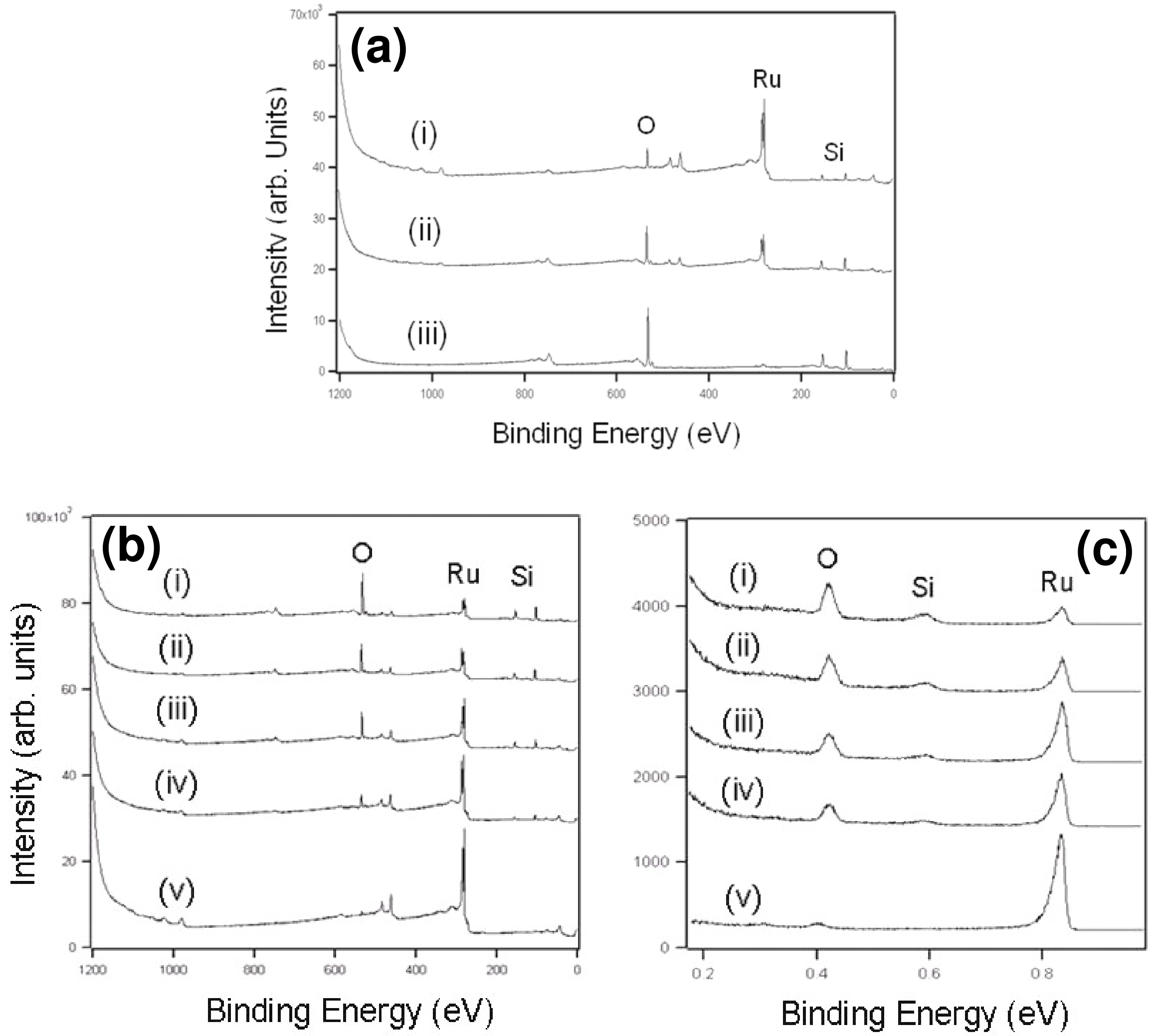

Figure 2.10 (a) XPS scan results of Ru films grown on SiO_2 with DER as a function of precursor dosing time, (i) 5 s, (ii) 10 s, and (iii) 15 s. (b) XPS and (c) LEISS results of Ru films grown with DER as a function of purging time, (i) 15 s, (ii) 30 s, (iii) 60 s, (iv) 75 s, and (v) 90 s.

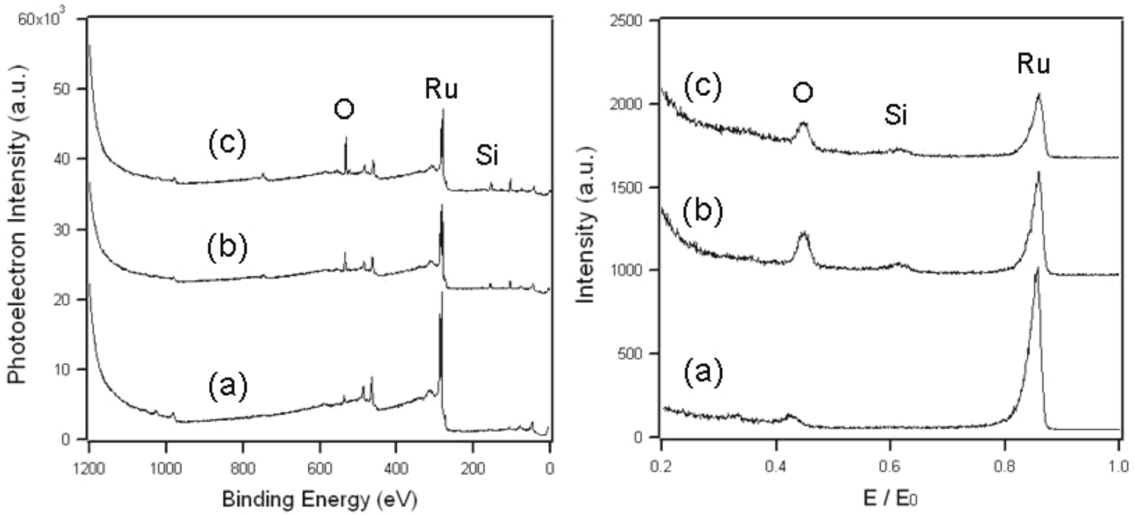

Figure 2.11 XPS (Left) and ISS (Right) scan results of the Ru films grown with DER as a function of chamber wall temperature. (a) 340 K, (b) 355 K, and (c) 370 K.

chamber surface. The substrate temperature was 575 K, and each cycle included 5, 30, 5, and 30 sec of precursor dosing, purging, O_2 dosing, and purging steps, respectively. XPS and LEISS scan results in Figure 2.11 show that as the wall temperature is decreased the film growth rate increases. From this we conclude the growth observed during the ALD cycles may involve an ALD process and definitely involves CVD between residual precursor that is evolving from the chamber wall and O_2 during the O_2 step in one ALD cycle. To suppress CVD film growth, a higher wall temperature than possible in our system is required.

2.3.4 CVD Ru Film Growth with $Ru(C_7H_{11})$ - DMPD

CVD deposition tests were performed with the bis(2,4-Dimethylpentadienyl)ruthenium, $Ru(C_7H_{11})_2$ precursor which is referred to as DMPD in this report. It is a yellow colored solid compound having a low sublimation temperature of 340 K. Deposition experiments in CVD mode were performed in the ALD chamber to test the viability of the precursor for an ALD process with reducing chemistry. XPS scan results of the films grown on SiO_2 substrates with the DMPD precursor for 1 hr at 425 – 575 K by thermal decomposition are shown in Figure 2.12 (a). From the binding energies of the Si, O and Ru peaks, it is apparent that the Si and O peaks are from the SiO_2 substrate and the Ru is in the zero-valent state (metallic Ru). The minimum

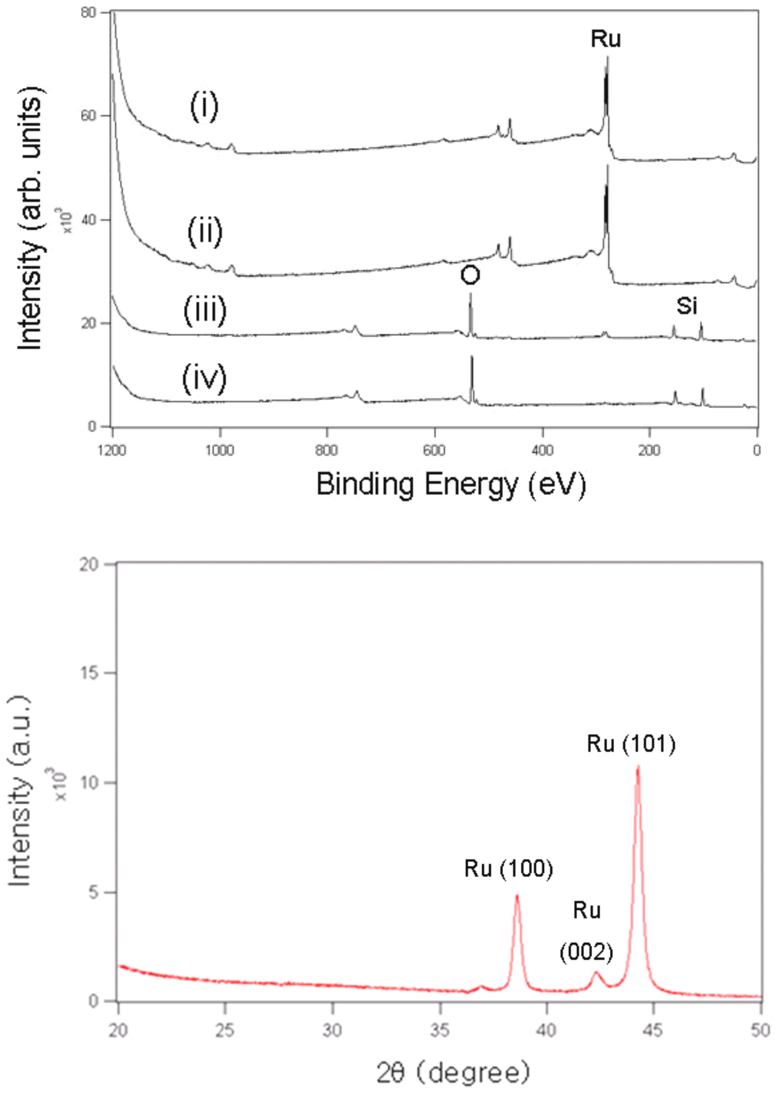

Figure 2.12 (a) XPS scan results of Ru films grown on SiO_2 with the DMPD precursor for 1 hour. (i) 525 K, (ii) 475 K, (iii) 425 K, and (iv) 375 K. (b) XRD result of Ru grown with DMPD on SiO_2 at 475 K for 20min.

temperature for film growth is ~525 K, and substrate peaks completely attenuate after 1 hr of deposition at 525 K. The resulting films are polycrystalline as shown in Figure 2.13. The film growth rate is high, ~9 nm/min at 425 K, and the average grain size of the film grown for 20 min is ~40 nm. The films are quite granular, and feature the columnar structure typical of a polycrystalline Ru film. Since the film is quite thick, ~120 nm, and composed of crystalline grains, grazing angle XRD showed clear peaks at $2\theta = 38°$, 42°, and 44° which represent the (100), (002), and (101) planes of the hexagonal Ru lattice as shown in Figure 2.12 (b).

The reactivity of the DMPD precursor with H_2 was examined in the ALD chamber at substrate temperatures 425 – 525 K. To minimize the precursor molecule partial pressure effect, He gas was introduced during some depositions in place of H_2. The XPS results of films grown with H_2 or He at different substrate temperatures are shown in Figure 2.14. H_2 does not enhance the film growth rate, and the growth rate is lower with H_2 than with He. Therefore, the DMPD precursor does not react with H_2 and is not viable for a CVD/ALD process in a reducing environment.

2.4 SUMMARY

Screening studies on CVD/ALD precursors for Ru film growth are reported. The precursors studied include dodecacarbonylruthenium (Ru-carbonyl), $Ru_3(CO)_{12}$, (η^6-

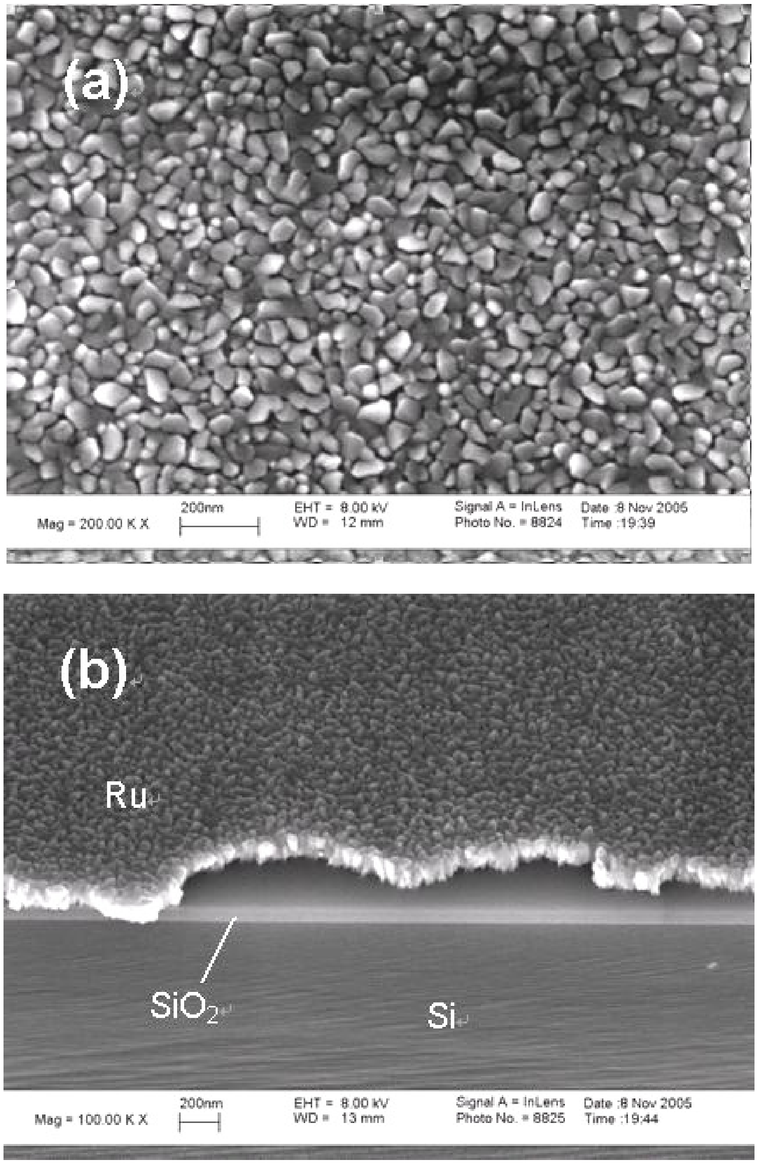

Figure 2.13 SEM image of ruthenium films grown with DMPD on SiO_2 at 525 K for 20min. (a) Top view, and (b) tilted view.

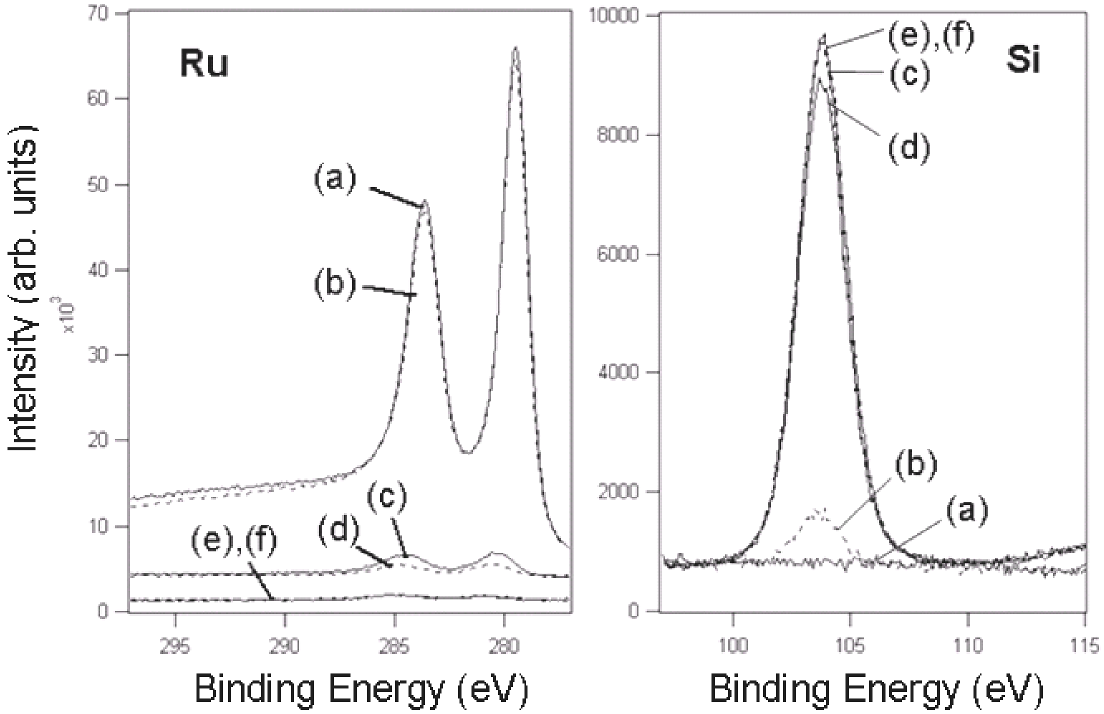

Figure 2.14 XPS scan result with H_2 or He at different substrate temperatures. (a) 525 K with He, (b) 525 K with H_2, (c) 475 K with He, (d) 475 K with H_2, (e) 425 K with He, (f) 425 K with H_2.

benzene)(η^4-1,3-cyclohexadiene)ruthenium, Ru(C_6H_6)(C_6H_8), (2,4-dimethylpentadienyl)-(ethylcyclopentadienyl)ruthenium (DER), Ru(C_7H_{11})(C_7H_9), and bis(2,4-Dimethyl-pentadienyl)ruthenium (DMPD), Ru(C_7H_{11})$_2$. CVD growth with the precursors resulted in polycrystalline Ru films having columnar structure and poor step coverage. The precursors do not show self limiting adsorption behavior and reactivity with H_2, suggesting that the precursors are not suitable for thermal ALD in a reducing atmosphere.

2.5 REFERENCES

[1] M. Damayanti, T. Sritharan, Z. H. Gan, S. G. Mhaisalkar, N. Jian, and L. Chan, *J. Electrochem. Soc.* **153**, J41 (2006).

[2] S. M. Rossnagel and H. Kim, *Proceedings of the IEEE 2001 International Interconnect Technology Conference*, 3 (2001)

[3] International Technology Roadmap for Semiconductors, 2006 Update, http://public.itrs.net (2006).

[4] E. Eisenbraun, A. Upham, R. Dash, W. X. Zeng, J. Hoefnagels, S. Lane, D. Anjum, K. Dovidenko, A. Kaloyeros, B. Arkles, and J. J. Sullivan, *J. Vac. Sci. Technol. B* **18**, 2011 (2000).

[5] S. Kim, S. Oh, H. Kim, D. Kang, K. Kim, W. Li, S. Haukka, and M. Tuominen, *J. Electrochem. Soc.* **151**, C272 (2004).

[6] H. Kim, *J. Vac. Sci. Technol. B* **21**, 2231 (2003).

[7] H. Kim, Y. Naito, T. Koseki, T. Ohba, T. Ohta, Y. Kojima, H. Sato, and Y. Shimogaki,

Jpn. J. Appl. Phys. **45**, 2497 (2006).

[8] Q. Wang, J. G. Ekerdt, D. Gay, Y. Sun, and J. M. White, *Appl. Phys. Lett.* **84**, 1380 (2004).

[9] M. Green, M. Gross, L. Papa, K. Schnoes, and D. Brasen, *J. Electrochem. Soc.* **132**, 2677 (1985).

[10] Y. Matsui, M. Hiratani, T. Nabatame, Y. Shimamoto, and S. Kimura, *Electrochem. Solid State Lett.* **5**, C18 (2002).

[11] M. Lashdaf, T. Hatanpää, A. O. I. Krause, J. Lahtinen, M. Lindblad, and M. Tiitta, *Appl. Catal. A* **241**, 51 (2003).

[12] W. Cheng, L. Hong, J. Jiang, Y. Chi, and C. Lin, *Thin Solid Films* **483**, 31 (2005).

[13] O. Kwon, S. Kwon, H. Park, and S. Kang, *J. Electrochem. Soc.* **151**, C753 (2004).

[14] G. B. Raupp and T. S. Cale, *Chem. Mater.* **1**, 207 (1989).

[15] F. Yubero, A. R. González-Elipe, and S. Tougaard, *Surf. Sci.* **457**, 24 (2000).

[16] S. Tougaard, *Vac. Sci. Technol. A* **14**, 1415 (1996).

[17] J. Shin, D. Gay, Y-M. Sun, J.M. White, J.G. Ekerdt, in: D.G. Seiler, A.C. Diebold, R. McDonald, .R. Ayre, R.P. Khosla, S. Zollner, E.M. Secula (Eds.), *AIP Conf. Proc.* **788**, 482 (2005).

[18] N. Oshima, T. Shibutami, K. Kawano, S. Yokoyama, and H. Funakubo, *Electrochemical Society Proceedings*, **28**, 277 (2002).

[19] T. Shibutami, K. Kawano, N. Oshima, S. Yokoyama, and H. Funakubo, *Electrochem. Solid-State Lett.* **6**, C117 (2003).

Chapter 3

Growth and Characterization of Ultrathin Ru Films Grown by PVD and CVD with $Ru_3(CO)_{12}$

3.1 INTRODUCTION

Ruthenium metal has been considered for a number of microelectronics applications, including use as a copper diffusion barrier and/or copper seed layer in future ultra-large scale integrated circuit (ULSI) processing [1-4]. The interconnect applications will require ultrathin (< 5nm) continuous films, which may be deposited directly onto a dielectric or onto a refractory material, such as Ta or TiN that functions as the barrier.

At present, methods for the atomic layer deposition (ALD) or chemical vapor deposition (CVD) of Ru are limited to the use of ruthenium carbonyl ($Ru_3(CO)_{12}$) [1], cyclopentadienyl derivatives such as Cp_2Ru or $(EtCp)_2Ru$ with O_2 [5,6], and β-diketonates such as $Ru(thd)_3$ [7] or $Ru(hfac)_2$ [8] with H_2. (Cp = η^5-C_5H_5, EtCp = η^5-C_5H_4Et, thd = 2,2,6,6-tetramethyl-3,5- heptanedione, hfac = hexafluoroacetylacetonate). We have reported a low-temperature CVD process to grow a pure Ru film on Ta substrate using ruthenium carbonyl ($Ru_3(CO)_{12}$) without any co-reactant [1]; comparable film growth characteristics and properties are realized over SiO_2 as described herein. As the barrier films will necessarily be ultrathin, *in situ* characterization is preferred since this avoids complications of ambient contamination during sample transfer into analytical instruments by adventitious carbon and possible film oxidation. This chapter describes studies directed toward determining when the Ru film has become continuous and what the film thickness is at this stage in the growth process.

Low energy ion scattering spectroscopy (LEISS) in combination with X-ray photoelectron spectroscopy (XPS) are two *in situ* techniques that provide complementary information about the film and are nondestructive. Three dimensional versus two dimensional film growth introduces complications when using LEISS to establish film continuity. The issues and challenges have been discussed in the literature and Refs. 9-12 provide a good background on both [9-12]. In short, XPS samples a volume and substrate signal attenuation will not follow an exponential decay with thickness and the inelastic mean free path for the electrons if the films are rough. ISS is surface sensitive, generally to the top most layer, and relies on momentum exchange between the low energy ions and the surface atoms. Shadowing by three dimensional particles prevents the incident ions from reaching the substrate or the reflected ions from reaching the detector.

3.2 EXPERIMENTAL DETAILS

The film growth and subsequent surface analysis measurements were carried out in a film deposition and characterization facility, consisting of a load lock chamber, sample transfer system, surface analysis chamber, electrical test chamber, physical vapor deposition (PVD) chamber and CVD chamber [13]. Ruthenium films were deposited in the CVD chamber with a base pressure of 5×10^{-8} Torr. Ruthenium carbonyl precursor, $Ru_3(CO)_{12}$ (purity 99.99%, Strem Chemicals), which was loaded in a metal-glass bubbler, was heated to 366 K. Using 10 standard cubic centimeters per minute (sccm) Ar carrier gas, the evaporated precursor was delivered into the CVD chamber through a gas line and shower head, both of which were heated 10 K higher than the bubbler temperature to avoid precursor condensation. The substrate was heated between 423 K and 593 K, and the chamber pressure was maintained at 50 mTorr during film deposition. For PVD deposition, the Ru target was conditioned 5 min, in argon (50 mTorr) with 20 watt DC power and then the film was deposited in 15 s increments of sputtering using 20 watt DC and 100 mTorr of Ar.

Film composition was analyzed *in situ* using a PHI 3057 X-ray photoelectron spectrometer. For XPS analysis, Mg Kα X-rays were operated at pass energies of 117.4 eV for surveys and 58.7 eV for high-resolution scans. For LEISS a 1 kV He^+ ion beam was employed; both the incident ion beam and the detector were at 30º from the sample normal. In order to obtain a depth profile or to remove surface contamination, some films were sputtered with 5 kV Ar ions at a sample current of 1 μA.

Ex situ analysis involved transmission electron microscopy (TEM), scanning electron microscopy (SEM) and energy dispersive X-ray spectroscopy (EDS). The film surface morphology was measured using a LEO 1530 scanning electron microscope. TEM was performed with a JOEL 2010F microscope at 200 kV accelerating voltage. The TEM samples were prepared by cutting the samples with a low speed saw, mechanical polishing and final trimming with a focused ion beam (FIB) system. EDS was performed on a LEO 1530 scanning electron microscope equipped with IXRF EDS. The beam voltage was 10 kV and a 60 μm aperture was used to increase the counts.

3.3 RESULTS

CVD films grown on Ta [1] and SiO_2 at temperatures ranging from 425 – 575 K are essentially pure with less than 1% carbon or oxygen based on XPS analysis. The films grown near 425 K in CVD are characterized in TEM as polycrystalline with a columnar structure (Figure 3.1 (a)). AFM reveals the surfaces to be quite rough with an RMS roughness of 1.43 nm for a 7 nm thick film on a thermal oxide having a RMS roughness of 0.20 nm. AFM line scans have peak to valley differences as high as 7.9 nm. Figure 3.1 (b) presents representative SEM images of a film grown for 30 min and

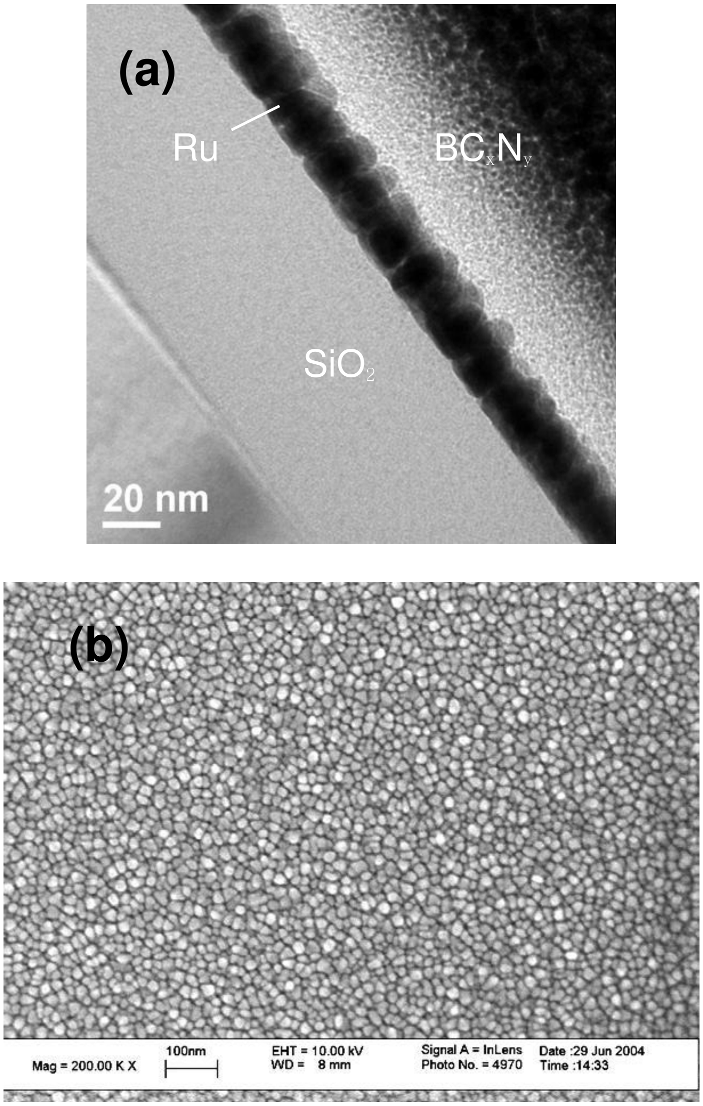

Figure 3.1 (a) TEM of a CVD film grown on SiO$_2$ for 30 min at 425K. (b) SEM image of a CVD film grown for 30 min on SiO$_2$. The average grain size appears to be ~20 nm.

it illustrates the columnar and rough nature of the CVD films. TEM studies of films on patterned wafers (not shown) reveal that this $Ru_3(CO)_{12}$ precursor gives poor step coverage and that it would not be viable for CVD growth of barriers in dual damascene processing. Nevertheless, this precursor can be used to understand the characterization issues. PVD films on thermal oxide were employed as a reference for two-dimensional growth. The PVD films were smooth and featureless in SEM (not shown). RMS roughness of 0.105 nm and line scan height differences of 0.53 nm were found for a 3.5 nm film in AFM measurements.

Figures 3.2 and 3.3 present representative XPS results for Ru deposited on SiO_2 by CVD and PVD, respectively. Figures 3.4 and 3.5 present the corresponding LEISS results for these films. For single layer alloy films, LEISS can be used to tell when one component is no longer present in the topmost layer as it will no longer be probed by the incident He ions. During film growth, and particularly during three dimensional film growth, shadowing of the substrate by the film complicates the analysis. The disappearance of a scattering peak does not necessarily mean the film is continuous. For the PVD films the Si scattering feature (Figure 3.5) is observed after 15 s of growth and absent after 30 s. Similarly, the Si scattering feature is gone after 30 min of CVD growth.

Attenuation of the substrate peak (Si 2p in this study) is used to assess film

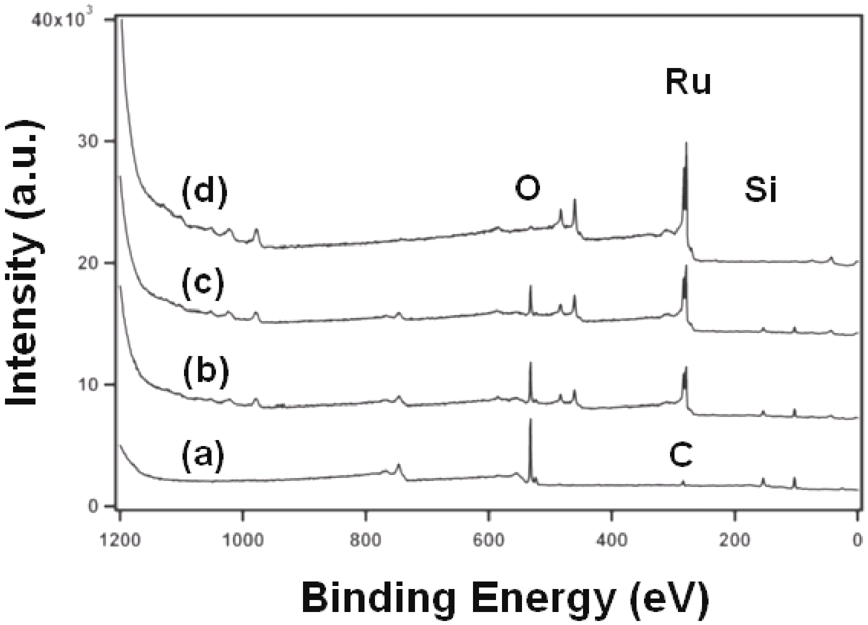

Figure 3.2 XPS survey scan of Ru grown from $Ru_3(CO)_{12}$ on SiO_2 at 425 K. (a) background, (b) 10 min, (c) 20 min, (d) 30 min.

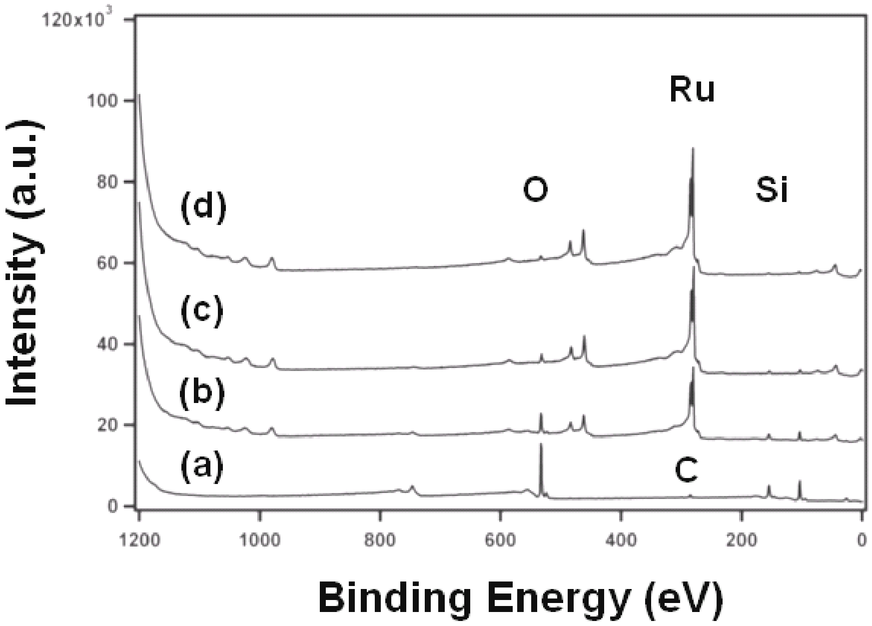

Figure 3.3 XPS survey scan of PVD Ru grown on SiO_2 at 300 K. (a) background, (b) 15 s, (c) 30 s, (d) 45 s.

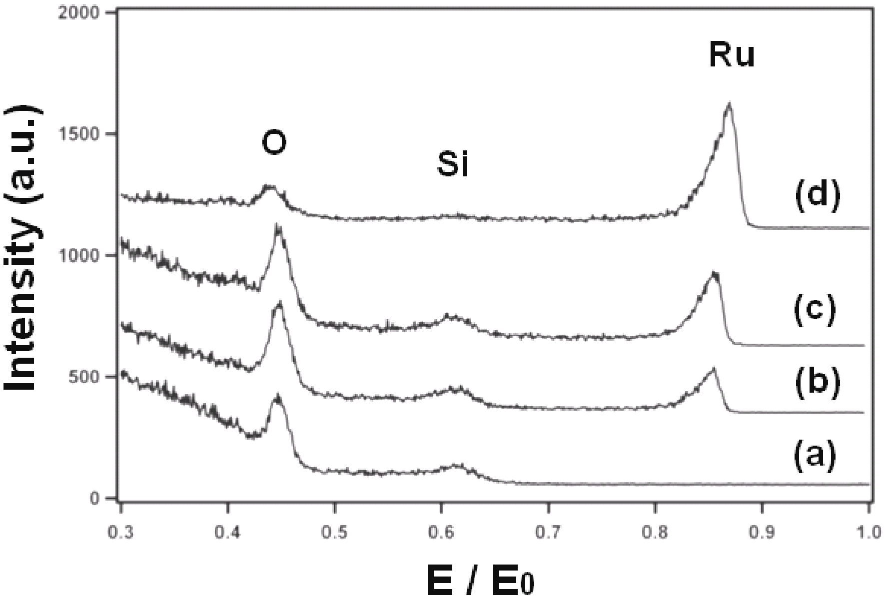

Figure 3.4 ISS of Ru grown from $Ru_3(CO)_{12}$ on SiO_2 at 425 K. (a) background, (b) 10 min, (c) 20 min, (d) 30 min. The Si feature is at the noise level for the 30 min film.

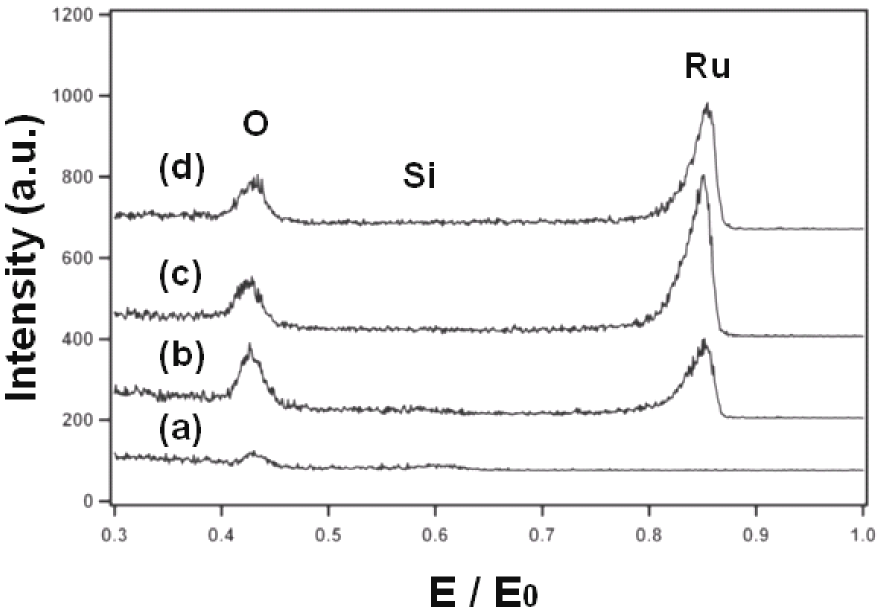

Figure 3.5 ISS of of PVD Ru grown on SiO_2 at 300 K. (a) background, (b) 15 s, (c) 30 s, (d) 45 s. The Si feature is present for 15 s and gone for 30 s.

thickness. This is reasonable for flat, continuous films such as the PVD films. The thicknesses, *d*, of the PVD and CVD films were calculated using Equation a) with λ equal to 2.73 nm for Si and θ of 30 degree. Assuming this is valid for the PVD films and using the 30 s film result, the PVD Ru films become continuous for films near 2.2 nm. A similar application of Equation 3.1 to the 30 min CVD film predicts a thickness of 3.0 nm.

$$\frac{I}{I_0} = \exp(-d / \lambda \cos\theta) \tag{3.1}$$

Figure 3.6 plots the XPS thicknesses for the CVD films. Cross section SEM results are also plotted in Figure 3.6 and illustrate this *ex situ* technique produces a very different result. The TEM image in Figure 3.1 is of the 30 min CVD film and the TEM result agrees quite well with the SEM results.

Film thickness was also probed by EDS and XPS depth profiling. More data are needed for both approaches. EDS probes a volume more than 100 nm deep and should be much less sensitive to film morphology [14]. The initial study examined two PVD films, 3.5 nm and 12 nm, in EDS; the thickness were based on XPS. Assuming a linear dependence on EDS Ru signal intensity and film thickness, a CVD film that was estimated by XPS to be 3.5 nm thick had an EDS thickness of 8.2 nm. Using argon ions to sputter the 3.5 nm PVD film and following the Ru 3d and Si 2p signals with sputtering time, a sputter profile was obtained (not shown). This was repeated for the 3.5 nm (XPS

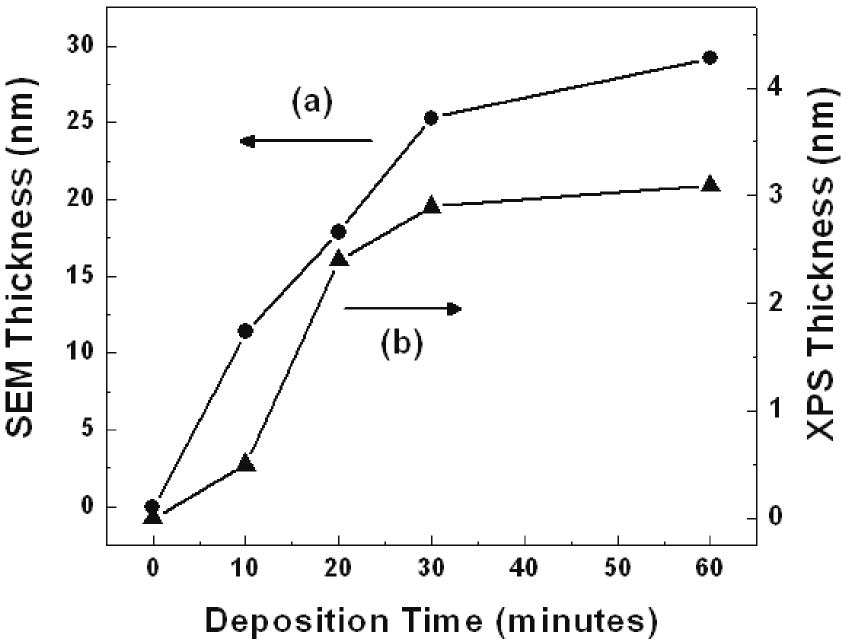

Figure 3.6 CVD film thickness based on Si 2p XPS peak attenuation and SEM analysis. The curves are drawn to guide the eye.

basis) CVD film. Assuming constant sputtering rates for the PVD and CVD films, the sputtering comparison predicts a CVD film thickness of 7.8 nm.

3.4 DISCUSSION

The film grower needs to know thickness and microstructure. If the characterization methods can be performed *in situ*, *i.e.*, without exposing the sample to ambient, one can avoid contamination of the film surface or altering the film surface through ambient exposure. XPS is a routine *in situ* technique. As we show herein, XPS can lead to underestimating the film thickness for rough films that grow in a highly three-dimensional manner. Independent *ex situ* techniques, such as AFM and SEM can reveal information on film roughness, and cross section TEM can provide an absolute measure of overall film thickness. SEM is of limited value in measuring film thickness for ultra-thin films less than 5 nm in thickness. TEM sample preparation is tedious, which limits its use to a few samples, and is not practical as a routine screening and measurement technique. Working with smooth PVD films to establish signal intensity versus film thickness, EDS could be applied as a technique to give an equivalent (to a smooth film) film thickness for rough, three-dimensional films. When combined with information on the film roughness, this equivalent EDS thickness or even the XPS thickness may be sufficient to characterize the film "thickness". Clearly, more studies are required with other Ru CVD precursors that will produce different degrees of three-dimensional growth before EDS results and XPS results can be properly related to each other.

Ultimately Ru film characterization must be coupled with electrical barrier tests to establish how film thickness and microstructure are related to barrier properties. One such technique involves preparing a Cu/barrier film/SiO_2/Si capacitor and noting if the capacitance-voltage curve shifts in a negative direction after thermal annealing, which indicates barrier failure since Cu ions have diffused through the barrier [15-17]. We will report on these studies separately and show that CVD Ru films from $Ru_3(CO)_{12}$ with an XPS-based thickness of 2.5 nm do not function as a barrier whereas Ru films with an XPS-based thickness of 4.0 nm do function as a barrier. These two films have an equivalent EDS thickness that is 2.35 times the XPS thickness, leading to 5.8 nm and 9.4 nm. If the SEM curves in Figure 3.6 are used, these films have a total thickness that is ~ 8 times the XPS values leading to 20 nm and 32 nm. The true barrier layer remains unresolved and requires further experiments.

In developing chemistries and growth processes for ultra-thin metals, one is also interested in establishing the thickness at which the film becomes continuous. In LEISS low energy ions, 1 kV He^+ in this study, scatter off the surface and energy distribution of the scattered ions proves a measure of the mass of surface atoms from which the ions scattered. For a smooth, two-dimensional film, LEISS will yield the film composition. During nonepitaxial film growth the substrate is eventually completely covered as the nucleated islands coalesce into a continuous film. Figure 3.7 (a) presents a schematic of a scattering process. The islands will have a finite height, *t*, and unless the ion gun angle and the detector angle are each at 90º, the substrate will be shadowed by the islands. Using a simple line of sight model one can examine the effect of island height, island size (*g*) and angles to determine the surface coverage α where the substrate will no longer be probed. Equation 3.2 was used to generate Figure 3.7 (b) for equal grain size and height. These results indicate that LEISS can used to follow the nucleation and growth of a film; its use to determine when the film is continuous is very dependent on the three-dimensional nature of the growth.

$$\frac{1}{\alpha_{\min}} = 1 + (1/\tan\theta + 1/\tan\delta)(t/g) \qquad (3.2)$$

LEISS and XPS can be used simultaneously to determine the growth mechanism [9]. Yubero et al. [9], and Jiménez et al. [11], report experiments that employed a 90º detector angle to follow the growth of films and plot a normalized ion scattering intensity versus the XPS intensities of a peak for the growing film and a peak for the substrate. Our experimental system has a 60º detector angle. Nonetheless, we use the same normalized ion scattering equation to compute the surface coverage and plot it versus the XPS intensity ratios (Figure 3.8) as done by Jiménez et al. The PDV curve

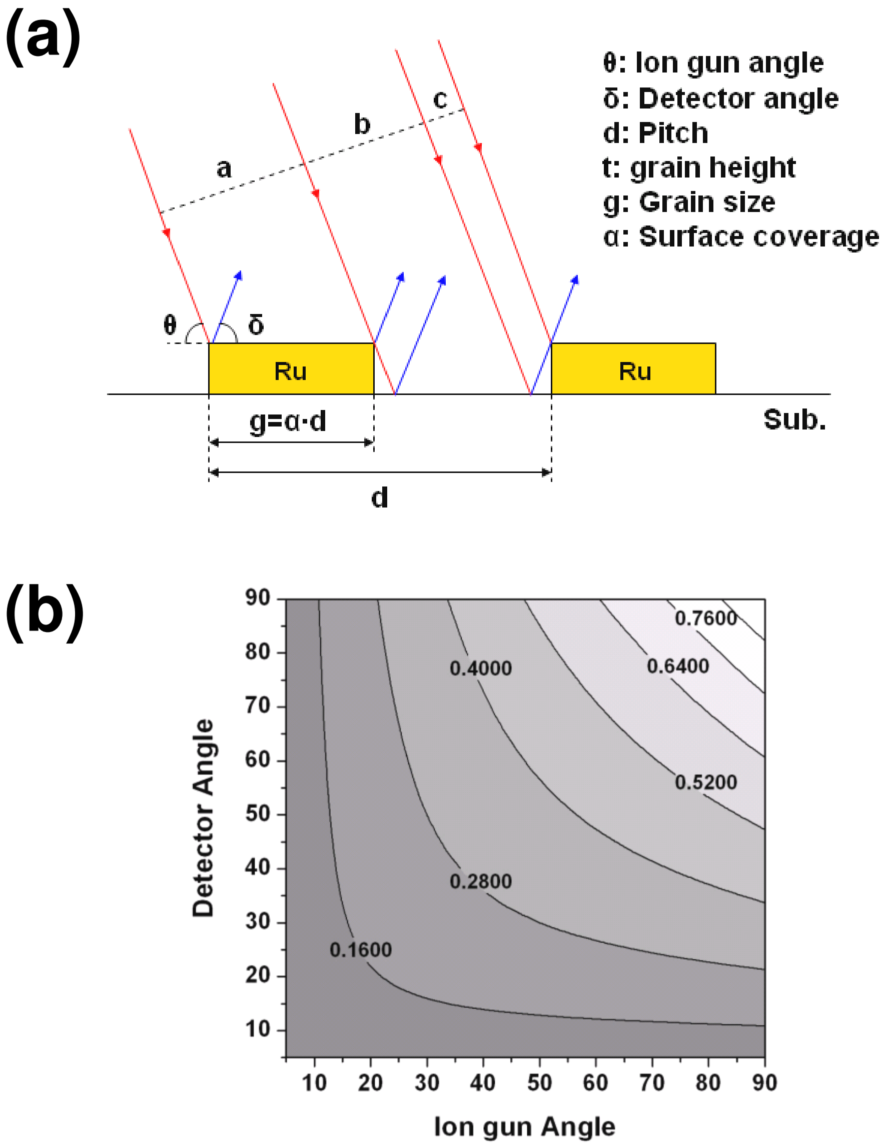

Figure 3.7 (a) Schematic showing the shadowing introduced by an overlayer island on both the incident ions and the scattered ions. (b) Plot showing the surface coverage (α) where the surface scattering signal is zero for detector and ion gun angles as defined in Fig. 8 and a grain size equal to the grain height. The experiments described herein employed detector and ion gun angles of 60º.

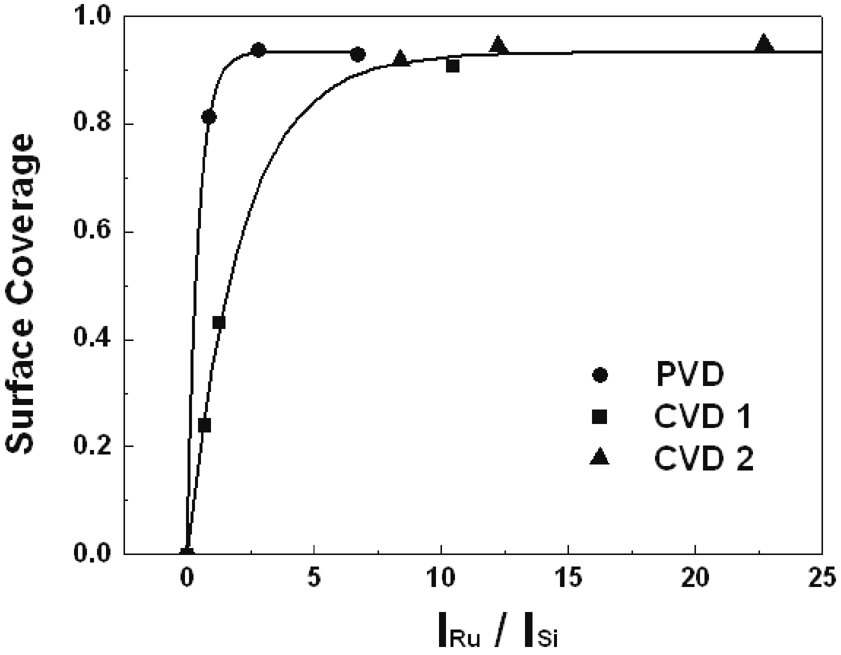

Figure 3.8 Plot based on the analysis presented by Yubero et al. The surface coverage is a normalized ratio of Ru scattering intensity to total scattering intensity and the abscissa is a ratio of XPS signals. Two different CVD growth series are presented for films grown at 425 K. The curves are not fit to any equation, they are drawn to guide the eye.

is more steep than the CVD curve and the curve shape of the PVD curve is expected when films grow in a two-dimensional mode. The more three-dimensional the growth, the higher the XPS intensity ratio before reaching saturation [11]. This interpretation is consistent with the AFM measurements and SEM measurements that showed the PVD films to be very flat and smooth.

3.5 SUMMARY

Chemical and physical methods are used to deposit Ru films on SiO_2 substrate with the goal of realizing ultrathin (3-5 nm) and continuous Ru films that can be used as copper diffusion barriers in Cu interconnect. CVD Ru films are grown from $Ru_3(CO)_{12}$ precursor at 425 – 525 K, and the films are characterized as polycrystalline with a columnar structure. Film thickness and continuity are established by using XPS and LEISS, however the shadowing effect of He^+ ions with LEISS causes considerable error in film thickness determined by XPS peak attenuation method. A surface coverage versus XPS intensity study reveals that CVD Ru follows strong 3D mode growth and thicker film is needed to fully cover SiO_2 surfaces than PVD Ru. The minimum thickness for continuous CVD Ru is determined to be ~20 nm by TEM. AFM reveals the CVD Ru films to have an RMS roughness of 1.43 nm, and the PVD films to have a roughness of 0.11 nm.

3.6 REFERENCES

[1] Q. Wang, J. G. Ekerdt, D. Gay, Y.-M. Sun, and J. M. White, *Appl. Phys. Letters* **84**, 1380 (2004).

[2] I. Goswami, R. and Laxman, *Semiconductor International* **27(5)**, 49 (2004).

[3] O. Chyan, T. N. Arunagiri, and T. Ponnuswamy, *J. Electrochem. Soc.* **150**, C347 (2003).

[4] S. Rossnagel, Solid State Technology, February 2005 Exclusive online feature#1: Deposition, www.solid-state.com 01 – 04 (2005).

[5] O. Kwon, J. Kim, H. Park, S. Kang, *J. Electrochem. Soc*. **151**, G109 (2004).

[6] T. Aaltonen, P. Alen, H. Ritala, M. Leskela, *Chem. Vap. Dep*. **9**, 45 (2003).

[7] M. Lashdaf, T. Hatanpää, A. O. I. Krause, J. Lahtinen, M. Lindblad, and M. Tiitta, *Appl. Cata. A* **241**, 51 (2003).

[8] T-M. Lu, and J. J. Senkevich, Worldwide Patent Application Number WO2004035858 (2004).

[9] F. Yubero, A. R. González-Elipe, S. and Tougaard, *Surf. Sci.* **457**, 24 (2000).

[10] S. Tougaard, *J. Vac. Sci. Technol. A* **14**, 1415 (1996).

[11] V. M. Jiménez, J. P. Espinós, and A. R. González-Elipe, *Appl. Surf. Sci.* **141**, 186

(1999).

[12] G. C. Nelson, *J. Appl. Phys*. **47**, 1253 (1976).

[13] Y-M. Sun, S. Y. Lee, A. M. Lemonds, E. R. Engbrecht, S. Veldman, J. Lozano, J. M. White, J. G. Ekerdt, I. Emesh, and K. Pfeifer, *Thin Solid Films* **397**, 109 (2001).

[14] I. E. Wach, *Characterization of Catalytic Materials*, Boston, Butterworth-Heinemann, 1992, pp 172.

[15] M. Y. Kwak, D. H. Shin, T. W. Kang, and K. N. Kim, *Thin Solid Fil*ms **339** 290 (1999).

[16] S. K. Rha, W. J. Lee, S. Y. Lee, Y. S. Hwang, Y. J. Lee, D. I. Kim, D. W. Kim, S. S. Chun, and C. O. Park, *Thin Solid Films* **320**, 134 (1998).

[17] H. Kizil, and C. Steinbruchel, *Thin Solid Films* **449**, 158 (2004).

Chapter 4

Chemical Vapor Deposition of Amorphous Ruthenium - Phosphorus Alloy Films with *cis*-$RuH_2(PMe_3)_4$

4.1 INTRODUCTION

For decades, ultra-large-scale integrated microelectronic devices have been continuously improved in functionality, operating speed and circuit density, and this has led to the use of Cu-based interconnects. While Cu provides several advantages, such as lower resistivity and higher electromigration resistance, than the Al metal it displaced, a diffusion barrier is needed since Cu readily diffuses into silicon to either act as an impurity or to form a silicide. Currently, Ta or a TaN/Ta multilayer stack is deposited by physical vapor deposition (PVD) on an interlayer dielectric as the Cu diffusion barrier, and then a Cu seed layer is deposited on the Ta for subsequent Cu electroplating [1]. However, the PVD technology used to grow Ta or the TaN/Ta multilayer stack may not be extendable to the 32-nm generation of devices and beyond where an ultra-thin (< 3 nm) and conformal barrier/cladding layer multilayer stack is required to maintain a low effective interconnect resistivity [2]. This has motivated studies on new barrier/cladding layer materials including $TiSi_xN_y$ [3], WN_xC_y [4] and Ru [5-9], and on alternate deposition technologies, such as chemical vapor deposition (CVD) and atomic layer deposition (ALD).

Ruthenium has been considered for a number of microelectronics applications, including use as a Cu diffusion barrier and Cu seed layer due to its low resistivity (~ 7 μΩ·cm), chemical stability, and low solubility with Cu [5]. However, recent studies point to some barrier limitations of Ru films. For example, a 20 nm Ru film failed to prevent Cu diffusion above 725 K, and a 5 nm Ru film lost its barrier property above only 575 K [10,11]. Ruthenium films can be grown by CVD or ALD methods using precursors such as, Ru carbonyl ($Ru_3(CO)_{12}$) [6], cyclopentadienyl derivatives such as Cp_2Ru [7] or $(EtCp)_2Ru$ [8], and β-diketonates such as $Ru(thd)_3$ [9], (Cp = η^5-C_5H_5, Et = C_2H_5, EtCp = η^5-C_5H_4Et, thd = 2,2,6,6-tetramethyl-3,5-heptanedione). In general, Ru films deposited by CVD or PVD methods follow a 3D, Vollmer-Weber growth mechanism, due to its high surface energy ($\gamma_{Ru(001)} = 3.05$ J/m^2) [12] and this leads to polycrystalline, columnar films. Fast Cu diffusion can occur through grain boundaries due to the much higher diffusion at grain boundaries than in the bulk [13]. If the poor barrier capability of thin Ru films is rooted in their columnar structure, controlling the microstructure of Ru films is essential in improving barrier properties. Changing the Ru film microstructure from polycrystalline to nanocrystalline or from polycrystalline to amorphous should eliminate or suppress the fast diffusion of Cu through grain boundaries.

Herein we report the CVD growth of nearly amorphous Ru-P alloy metal films by employing *cis*-$RuH_2(PMe_3)_4$ (Me = CH_3) as the precursor. Amorphous metallic alloy films and powders grown by plasma enhanced-ALD, PVD, CVD, reduction of metal ions in solution, or electroless deposition have been reported for TaN_x, Ta-Ru-N, FeB, NiP_x, NiB_x, and CoW_xP_y [14-18]. Studies have shown these films to be metastable and undergo crystallization at high annealing temperatures [14,16-18]. Much can likely be learned about the structure, formation driving forces, and stability of the amorphous metal alloy films from the literature on bulk metallic glasses [19-24]. To that end, and borrowing from the approaches applied to bulk metallic glasses, we also report *ab initio* molecular dynamics simulations that provide insight into the local structure of amorphous Ru-P alloys. The first principles approach [24] has allowed us not only to establish a realistic description of glassy structures but also to develop a detailed understanding of the origin of short-to-medium range order often seen in amorphous alloy structures.

4.2 EXPERIMETAL DETAILS

Film growth was carried out in a deposition and analysis facility consisting of a vacuum sample transfer system, load lock, X-ray photoelectron spectroscopy (XPS) system (Physical Electronics 3057; Mg Kα), CVD chamber, and a PVD chamber equipped with DC magnetron sputtering. The stainless steel CVD chamber is a cold-wall vessel (base pressure 5×10^{-8} Torr) and the SiO_2/Si(100) substrates were heated radiatively from below. Thermally grown SiO_2 (100 nm)/Si(100) 200 mm wafers were supplied by Sematech. The wafers were cut into 20 × 20 mm pieces and heated to the growth temperature under vacuum. *cis*-$RuH_2(PMe_3)_4$ was synthesized according to procedures described below; the solid compound was sublimed at 353 K to obtain sufficient vapor pressure and delivered to the CVD chamber using flowing Ar through a heated gas line and shower head. The deposition was carried out at ~200 mTorr. *Ex situ* XPS chemical state analysis was performed with a Physical Electronics 5500, which is fitted with a monochromatic Mg Kα source. Crystallinity is established using grazing angle (2°) X-ray diffraction (XRD) (Bruker-Nonius D8), cross section transmission electron microscopy (TEM) (JOEL 2010F operated at 200 kV) and selected area diffraction (SAD).

The precursor, *cis*-$RuH_2(PMe_3)_4$, was prepared by a modification of the published procedure from *trans*-$RuCl_2(PMe_3)_4$ and the intermediate borohydride derivative [25,26]. All reactions were performed under a dry, oxygen-free nitrogen atmosphere or under vacuum using standard Schlenk line and dry box techniques. Solvents were dried prior to use by distillation from CaH_2. Sodium borohydride was purchased from Fisher Scientific and dried under vacuum overnight prior to use. Trimethylphosphine (97%) was purchased from Aldrich and used without further purification. Trimethylphosphine (4.5 g, 60 mmol) was added to a stirred solution of $RuCl_3\cdot xH_2O$ (2.7 g, 13 mmol) in methanol (30 mL) at 298 K. The mixture was stirred (18 hr) at 298 K during which time a yellow precipitate formed. The solid was isolated by filtration, then dried under vacuum, and used in the next step without further purification. (Isolated: *trans*-$RuCl_2(PMe_3)_4$, 3.8 g, 81% as a greenish yellow solid, m.p. 503-510 K, (dec. 462-466 K). Methanol (1.0 to 1.5 mL) was added dropwise, slowly until violent gas evolution was observed to a stirred mixture of *trans*-$RuCl_2(PMe_3)_4$ (1.1 g, 2.3 mmol) and sodium borohydride (730 mg, 19 mmol) in benzene (70 mL) at 298 K. The mixture was stirred (2 hr) at 298 K after which the solvent was removed under vacuum. The brown residue was extracted with hexane, and filtered through a short bed of Celite®. The filtrate was evaporated to dryness under vacuum to 6 give a bright yellow solid. (Isolated: *mer*-$(PMe_3)_3RuH(\eta^2\text{-}H_2BH_2)$, 650 mg, 82% as a bright yellow solid, m.p. 378 – 381 K.) Trimethylphosphine (460 mg, 6 mmol) was added dropwise to a stirred solution of *mer*-$(PMe_3)_3RuH(\eta^2\text{-}H_2BH_2)$ (1.04 g, 3 mmol) in benzene (80 mL) at 298 K. The yellow mixture was stirred at 298 K until it was nearly colorless (faintly brown after 1 hr), then the solvent was evaporated under vacuum. The crude, light brown solid was sublimed (353 K, 1×10^{-2} Torr) onto a 195 K cold probe. (Isolated **1**: 740 mg, 86% as a white solid.)

The surface science study was conducted in an ultra-high vacuum chamber equipped with a cryogenic pump to maintain a base pressure of 5.2×10^{-10} Torr during XPS analysis and a diffusion pump that maintains a base pressure of 1.1×10^{-9} Torr for precursor dosing and temperature programmed desorption (TPD). TPD and XPS were done *in situ* on an Extrel C50 quadrapole mass spectrometer and a PHI 5000C ESCA system, respectively. *cis*-$RuH_2(PMe_3)_4$ was heated to 353 K while the stainless steel tubing and valves were heated to 363 K to prevent deposition in dosing lines. *cis*-$RuH_2(PMe_3)_4$ was introduced into the chamber using an uncalibrated, pin-hole doser, and dosed onto a polycrystalline tantalum foil heated resistively and cooled by liquid nitrogen. XPS peaks are shifted to give C 1s at 285.0 eV. The tantalum foil contained small amounts of oxygen that could not be removed by heating, annealing or ion sputtering and is referred to herein as a sub-oxide (TaxOy) foil. The sample was regenerated using an Ar^+ ion gun to remove any Ru that was deposited and annealed to 1275 K to heal the ion damage.

For the construction of model amorphous Ru-P alloy structures used in our theoretical analysis, we began by randomizing Ru in a periodic supercell and then replaced a given fraction of Ru with P. Next, the alloy was melted at high temperatures (3500 K) for 3 picoseconds (ps) with a time step of 1 femtosecond (fs), using *ab initio* molecular dynamics (MD) within a Born-Oppenheimer framework, and then quenched to 500 K at a rate of 1.5 K/fs, followed by static structural optimization. Here the temperature was controlled using velocity rescaling. Our *ab initio* MD simulations were performed within the generalized gradient approximation (GGA-PW91 [27]) to density functional theory (DFT) using the well established Vienna *ab initio* Simulation Package

(VASP) [28-30]. A planewave basis set for valence electron states and Vanderbilt ultrasoft pseudopotentials for core-electron interactions were employed. A plane-wave cutoff energy of 300 eV was used and the Brillouin zone integration was performed using one k-point (at Gamma). The $Ru_{80}P_{20}$ amorphous alloy system reported herein was modeled using a periodic 144-atom supercell (consisting of 115 Ru and 29 P atoms) with an optimized volume of 2 nm^3 at 0 K. While no simulation study has been reported for the Ru-P system, our $Ni_{80}P_{20}$ structure obtained using the same procedure shows excellent agreement with that from previous extensive *ab initio* MD simulations [24]. This confirms the soundness of our approach.

4.3 RESULTS

4.3.1 Film Growth Studies

The precursor is a solid that sublimes intact at temperatures as high as 405 K. Figure 4.1 presents mass sweeps of the vapor space above the precursor as it was heated from room temperature to 405 K. *cis*-$RuH_2(PMe_3)_4$ has a molecular weight of 407 and the appearance of fragmentation peaks at 345 K and 405 K for masses 406, 393 and 330 are indicative of the compound. The additional peak for masses 93, 107, and 185 are contaminants associated with synthesis. $RuH_2(PMe_3)_4$ was heated to 353 K during growth.

Film growth was possible above 525 K. The XPS survey scans in Figure 4.2 show

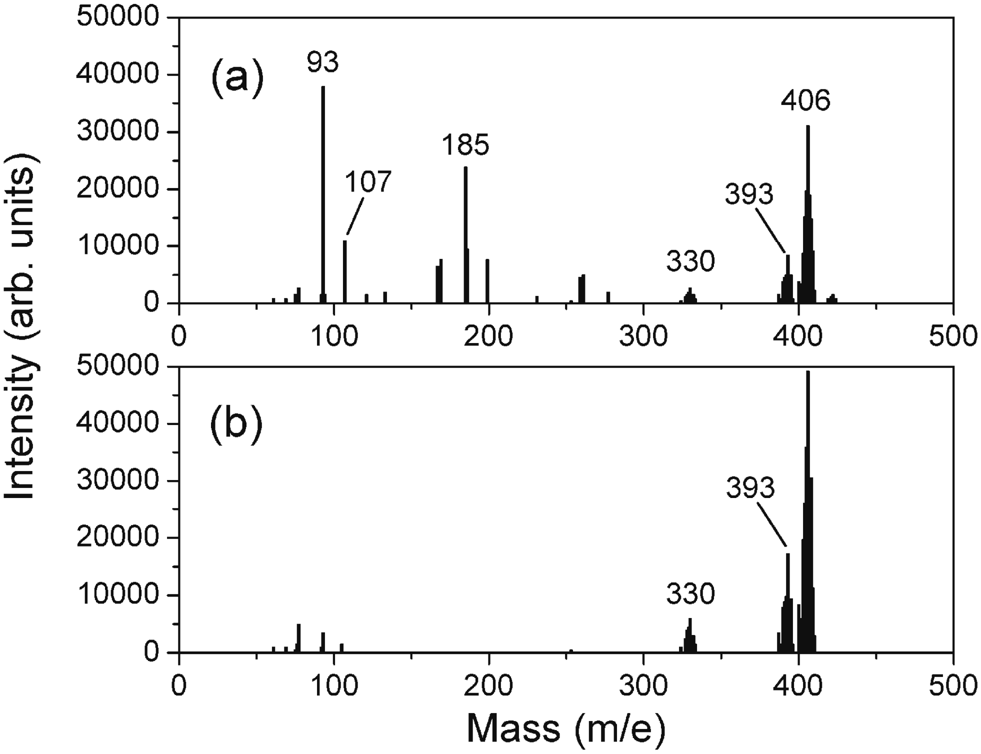

Figure 4.1 Electron impact ionization analysis of the vapor produced during sublimation at (a) 345 K and (b) 405 K.

the films contain Ru and P. The Si (104.3 eV) and O (533.5 eV) features are associated with the 100 nm-thick thermal oxide/Si(100) substrate. Under the conditions of our growth (1hr, 200 mTorr pressure, dosing geometry) a continuous film was not realized at 525 K, and a continuous 30 nm Ru film (see below) grew at 575 K. The chemical state of Ru is metallic for the films grown at 525 and 575 K, as indicated by the binding energy of the Ru $3d_{5/2}$ peak at 280.0 eV. A weak Ru $3d_{5/2}$ peak that is not apparent in Fig. 2 is present at 281.2 eV for the 475 K film, which is attributed to Ru in adsorbed or partially decomposed precursor molecules. Figure 4.3 shows XPS depth profile results of the films deposited at 525 and 575 K, indicating that higher substrate temperatures resulted in a higher P concentration and that both films have higher P concentrations near the film surface than in the bulk. The P concentrations near the surface are 13 % and 28 % for the 525 K and 575 K films, respectively, and continuously decrease with sputtering. The P concentration of the 525 K film dropped to near zero after 45 s of sputtering as the film was removed, while the 575 K film shows ~15 % of P concentration after 105 s of sputtering. (The O and Si signals in Figure 4.3 (a) are associated with the SiO_2 because the film was not continuous.) The cause(s) for a P profile were not revealed in this study; there may be a surface enrichment associated with cooling the sample in the growth chamber to 325 K, during which time residual precursor and precursor decomposition products can adsorb on the surface.

Figure 4.4 shows high resolution Ru 3d and P 2p XPS peaks for the film grown at

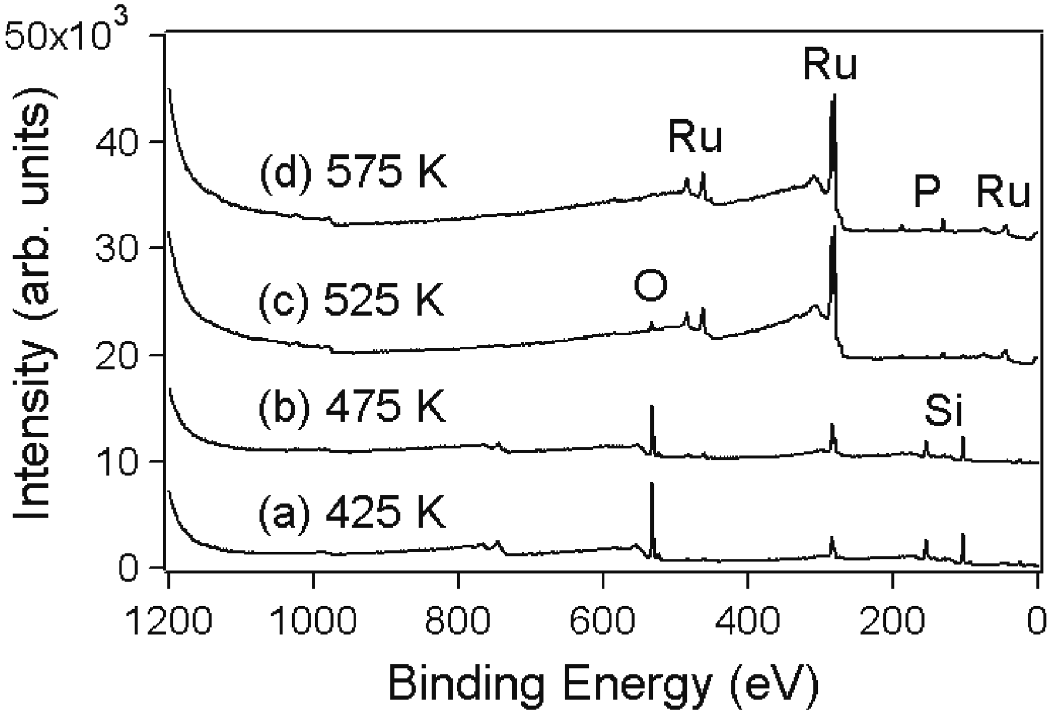

Figure 4.2 XPS survey scan results of the Ru films deposited with *cis*-$RuH_2(PMe_3)_4$ at different substrate temperatures. (a) 425 K, (b) 475 K, (c) 525 K, and (d) 575 K.

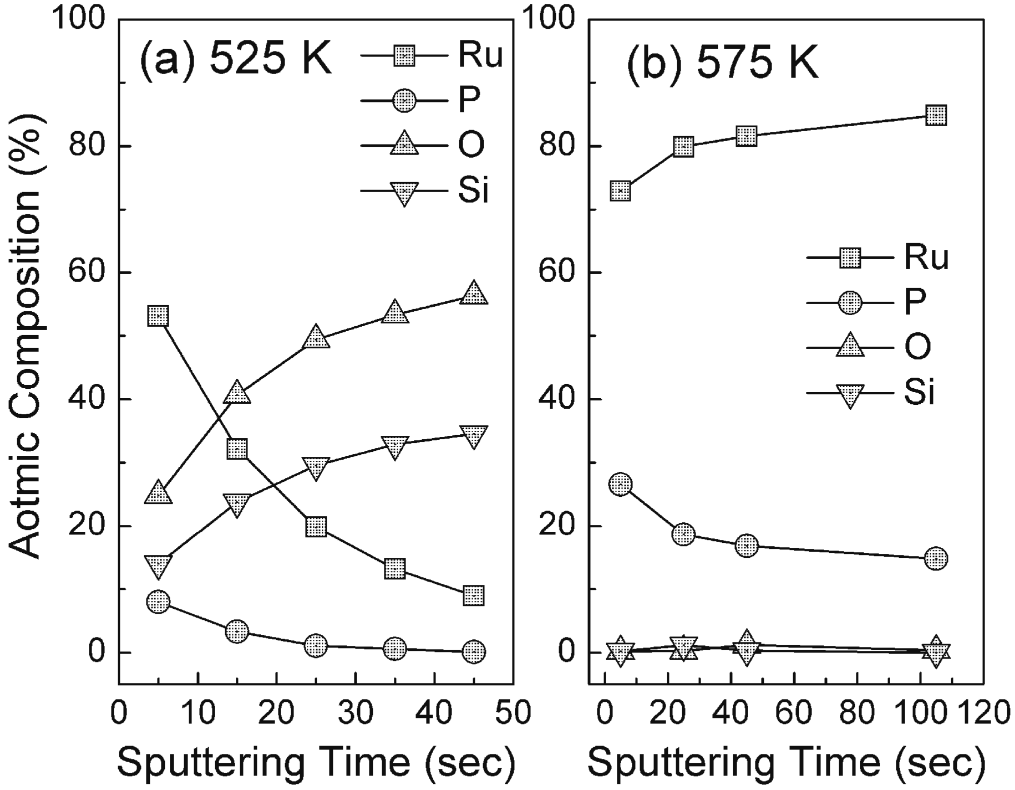

Figure 4.3 XPS depth profile of the atomic concentration of the Ru films grown at (a) 525 K and (b) 575 K.

575 K. Because of the overlapping Ru $3d_{3/2}$ and C 1s peaks, the C content cannot be obtained directly from XPS measurements. However, this can be overcome by fitting the Ru $3d_{5/2}$ and $3d_{3/2}$ peaks, assuming pure Ru has a peak intensity ratio of 1.5 based on the relative degeneracy of the 3d doublet peaks [31]. The Ru-P film grown at 575 K is determined to contain 10.5% C. The P $2p_{3/2}$ peak at 129.8 eV indicates P is present in the zero-valent state and is not donating or accepting electrons with Ru [32]. The 525 K film also has a P $2p_{3/2}$ peak at 129.8 eV.

The surface morphology of a 30 nm thick Ru-P film deposited at 575 K was inspected by scanning electron microscopy and the micrographs (not shown) reveal a smooth surface without observable grain boundaries. Atomic force microscopy measurements of this film lead to an RMS roughness of 0.52 nm. For comparison a 3.5 nm PVD Ru film has a 0.11 nm RMS roughness, and the SiO_2/Si(001) substrate has a 0.20 nm roughness. The smooth surface of the 575 K-CVD film can be seen in the cross section TEM image in Figure 4.5a and contrasted against the PVD film.

Grazing angle XRD results for a 575 K-CVD film, 30 and 5 nm PVD films, and a 30 nm Ru film grown by thermal CVD at 525 K from $(2,4\text{-dimethylpentadienyl})_2Ru$ are presented in Figure 4.6. The PVD films and an additional CVD film were examined to ensure the grazing angle technique would be sensitive enough for ultrathin films. The 30 nm CVD film deposited with $(2,4\text{-dimethylpentadienyl})_2Ru$ and the 20 nm thick PVD

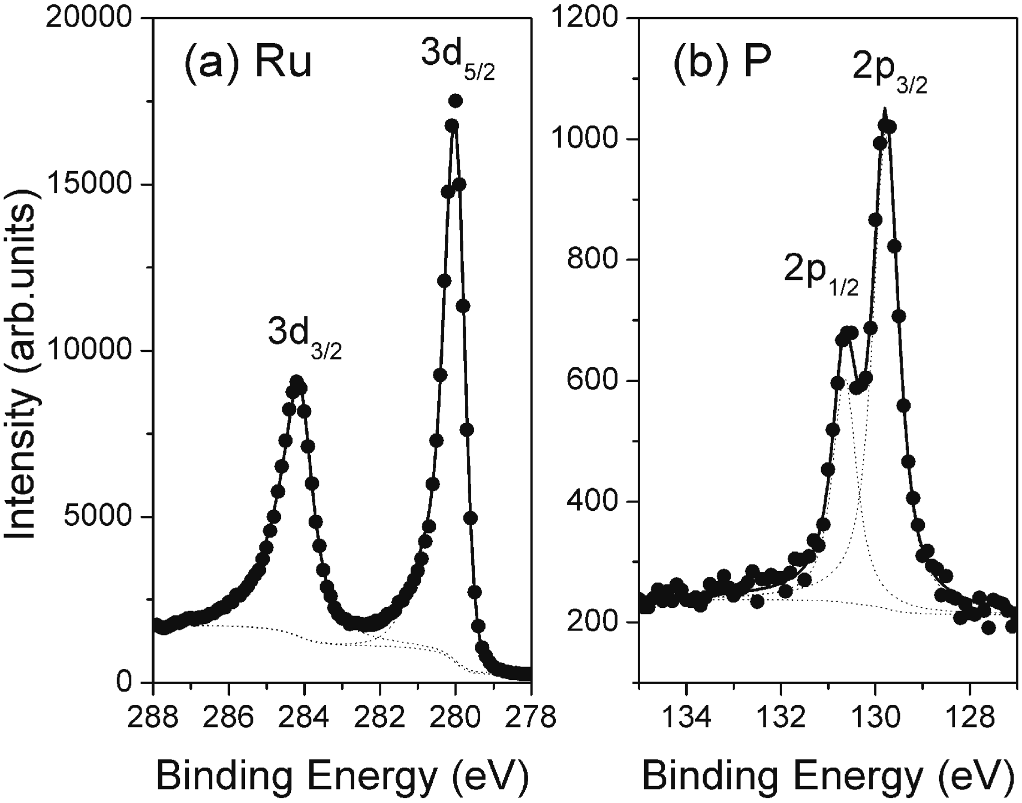

Figure 4.4 High resolution XPS result of the (a) Ru 3d and (b) P 2p peaks for a film deposited at 575 K.

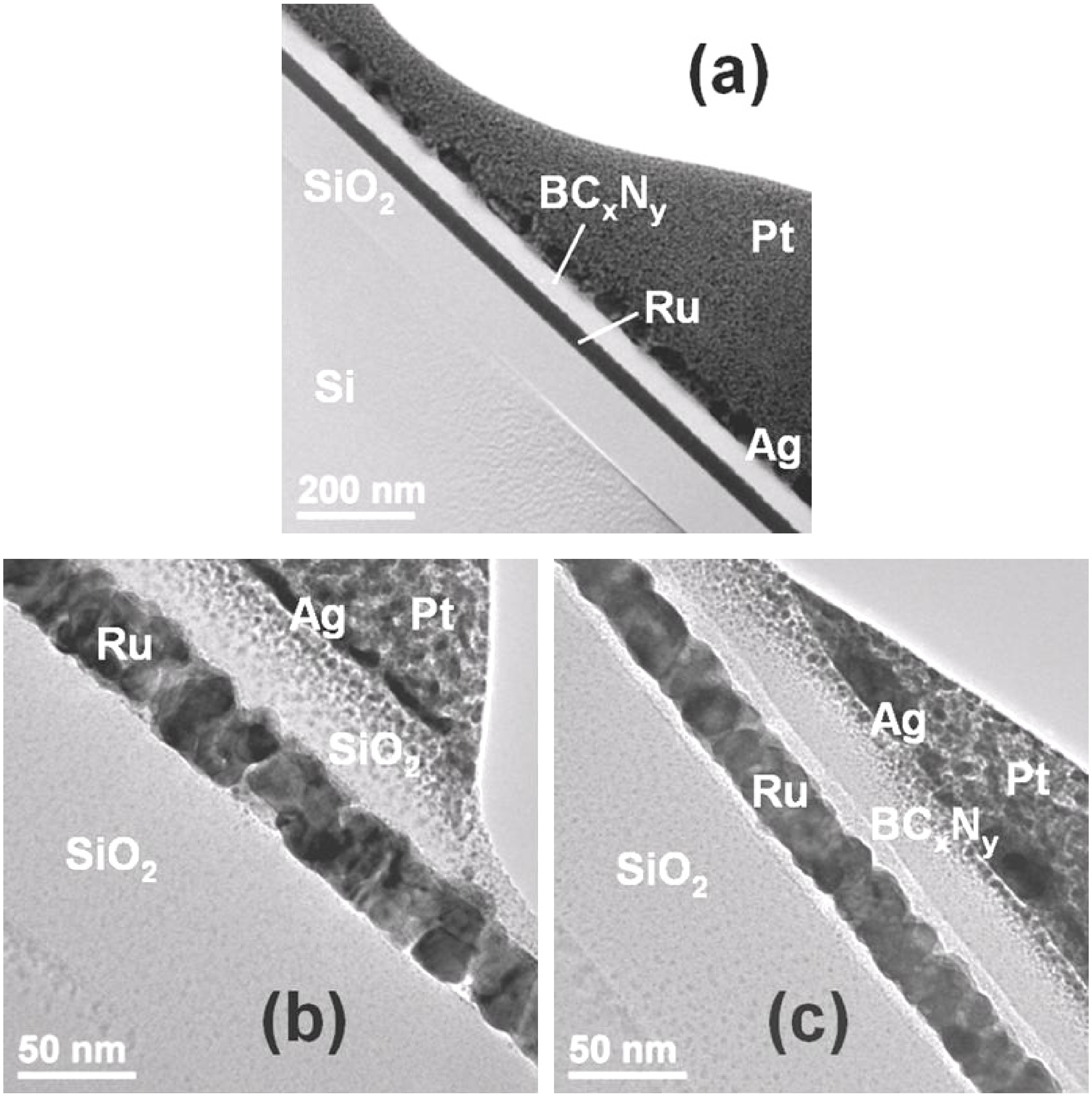

Figure 4.5 Cross section TEM of (a) the Ru-P film grown by CVD at 575 K, (b) a 30 nm PVD Ru film, and (c) the Ru-P grown at 575 K and annealed to 975 K for 30 min.

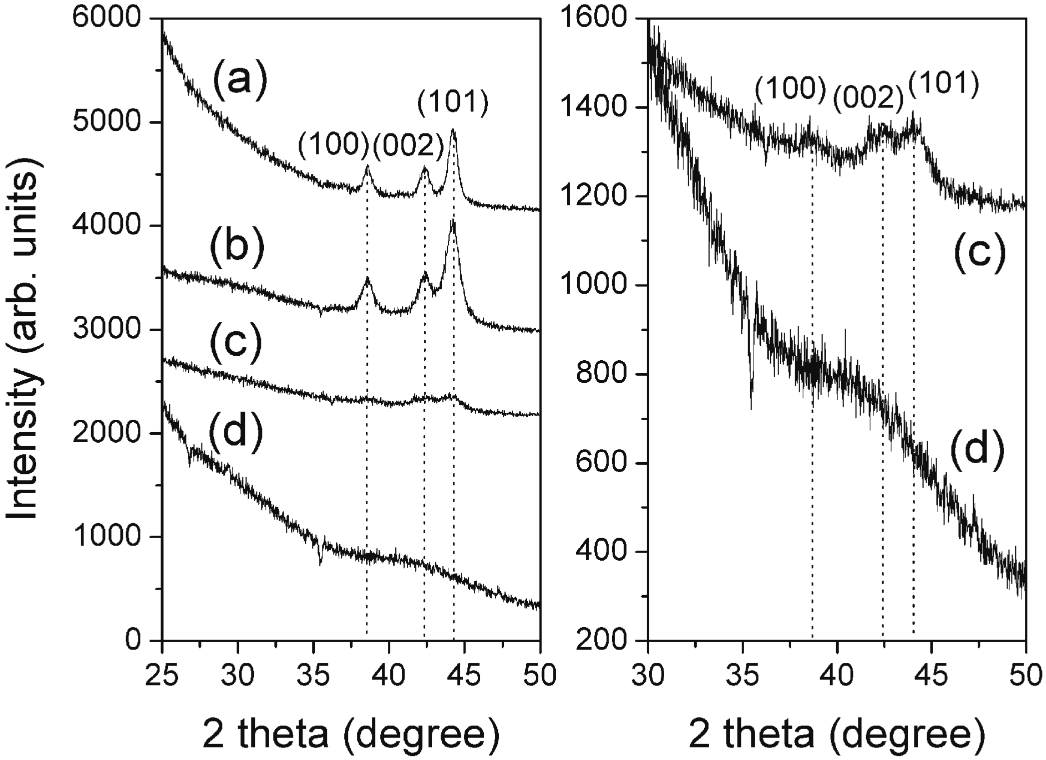

Figure 4.6 XRD of Ru films. (a) 20 nm PVD Ru, (b) 30 nm CVD Ru deposited with $Ru(C_7H_{11})_2$, (c) 5 nm PVD Ru, and (d) 30 nm CVD Ru-P deposited with $RuH_2(PMe_3)_4$.

film show clear peaks at 2θ = 38.6°, 42.4°, and 44.2°, which represent the (100), (002), and (101) planes of the hexagonal close packed Ru lattice, respectively [33]. The 5 nm PVD film also shows peaks at the same positions that indicate the film is polycrystalline Ru, although the peaks are quite weak due to its low thickness. In contrast, no peak was observed for the film grown with *cis*-$RuH_2(PMe_3)_4$, suggesting that the film is amorphous or has nano-crystallites that are too small to be detected by XRD; *i.e.*, an XRD-level amorphous film [34].

The microstructure of the Ru-P film deposited at 575 K was also analyzed using dark field TEM (Figure 4.7) and SAD pattern measurement (Figure 4.8b). Note the TEM sample preparation involves coating the CVD Ru film with a BC_xN_y film in a process that takes 3 hr at 635 K. Generally, Ru films deposited by a CVD or PVD method are polycrystalline having columnar structures, however the films grown with *cis*-$RuH_2(PMe_3)_4$ show a significantly different microstructure. The SAD pattern (Figure 4.8b) does not feature a sharp ring or spot pattern, while the PVD film pattern (Figure 4.8a) has a well-developed spot pattern. The sharp spot pattern is expected for the PVD film based on the XRD results (Figure 4.6) and separate TEM images (not shown). A diffuse ring pattern can be observed from films composed of extremely small crystallites, which cause overlapping of crystalline diffraction lines with broadening, or can be observed from amorphous films having a random microstructure [35]. The criteria and transition between the two cases (*i.e.*, nanocrystalline versus

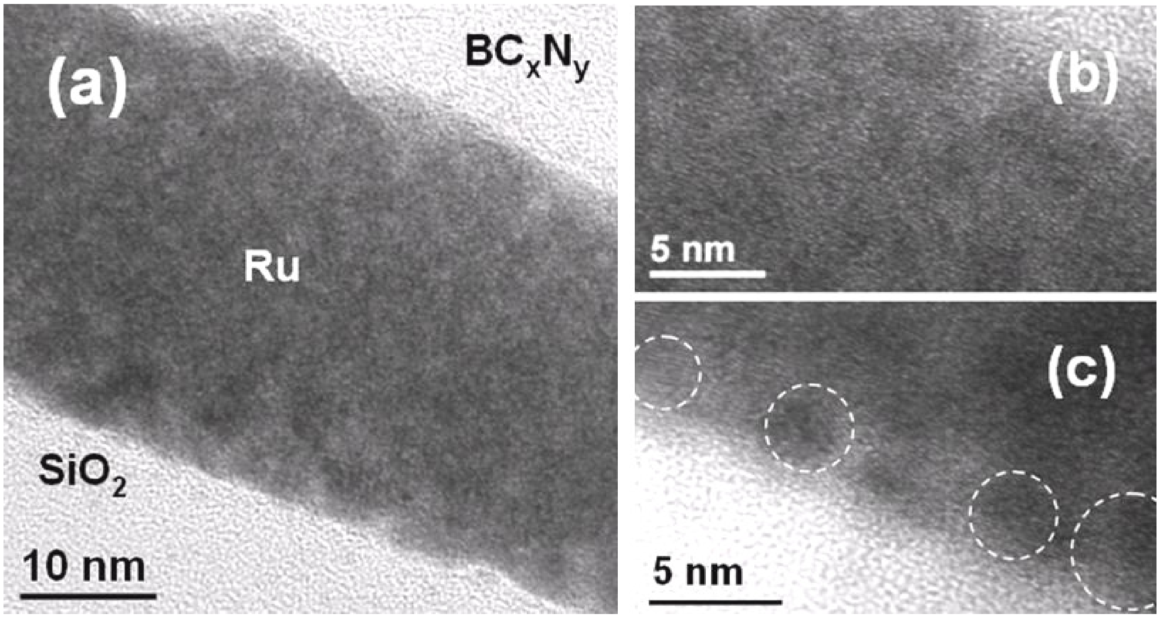

Figure 4.7 Dark field TEM image of the 30 nm CVD Ru-P film deposited with cis-RuH$_2$(PMe$_3$)$_4$ at 575 K for 1h. The circles are drawn to indicate where crystalline regions are detected. Panel (a) presents the cross section of the entire sample and Panels (b) and (c) present close up views of the Ru-P film near the growth surface and at the SiO2 substrate, respectively.

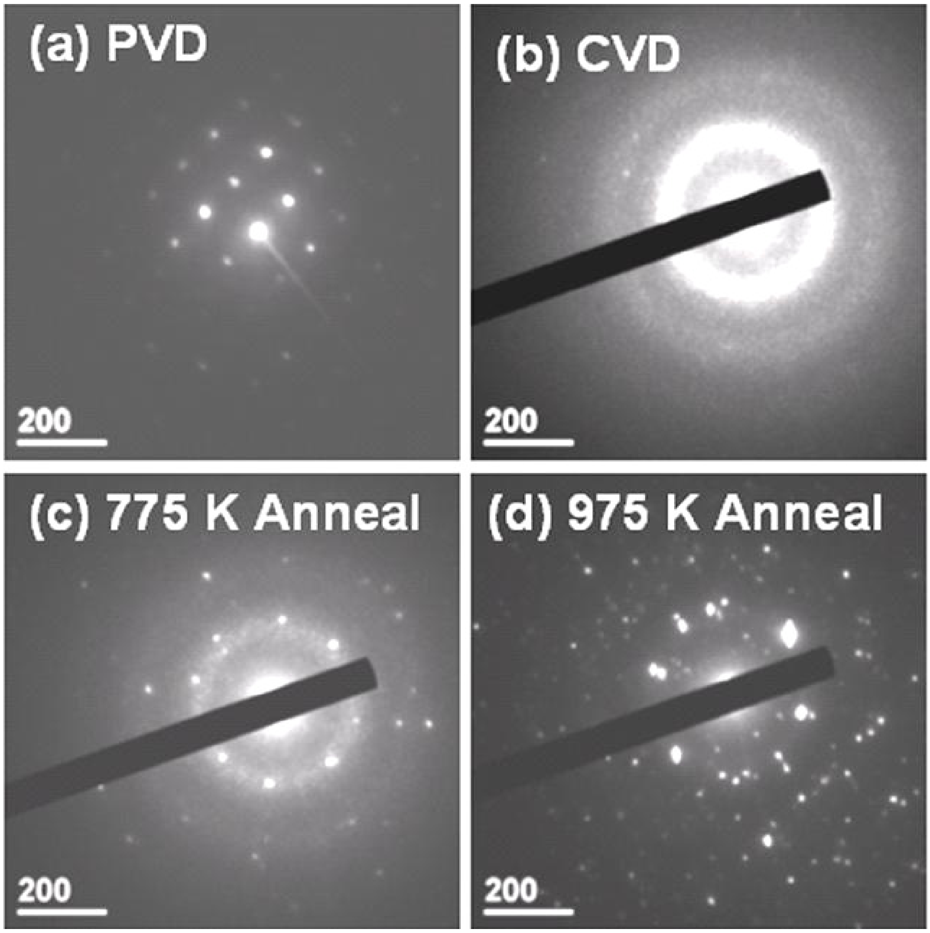

Figure 4.8 SAD patterns of (a) a PVD Ru film, (b) a CVD Ru-P film grown at 575 K, (c) the Ru-P film annealed to 775 K for 30 min, and (d) the Ru-P film annealed to 975 K for 30 min.

amorphous) are not clear because amorphous microstructures have some degree of local order.

The Ru-P film deposited with *cis*-$RuH_2(PMe_3)_4$ shows an amorphous-like random microstructure, however small crystallites a few nm in size were observed, especially near the SiO_2 substrate rather than near the film surface. The Ru-P alloy films are metastable and become increasingly more crystalline upon annealing to 775 or 975 K. Figure 4.9 presents the dark field TEM image of the 575 K-CVD film after it was annealed in vacuum to 775 K for 30 min. Figure 4.5c presents a cross section of the film after annealing to 975 K. The SAD patterns in Figure 4.8 illustrate the appearance of definite spots at 775 K and then well-developed spots at 975 K. Most of the film adjacent to the SiO_2 substrate appears polycrystalline in Figure 4.9. The small crystallites that formed during deposition at 575 K (Figure 4.7) could have acted as nuclei for crystallite growth upon annealing to 775 K. The TEM image in Figure 4.5 demonstrates the polycrystalline film has a large grain structure after annealing to 975 K. Chemical mapping studies using electron energy loss spectroscopy were not performed to determine if there was any segregation of the P under high temperature annealing.

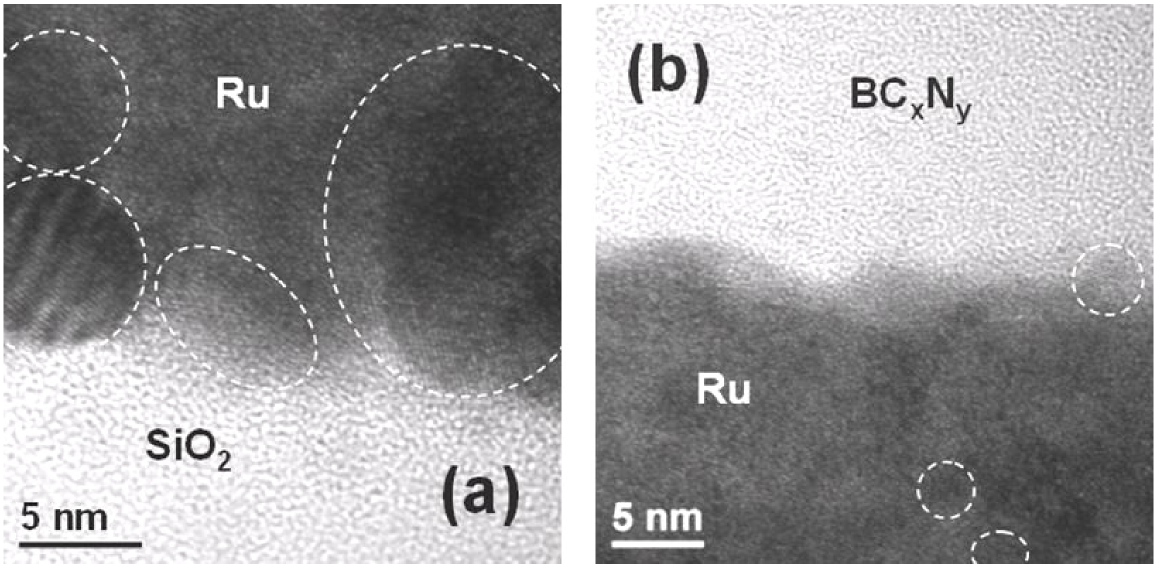

Figure 4.9 Dark field TEM image of the 30 nm CVD Ru-P film deposited with cis-RuH$_2$(PMe$_3$)$_4$ at 575 K for 1h and annealed at 775 K for 30 min. The circles are drawn to indicate where crystalline regions are detected. Panel (a) is a view of the film against the SiO2 substrate and Panel (b) is a new near the growth surface.

4.3.2 Surface Studies [This section is principally the work of Wyatt Winkenwerder.]

A 5.9 Langmuir (L) dose of *cis*-$RuH_2(PMe_3)_4$ was delivered to a Ta_xO_y surface heated at 455 K. The Ru $3d_{3/2}$ and C 1s photoelectrons contribute to the broad feature seen at 285 eV in Figure 4.10 after dosing, indicating a partially decomposed precursor is present at the surface. The P 2p XPS peaks (not shown), if present, were at the noise level since the Ru 3d electrons are ten times more sensitive than the P 2p electrons in XPS [36] and the signal-to-noise ratio for Ru 3d in Figure 4.10 is 4:1. Only the m/e 15 signal produced a peak at 560 K during TPD. After TPD the 285 eV XPS peak is more narrow, and the Ru $3d_{5/2}$:$3d_{3/2}$ peak ratio is consistent with partial loss of C from the surface. The peak ratio goes from 0.69 before to 0.91 after TPD to 975 K. (Ru containing < 1 % C has a Ru $3d_{5/2}$:$3d_{3/2}$ peak ratio of 1.5.)

A 0.17 L dose of the precursor was condensed at 135 K and subjected to TPD. Figures 4.11 and 4.12 present the Ru 3d and P 2p signals. The Ru $3d_{5/2}$ feature appears at 280.2 eV and the P 2p signal is centered at 131.5 eV. Note the P $2p_{1/2}$ and $2p_{3/2}$ doublet (Figure 4.4) is not resolvable with the *in situ* PHI 5500C system as it does not feature a monochromatic X-ray source. Subsequent TPD of the adsorbed species produces the spectra presented in Figure 4.13. Additional masses were monitored, m/e 46 ($P(CH_3^+)$, 61($P(CH_3)_2^+$) and 330 ($RuH_2(P(CH_3)_3^+$) and their signals mirrored the m/e

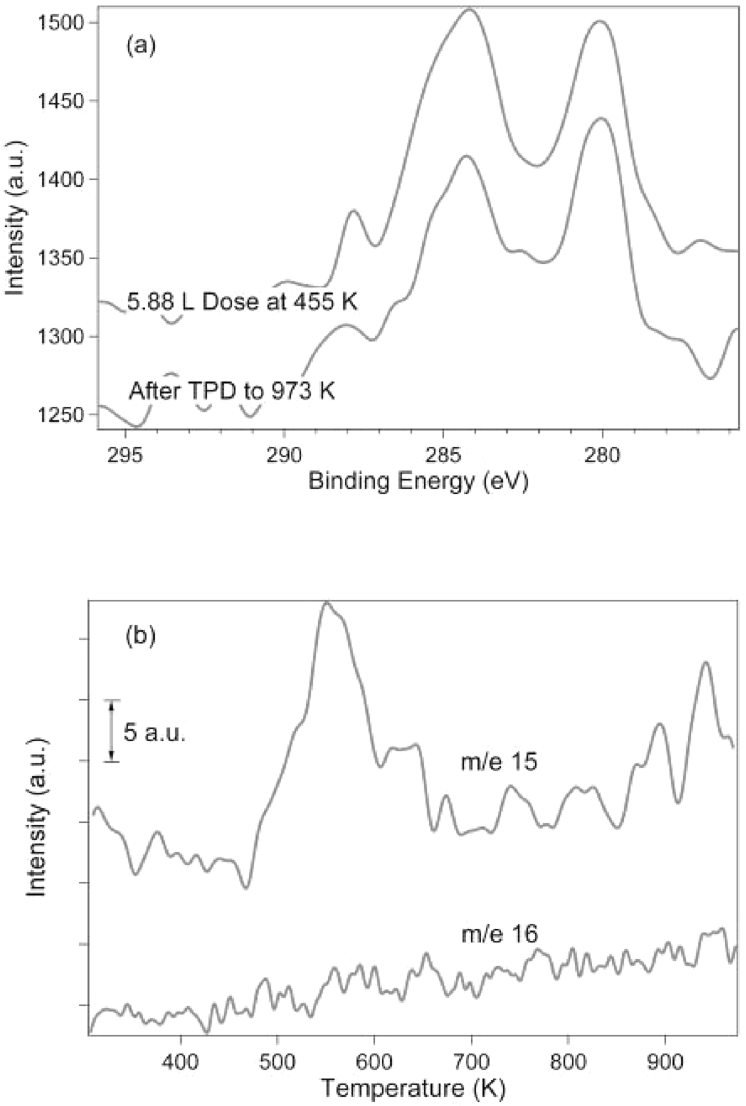

Figure 4.10 6.24 L dose of *cis*-RuH2(PMe3)4 at 455 K on TaxOy: (a) Ru 3d and C 1s XPS spectra and (b) TPD results.

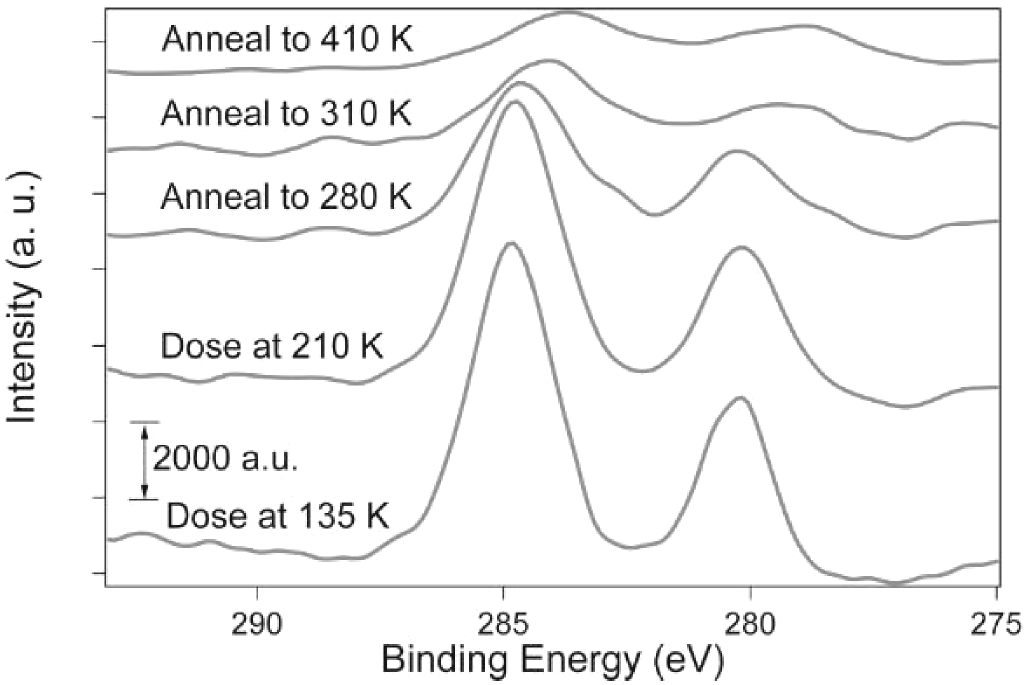

Figure 4.11 Ru 3d and C 1s XPS spectra resulting from a 0.17 L dose of *cis*-$RuH_2(PMe_3)_4$ at 135 K, and resulting from a 0.018 L dose of *cis*-$RuH_2(PMe_3)_4$ at 210 K followed by annealing to the indicated temperatures and cooling back to 210 K to record the spectra.

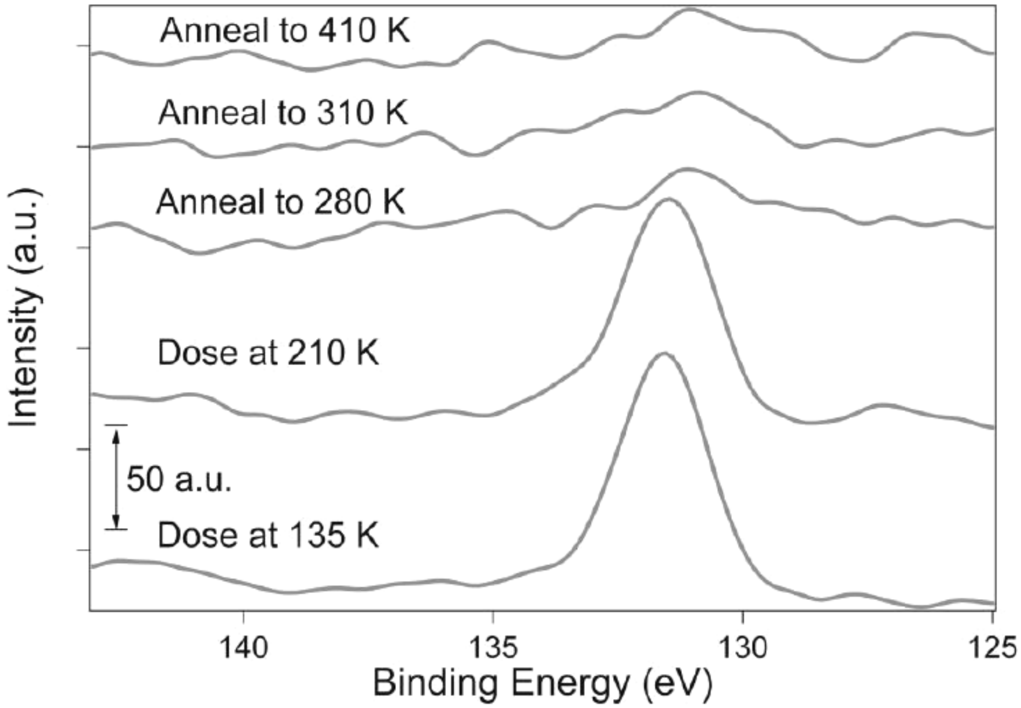

Figure 4.12 P 2p XPS spectra resulting from a 0.17 L dose of *cis*-$RuH_2(PMe_3)_4$ at 135 K, and resulting from a 0.018 L dose of *cis*-$RuH_2(PMe_3)_4$ at 210 K followed by annealing to the indicated temperatures and cooling back to 210 K to record the spectra.

406 signal. Features worth noting include: 1) The m/e 406 signal that is associated with the precursor illustrates molecular desorption; 2) The relative intensity of the m/e 76:406 signals at 285 K is 189, which is significantly higher than the relative intensity of 0.11 recorded during residual gas analysis of the precursor alone; 3) The relative intensities for m/e 76, 61, 46, and 31 (P^+) are inconsistent with the electron impact ionization fragmentation pattern for $P(CH_3)_3$ [37]; 4) Only the m/e 16 signal begins to increase at 220 K; and, 5) The relative intensities of the m/e 16:15 signals at 285 K is 0.08, which is different from that associated with CH_4, with an intensity ratio of 1.12 [37].

Figure 4.14 presents the signal intensities on the high temperature tails of the peaks shown in Figure 4.13. The signals have a baseline intensity of zero when a blank surface is ramped to 975 K. M/e 406 returns to the baseline by 300 K. All the remaining signals continue to generate a nonzero response and m/e 15 and 76 decay differently from m/e 31 and 16. These signals (m/e 15, 76, 31 and 16) remain essentially at the levels indicated at 350 K up to at least 475 K (not shown). Control experiments verify the nonzero response is not associated with adsorbates desorbing from the sample mounts.

In a separate experiment, 0.018 L of the precursor was adsorbed on the surface at 210 K and annealed to successively higher temperatures for 1.0 min and cooled back to 210 K to collect the XPS signals in Figures 3.11 and 3.12. The Ru $3d_{5/2}$ and P 2p peak

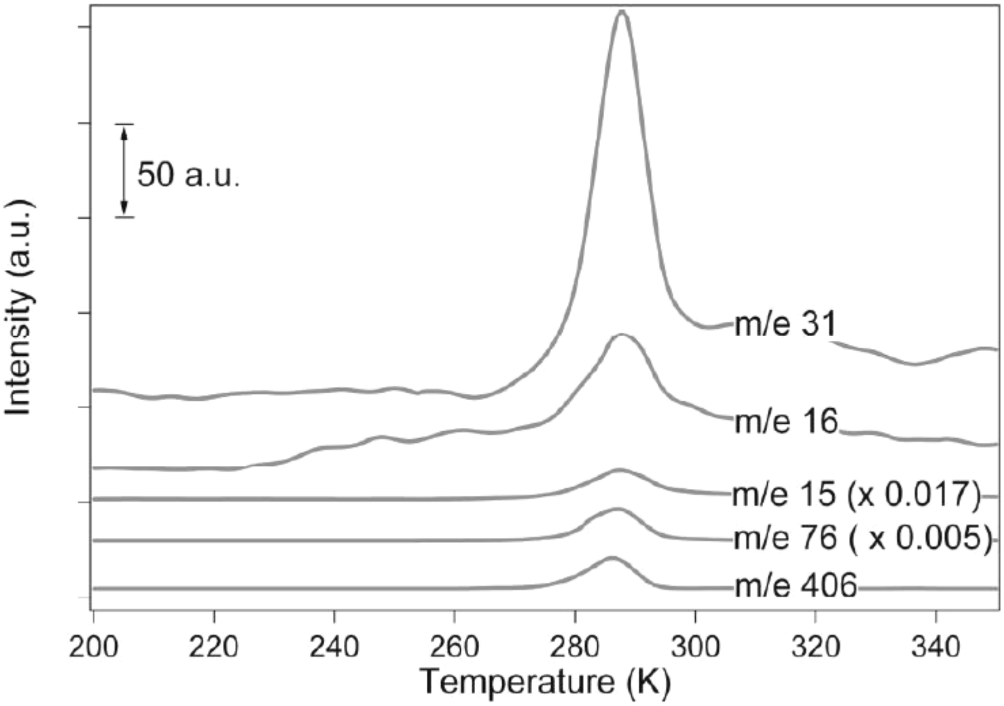

Figure 4.13 TPD spectra of the 0.17 L dose of *cis*-$RuH_2(PMe_3)_4$ at 135 K.

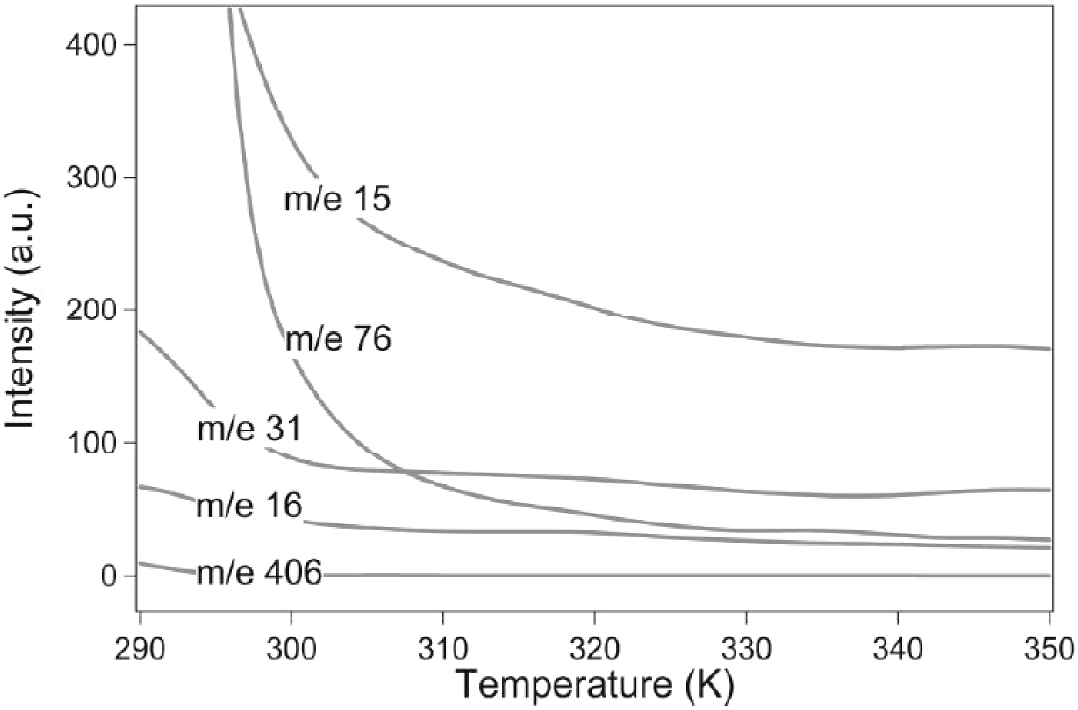

Figure 4.14 Trailing edges of the m/e signals presented in Figure 4.13.

positions are the same as found when condensing the precursor at 135 K. The spectra recorded after annealing to 260 K (not shown) were identical in position and intensity to the spectra recorded after dosing. Annealing to 280 K, the leading edge of the molecular desorption feature in Figure 4.13, results in attenuation of the Ru $3d_{5/2}$ and P 2p signals. The P 2p signals for 280 K, 310 K and 410 K anneals are comparable to the noise level; however, the peak does appear to move to lower binding energy for these anneal temperatures. The Ru $3d_{5/2}$ peaks are constant in area, and decreased relative the 280 K anneal, for annealing to 310 and 410 K. The binding energy for the weak $3d_{5/2}$ feature is estimated to be 279.3 eV.

4.3.3 Modeling Studies

To understand the nature of local packing in Ru-P amorphous structures, we analyzed various atomic configurations obtained from the melt-quenching molecular dynamics simulations as described earlier. For the $Ru_{80}P_{20}$ amorphous alloy, as shown in Figure 4.15, the solute P atoms are more or less evenly distributed while surrounded by Ru atoms. Our DFT-GGA calculation indeed predicts a negative mixing energy in the amorphous system, implying that unlike bonds are favored. The local structure can be characterized by the nearest-neighbor coordination. For the *ab initio* Ru-P configuration, the average first neighbor coordination number (CN=Z) of the P solute is predicted to be

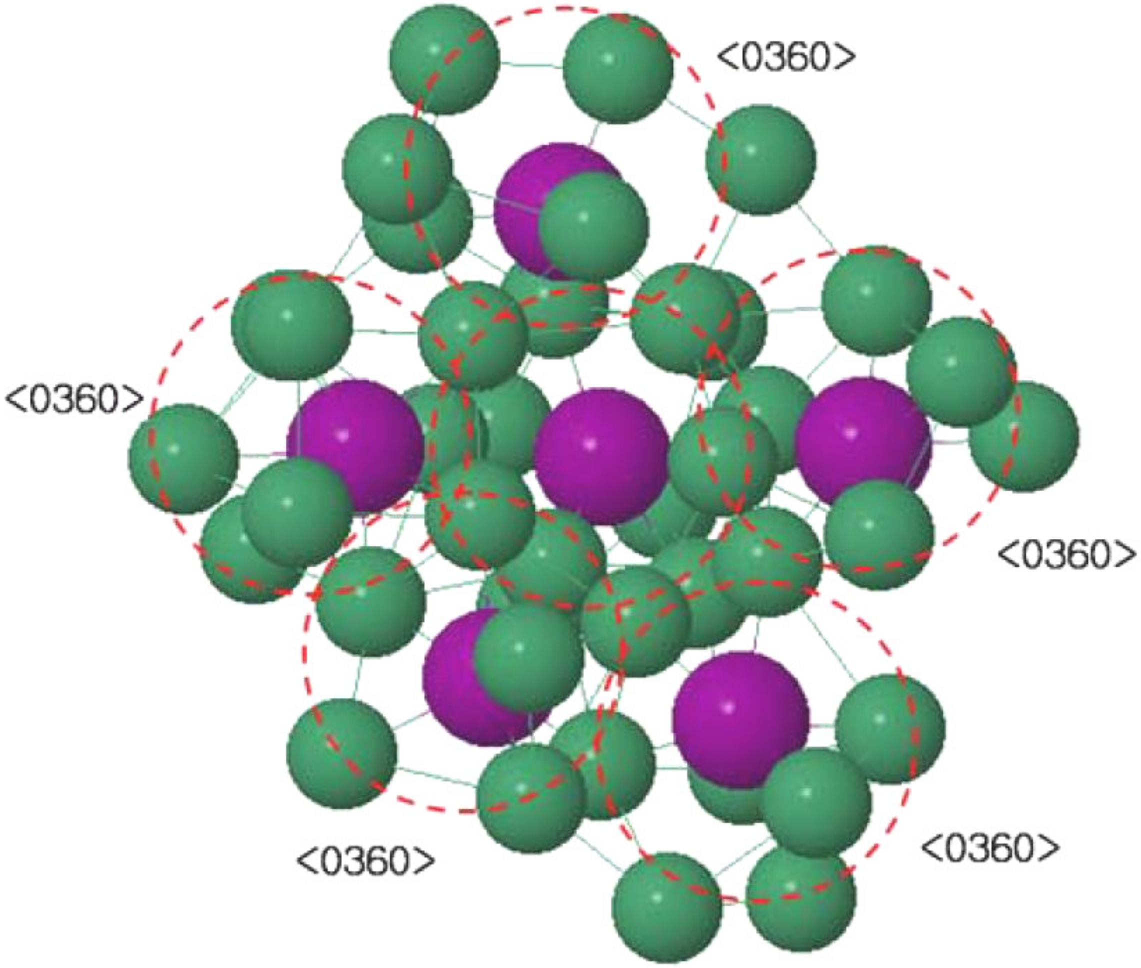

Figure 4.15 Modeling results for the packing of the P-centered quasi-equivalent Ru clusters for a Ru_{80}:P_{20} mixture. Large (purple) and small (green) balls represent P and Ru atoms, respectively.

approximately 9.2, with eight Z9 and two Z10 among ten sampled solutes. Here the CN is defined as the number of Ru neighbors of a central P atom within a cutoff distance of 3 Å (obtained from calculated radial-distribution functions), as the first shell of the solute consists of Ru atoms only.

The type of the coordination polyhedron around a solute atom can further be specified using the Voronoi index $<i_3, i_4, i_5, i_6, \ldots>$, where i_n represents the number of n edged faces of the Voronoi polyhedron [38, 39]. In the $Ru_{80}P_{20}$ glass, the dominant Kasper polyhedra with CN=9 exhibit <0,3,6,0> and <0,5,4,0> types, where the former appears about four times more than the latter. Figure 4.16 shows Z9 and Z10 polyhedra obtained from *ab initio* calculations. In the Ru-P system, seven-edged faces and above were found to hardly occur.

It is now well established that the local order in amorphous binary alloys is strongly controlled by the effective atomic size ratio between solvent and solute atoms, λ [23, 40, 41]. A recent *ab intio* MD study [24] showed that the preferred polyhedra type changes with λ; that is, decreasing the atomic size ratio leads to noticeable changes in the structure of polyhedra from icosahedral with Voronoi index <0,0,12,0> ($\lambda \approx 0.90$), to bicapped square archimedean antiprism (BSAP) with <0,2,8,0> ($\lambda \approx 0.84$), and then to tricapped trigonal prism packing (TTP) with <0,3,6,0> ($\lambda \approx 0.73$). Considering the larger atomic size of Ru than Ni by (about 7 % in pure metal according to Goldschmidt's

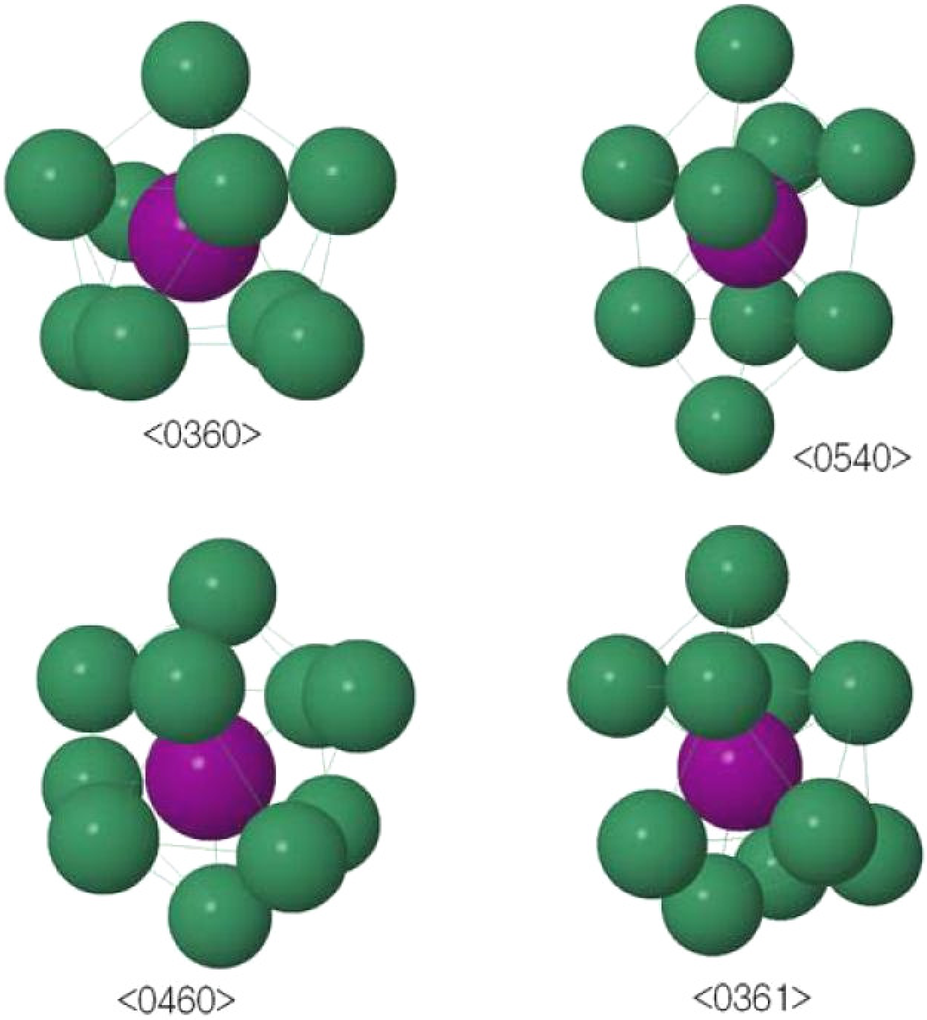

Figure 4.16 Calculated coordination polyhedra in the amorphous $Ru_{80}P_{20}$ alloy from *ab initio* molecular dynamics simulations. Large (purple) and small (green) balls represent P and Ru atoms, respectively.

rules [19]), we can expect that the atomic size ratio λ for the Ru-P alloy is smaller than 0.78 for the Ni-P case. This is consistent with our simulations results showing that the TTP phase is predominant in the $Ru_{80}P_{20}$ structure while the $Ni_{80}P_{20}$ alloy preferably results in the BSAP phase, although the magnitude of λ often differs from that evaluated based on Goldschmidt's atomic radii. As is also shown in Figure 4.15, the formation of 'quasi-equivalent' P-centered Ru clusters arising from topological and chemical short-range order is also likely to lead to the medium range order in the binary alloy, when the clusters are packed in three-dimensional space. In fact, the short-to-medium range order is seen in other metallic glasses, particularly in transition metal-metalloid and transition metal-transition metal systems where the chemical short-range-order is significant [24].

4.4 DISCUSSION

The TEM, SAD and XRD data illustrate an amorphous Ru-P alloy film can be grown from *cis*-$RuH_2(PMe_3)_4$ in a CVD process at 575 K. The amount of phosphorus changed with depth, decreasing to about 15 % within the film bulk. Formation of the amorphous alloy could originate from the uniqueness of the precursor in that it contains both transition metal, Ru, and metalloid, P, or it could result from the physical and chemical effects of mixing alloying components with physical randomization of the lattice due to different atomic sizes and chemical interactions between the metal and metalloid. The modeling studies support the latter.

The surface studies provide insight into the reactions the precursor undergoes during growth. When *cis*-$RuH_2(PMe_3)_4$ is adsorbed above the molecular desorption temperature (285 K), only CH_3 is observed to desorb. Sequential demethylation, with retention of P on the surface is likely occurring. Tao *et al.* followed the reaction of $P(CH_3)_3$ on Ru(0001) and report $P(CH_3)_3$ undergoes stepwise demethylation, with the final step, $P(CH_3) \rightarrow P$, being completed by 500 K [42]. The TPD peak (Figure 4.10b) could be associated with a similar demethylation reaction only now the $P(CH_3)_y$ (y = 1-3) is bonded to a Ru atom and/or the Ta_xO_y surface. The presence of residual carbon on the Ta_xO_y surface might be explained by some of the demethylation reactions occurring on the Ta surface since Tao *et al*. ultimately formed Ru_xP above 600 K.

The precursor likely adsorbed dissociatively on Ta_xO_y at 455 K. Unfortunately the composition could not be determined in this study. Only the demethylation reaction could be detected during TPD.

The low temperature experiments reveal some reactions begin as low as 220 K with the evolution of the m/e 16 signal in TPD. This m/e 16 signal cannot be associated with methane as it lacks a corresponding m/e 15 signal and its identity remains unresolved. The relative intensities of the signals during the main 285 K desorption feature in Figure 4.13 cannot be accounted for by the precursor and $P(CH_3)_3$ alone.

Demethylation contributes to the m/e 15 signal. The m/e 76 signal is associated with $P(CH_3)_3$ and a P-containing species whose identity remains unresolved. Finally the trailing edge signals (Figure 4.14) reveal the species remaining after molecular desorption continue to undergo demethylation and evolve a P-containing species.

The surface studies illustrate that demethylation is quite efficient near the TPD peak temperature of 560 K (Figure 4.10b) and this is approximately the minimum temperature for film growth of 525 K. The surface studies also indicate some of the $P(CH_3)_3$ ligands are desorbing, either intact or after partial decomposion, well below the film growth temperature. Therefore, we propose that not all the $P(CH_3)_3$ ligands remain on the surface during growth. Clearly some remain and are directly incorporated into the film. The desorbing P-containing species can also readsorb since the growth pressure is ~200 mTorr and subsequently incorporate P into the film. This readsorption path could explain why the P content was significantly lower at 525 K than 575 K (Figure 4.3). A readsorption path suggests dual sources in which a phosphorus precursor such as PH_3, $P(CH_3)_3$ or $P(C_2H_5)_3$ are used along with more conventional Ru precursors could also lead to amorphous Ru-P alloys.

Our *ab initio* MD simulations show the formation of 'quasi-equivalent' P-centered Ru clusters with both topological and chemical short-range order in the $Ru_{80}P_{20}$ amorphous alloy. Subsequently this leads to the medium range order as the clusters are packed in three-dimensional space. The atomic structure obtained from melt-quenching simulations might differ from that in the experimental samples, whose structure could also be determined by CVD kinetics. Nonetheless, our simulation results clearly demonstrate the existence of amorphous Ru-P alloys with moderate P content.

Films grown at 575 K do feature very small crystalline regions, mostly adjacent to the SiO_2 interface. Considering the longer duration at an elevated temperature during deposition and the lower P concentration near the substrate than the surface, it is plausible that Ru atoms organized into small crystallites during the film deposition. These crystallites appear to serve as nucleation centers for the larger crystallites found after annealing to 775 K. Annealing the Ru-P alloy to 775 K and higher demonstrates the films are metastable. Metastability has been reported for other amorphous alloy films [14,16-18]. Modeling and experimental studies are required to establish the extent to which thermodynamically stable compound formation, such as Ru2P [43], or a more stable alloy composition drive the segregation of the as-grown composition to produce regions that are crystalline and regions that remain amorphous.

4.5 SUMMARY

This study reports the CVD growth of a metastable Ru-P alloy at 575 K. Films as thin as 30 nm contain zero-valent Ru and P. The films remain amorphous upon heating for 3 hr at 635 K, and begin to crystallize upon annealing at 775 K for 30 min in vacuum. The phosphorus content is related to the growth temperature, with more P found at higher temperatures, and the amount of alklyphosphorus in the chamber background. Separate surface studies suggest the trimethylphosphine ligands undergo demethylation and desorb at the growth conditions and readsorb, and subsequently incorporate the P into the Ru film. Our *ab initio* molecular dynamics study shows that Ru-P alloys with moderate P content can result in glassy structure exhibiting the topological and strong chemical short-range order. In the $Ru_{80}P_{20}$ structure, the P-centered polyhedra prefer the tri-capped trigonal prism packing (TTP) phase with Veronoi index <0,3,6,0>. In addition, the Ru-P system shows the medium-range order arising from packing the "quasi-equivalent" P-centered Ru clusters in three-dimensional space. The structural model based on melt-quenching simulations might differ from that in experimental samples, which could also be determined by CVD kinetics. Nonetheless our simulation results are sufficient to provide invaluable and unique insight into the nature of local packing in Ru-P amorphous structures.

4.6 REFERENCES

[1] A. Kaloyeros, X. Chen, K. Kumar, S. Seo, G. Peterson, H. Frisch, B. Arkles, and J. Sullivan, *J. Electrochem. Soc.* **146**, 170 (1999).

[2] S. Rossnagel and H. Kim, Proceedings of the IEEE 2001 International Interconnect Technology conference (IEEE, Piscataway, PA 2001) p.3

[3] H. Kim, C. Cabral, C. Lavoie, and S. M. Rossnagel, *J. Vac. Sci. Technol. B* **20**, 1321 (2002).

[4] S. Kim, S. Oh, H. Kim, D. Kang, K. Kim, W. Li, S. Haukka, and M. Tuominen, *J. Electrochem. Soc.* **151**, C272 (2004).

[5] I. Goswami and R. Laxman, *Semiconductor International* **27**, 49 (2004).

[6] Q. Wang, J. G. Ekerdt, D. Gay, Y. Sun, and J. M. White, *Appl. Phys. Lett.* **84**, 1380 (2004).

[7] M. Green, M. Gross, L. Papa, K. Schnoes, and D. Brasen, *J. Electrochem. Soc.* **132**, 2677 (1985).

[8] Y. Matsui, M. Hiratani, T. Nabatame, Y. Shimamoto, and S. Kimura, *Electrochem. Solid State Lett.* **5**, C18 (2002).

[9] M. Lashdaf, T. Hatanpää, A. O. I. Krause, J. Lahtinen, M. Lindblad, and M. Tiitta, *Appl. Catal. A* **241**, 51 (2003).

[10] R. Chan, T. N. Arunagiri, Y. Zhang, O. Chyan, R. M. Wallace, M. J. Kim, and T. Q. Hurd, Electrochem. *Solid-State Lett.* **7**, G154 (2004).

[11] J. Tan, X. Qu, Q. Xie, Y. Zhou, and G. Ru, *Thin Solid Films* **504**, 231 (2006).

[12] H. L. Skriver, and N. M. Rosengaard, *Phys. Rev. B* **46**, 7157 (1992).

[13] J. Lin, and C. Lee, *J. Electrochem. Soc.* **146**, 3466 (1999).

[14] C-S., Jun, and T. P. Fehlner, *Chem. Mater.* **4**, 440 (1992).

[15] H. Kim, C. Detavenier, O. van der Straten, S. M. Rossnagel, A. J. Kellock, and D-G. Park, *J. Appl. Phys.* **98**, 014308 (2005).

[16] C. M. Eichfeld, M. A. Horsey, S. E. Mohney, A. V. Adedeji, and J. R. Williams, *Thin Solid Films* **485**, 207 (2005).

[17] H. Li, H. Li, W. Dai, W. Wang, Z. Fang, and J. Deng, *Appl. Sur. Sci.* **152**, 25 (1999).

[18] A. Kohn, M. Eizenberg, and Y. Sacham-Diamand, *J. Appl. Phys.* **94**, 3810 (2003).

[19] O. N. Senkov, and D. B. Miracle, *Mater. Res. Bull.* 36, 2183 (2001).

[20] R. Busch, *J. Mater.* **52**, 39 (2000).

[21] J. Basu, and S. Ranganathan, *Sandhana* **28**, Parts 3 & 4, 783 (2003).

[22] L. Xia, S. S. Fang, Q, Wang, Y. D. Dong, and C. T. Liu, *Appl. Phys. Lett.* **88**, 171905 (2006).

[23] H.-J. Lee, T. Cagin, W. L. Johnson, and W. A. Goddard III, *J. Chem. Phys.* **119**, 9858 (2003).

[24] H. W. Sheng, W. K. Luo, F. M. Alamgir, J. M. Bai, and E. Ma, *Nature* **439**, 419

(2006).

[25] H. Schmidbauer, and G. Blaschke, *Z. Naturforsh.* **35b**, 584 (1980).

[26] W. Kohlmann, and H. Werner, *Z. Naturforsch.* **48b**, 1499 (1993).

[27] J. P. Perdew, J. A. Chevary, S. H. Vosko, K. A. Jackson, M. R. Pederson, D. J. Singh, and C. Fiolhais, *Phys. Rev. B* **46**, 6671 (1992).

[28] G.. Kresse, and J. Hafner, *Phys. Rev. B* **47**, 553 (1993).

[29] G.. Kresse, and J. Furthmüller, *Comput. Mater. Sci.* **6**, 15 (1996).

[30] G.. Kresse, and J. Furthmüller, *Phys. Rev. B* **54**, 11169 (1996).

[31] Y. Lai, Y. Chen, Y. Chi, C. Liu, A. J. Carty, S. Peng, and G. Lee, *J. Mater. Chem.* **13**, 1999 (2003).

[32] H. Li, W. Dai, W. Wang, Z. Fang, and J. Deng, *Appl. Surf. Sci.* **152**, 25 (1999).

[33] Powder Diffraction File, Joint Committee on Powder Diffraction Standards, ASTM, Philadelphia, PA, 1967, Card 06-0663.

[34] P. Giauque and M. Nicolet, *J. Appl. Phys.* **93**, 4576 (2003).

[35] S. Mader, *J. Vac. Sci. Technol.* **2**, 35 (1964).

[36] C. D. Wagner, L. E. Davis, M. V. Zeller, J. A. Taylor, R. H. Raymond, and L. H. Gale, *Surf. Interface Anal.* **3**, 211 (1981).

[37] *Mass Spectra* in NIST Chemistry Webbook, NIST Standard Database Number 69, Eds. P. J. Linstrom and W. G. Mallard, June 2005, NIST, Gaithersburg, MD 20899 (http://webbook.nist.gov).

[38] J. L. Pinney, *Proc. R. Soc. A* **319**, 479 (1970).

[39] J. L. Pinney, *Nature* **266**, 309 (1977).

[40] Y. Qi, T. Cagin, Y. Kimura, and W. A. Goddard III, *Phys. Rev. B* 59, 3527 (1999).

[41] D. Duan, D. Xu, Q. Zhang, Q. Zhang, T. Cagin, W. L. Johnson, and W. A. Goddard III, *Phys. Rev. B* **71**, 224208 (2005).

[42] H.-S. Tao, U. Diebold, N. D. Shinn, and T. E. Madey, *Surface Science* **375**, 257 (1997).

[43] V. B. Chernogorenko, V. G. Ivanchenko, and L. Ya. Kulik, in *Binary Phase Diagrams*, edited by. T. B. Massalski, H. Okamoto, P. R. Subramanian, and L. Kacprzak, (ASM International, Materials, Park, OH 1990) p 2979.

Chapter 5

Chemical Vapor Deposition of Amorphous Ruthenium - Phosphorus Alloy Films with $Ru_3(CO)_{12}$ and $P(CH_3)_3$ or $P(C_6H_5)_3$

5.1 INTRODUCTION

With feature scaling in microelectronic devices, new materials have been adopted, such as Cu for the interconnect wiring. Copper readily diffuses into silicon and through dielectrics and a diffusion barrier is required to prevent this. Copper is also prone to electromigration and seed layer/liner materials are required that can facilitate both the Cu deposition process and eliminate Cu electromigration. The barrier material and the seed layer/liner material combined thickness is projected to be <3.3 nm for the 45-nm generation [1] and a single material that could function as both would be ideal.

Ruthenium shows potential because of its low resistivity of ~7 μΩ cm, chemical stability, low solubility with Cu [2], and ability to form a strong first layer with Cu [3,4]. However, Ru like most metals forms polycrystalline thin films with a columnar character that cannot be expected to function as the Cu diffusion barrier as recently demonstrated

[5,6]. Alloying Ru to generate an amorphous film is one approach to enable it to function as both the seed/liner and the diffusion barrier.

We have recently reported the chemical vapor deposition (CVD) growth of amorphous Ru–P alloys containing ~15% P (*n.b.*, compositions on an atom basis) in the bulk using a single source precursor, *cis*-ruthenium(II)dihydrotetrakis-(trimethylphosphine), *cis*-$RuH_2(P(CH_3)_3)_4$, at 575 K [7,8]. These films were metastable and remained amorphous upon annealing to 635 K for 3 h, and displayed small crystallites in an amorphous matrix upon annealing to 775 K for 1 h [8]. *Ab initio* molecular dynamics calculations [8] revealed that Ru–P alloys with 20% P can result in a glassy structure exhibiting the topological and strong chemical short-range order previously reported for bulk metallic glasses [9-14]. Surface studies revealed the trimethylphosphine ligands of *cis*-$RuH_2(P(CH_3)_3)_4$ both desorbed intact and underwent a stepwise demethylation to generate the P for Ru–P alloy formation [8].

Herein we report the use of dual sources to explore both how general the Ru–P alloy formation is in CVD and how the P content influences microstructure and resistivity, and we report on gradient corrected density functional calculations that explore the stability and bonding properties of the amorphous phase. Triruthenium dodecarbonyl, $Ru_3(CO)_{12}$, does not require a reactive gas, like O_2 or H_2 [4,15], and trimethylphoshine, $P(CH_3)_3$ is used because surface studies have shown it readily demethylates on Ru to give

P by 500 K [16].

5.2 EXPERIMENTAL DETAILS

Film growth was carried out in a deposition and analysis facility consisting of a vacuum sample transfer system, load lock, X-ray photoelectron spectroscopy (XPS) system (Physical Electronics 3057), CVD chamber, and a physical vapor deposition (PVD) chamber [8]. The stainless steel CVD chamber is a cold-wall vessel (base pressure 6.7×10^{-6} Pa) and the SiO_2/Si(100) substrates were heated radiatively from below. Thermally grown SiO_2 (100 nm)/Si(100) 200 mm wafers were supplied by Sematech. The wafers were cut into 20 × 20 mm pieces and heated to the growth temperature under vacuum. $Ru_3(CO)_{12}$ (Strem Chemical; 99%) was sublimed at 355 K and delivered to the CVD chamber using 2.5 – 5.0 standard cm^3 per min (sccm) of flowing Ar or H_2 through a heated gas line and shower head. $P(C_6H_5)_3$ (Strem Chemical, 99%) was sublimed at 335 K and delivered using 5 – 10 sccm of flowing Ar through separately heated lines. $P(CH_3)_3$ (Strem Chemical, 99%) was dosed directly into the reaction chamber; the flow was controlled using a leak valve. Crystallinity is established using grazing angle (1º) X-ray diffraction (XRD) (Bruker-Nonius D8). Resistivity was established by measuring the sheet resistance of thin films with a four point probe and the thickness was determined from cross section scanning electron microscopy (SEM) (LEO 1530). Low energy ion scattering spectroscopy (LEISS) was carried out *in situ* using 1 kV He^+. The samples were sputter cleaned with 2 kV Ar^+ before both XPS and LEISS.

Our first principles calculations were performed within the generalized gradient approximation (GGA-PW91 [17]) to density functional theory (DFT) using the well established Vienna *ab initio* Simulation Package [18,19]. A planewave basis set for valence electron states and Vanderbilt ultrasoft pseudopotentials for core-electron interactions were employed. A plane-wave cutoff energy of 300 eV was used and the Brillouin zone integration was performed using one k-point (at Gamma). Model amorphous Ru(P) alloy structures considered herein were constructed using *ab initio* molecular dynamics within a Born-Oppenheimer framework [7,8].

5.3 RESULTS AND DISCUSSION

Figure 5.1 presents Ru 3d and P 2p XPS peaks for the Ru(P) film grown from $Ru_3(CO)_{12}$ and $P(CH_3)_3$ with H_2 at 575 K. Ru $3d_{5/2}$ and P $2p_{3/2}$ peaks locate at 280.1 eV and 129.8 eV, respectively, which are consistent with the peak positions in the Ru(P) films grown from $RuH_2(PMe_3)_4$ [8]. From the binding energies, Ru and P atoms in Ru(P) films grown from the single source precursor and the dual sources are in the identical chemical states. According to our previous study on the microstructure of amorphous Ru(P), each P atom is surrounded by on average 9.2 Ru atoms, therefore the

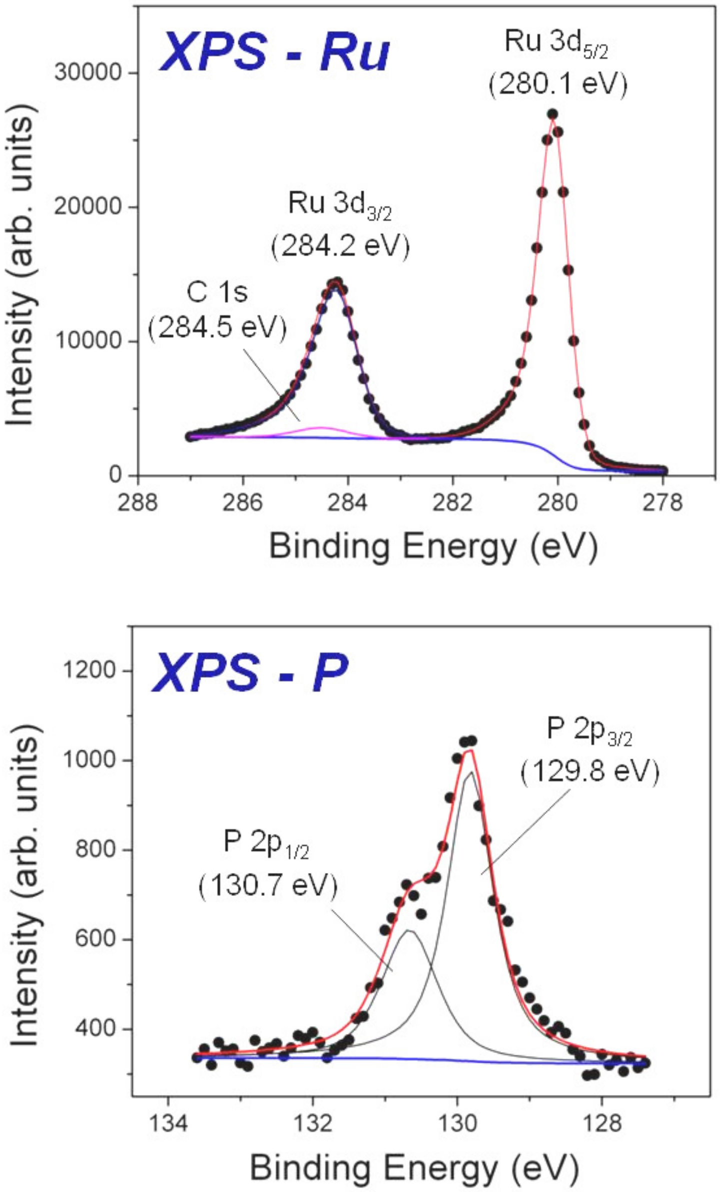

Figure 5.1 XPS Ru 3d and P 2p peaks of amorphous Ru(P) film grown at 575 K from $Ru_3(CO)_{12}$ and $P(CH_3)_3$ with H_2.

binding energy shift by charge transfer will be more pronounced in the P 2p peak than the Ru 3d peak. P $2p_{3/2}$ peaks in amorphous Ni(P) alloys are reported to have 0.4 – 0.5 eV of chemical shift by partial electron donation from Ni to P [20-22]. Strong hybridization between P 3p and Ni 3d bands are observed in the density of state (DOS) study with Ni(P) alloys, and a P atom accepts 0.3 – 0.4 electron form adjacent Ni atoms [23]. Our study on the DOS of Ru(P) also shows hybridization between P 3p and Ru 4d orbitals (Figure 5.4). However, the binding energy of P $2p_{3/2}$ peak in Ru(P) is slightly lower than zero-valent state by ~ 0.08 eV, and it is likely an XPS analysis error rather than chemical shift. Therefore, charge transfer between P and Ru atoms in Ru(P) is minimal, and both Ru and P are in nearly zero-valent states.

The effect of growth conditions on the composition and materials properties of the films is summarized in Table 5.1. P can be incorporated into the Ru films by co-dosing either $P(CH_3)_3$ or $P(C_6H_5)_3$ with $Ru_3(CO)_{12}$ during film growth. Higher $P(CH_3)_3$ or $P(C_6H_5)_3$ dosing results in more P and C incorporated in the films, and also lower growth rate. The exact C concentration is difficult to measure because the C 1s and Ru $3d_{3/2}$ XPS peaks at 285 eV overlap and there is no singular unique C peak. This can be overcome by fitting the Ru $3d_{5/2}$ peak and $3d_{3/2}$ peaks, assuming pure Ru has a $3d_{5/2}$ to $3d_{3/2}$ ratio of 1.5 based on the relative degeneracy of the 3d doublet peaks. Measurement and fitting conditions are carefully optimized using a 99.95% PVD Ru target to minimize possible fitting errors arising from the C sensitivity factor which is

Table 5.1 Effect of phosphorus and carbon content on the film microstructure and resistivity.

Sample	Phosphorus source	Delivery gas	Growth Rate (Å/min)	P (at.%)	C (at.%)	Resistivity (μΩ•cm)	Microstructure
1	TPP⁽¹⁾	Ar	6.5	6.3	31.9	12,624	Crystalline
2	TPP	Ar	5.5	11.4	47.9	1,099,506	Amorphous
3	TMP⁽²⁾	Ar	10.2	2.4	-	263	Crystalline
4	TMP	Ar	1.8	10.2	35.6	864	Amorphous
5	TMP	H_2	5.7	5.7	-	59	Crystalline
6	TMP	H_2	2.5	11.3	10.5	209	Amorphous
7	TMP	H_2	< 2.5	14.7	22.3	367	Amorphous

(1) Triphenylphosphine
(2) Trimethylphosphine

14.4 times higher than that of Ru [24]. The films grown with $P(CH_3)_3$ have a lower C content compared to films grown with the more C-rich $P(C_6H_5)_3$. H_2 was used as the $Ru_3(CO)_{12}$ carrier gas to help drive any ligand dehydrogenation reaction in the reverse direction. Amorphous Ru(P) film having lowest C impurity, ~ 10%, was obtained when $P(CH_3)_3$ and H_2 are used. C is not an efficient element for amorphizing Ru; the sample 1 in Table 5.1 contains 31.9% C and still remains crystalline. This is possibly because of the small atomic size of C or weak chemical interaction with Ru. While C has little impact on microstructure, it shows considerable impact on film resistivity as shown in Table 5.1.

The microstructure of Ru(P) alloy films are closely related to P concentration in the films. The films having more than ~ 10% P feature amorphous microstructure in Table 5.1. The minimum P content in amorphous Ru(P) films is 13% on a C free basis (sample 6), which is similar with the amorphous Ru(P) films grown with *cis*-$RuH_2(P(CH_3)_3)_4$ that contained 15% P [8]. Figure 5.2 (a) presents calculated total energy differences between crystalline and amorphous Ru(P) alloys with varying stoichiometric ratios. The result demonstrates that above 20% P the amorphous phase is energetically more favorable than the crystalline phase. Here, the total energy variation of the crystalline alloys was calculated by replacing Ru with P starting with a pure hexagonal close packed Ru phase, which is modeled using a 72-atom supercell with a lattice constant of 2.70 Å. For each crystalline or amorphous alloy considered, the

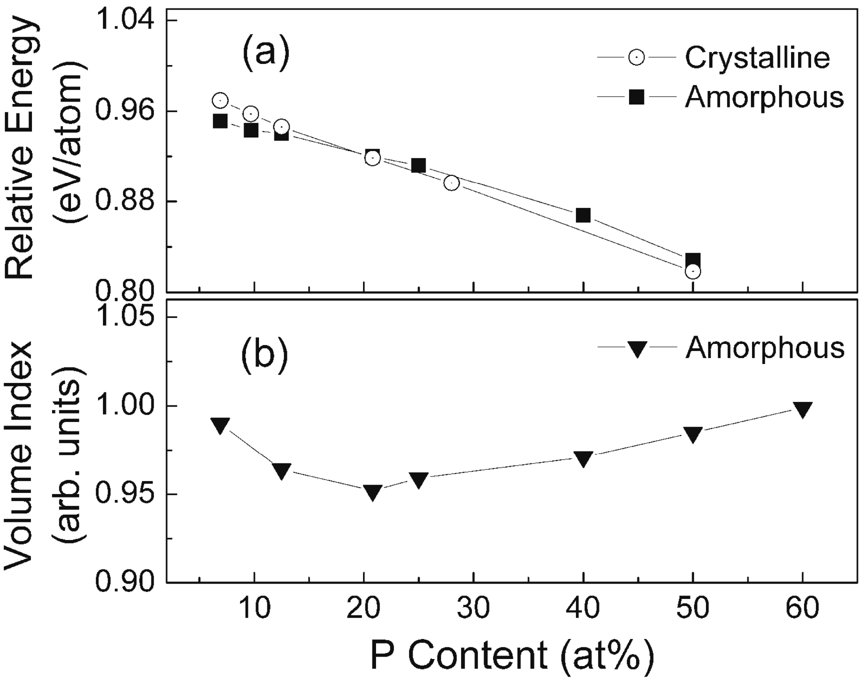

Figure 5.2 Variation in (a) the total energy difference between the crystalline and amorphous phases and (b) the optimized volume of Ru(P) alloys as a function of the P content.

volume of the 72-atom supercell was optimized by determining the minimum total energy with varying supercell volumes. As shown in Figure 5.2 (b), the alloy volume becomes the minimum at 20% P, yielding the highest packing density. Lower P concentration observed in the grown Ru(P) films featuring amorphous character can be attributed to the local effect of non-uniform P distribution or the effect of C impurity, which is not considered in the calculation.

Figure 5.3 shows a variation in the mixing energy of amorphous Ru(P) alloys as a function of the stoichiometric ratio, with respect to amorphous Ru and P. The negative mixing energy demonstrates that the alloy state is thermodynamically favored in the amorphous phase. Our density functional calculations also predict that the Ru(P) alloy forms the most stable structure when the P content is around 40-50%. The sizable energy gain of the $Ru_{60}P_{40}$ structure, relative to the $Ru_{80}P_{20}$ structure, suggests that the Ru(P) alloys with a low P content (~ 20%) may undergo P segregation during high temperature thermal treatment.

To gain understanding of the Ru(P) bonding properties, as shown in Figure 5.4 we analyzed the density of states (DOS) of the $Ru_{80}P_{20}$ alloy (inset), including the total DOS [(a)] and the partial DOS of Ru 4d [(b)] and P 3p [(c)]. The Fermi level is used as the reference energy state. The calculated total DOS shows no gap at the Fermi level, indicating that the Ru(P) alloy is metallic. In Figure 5.4 (a), peaks below -10 eV are

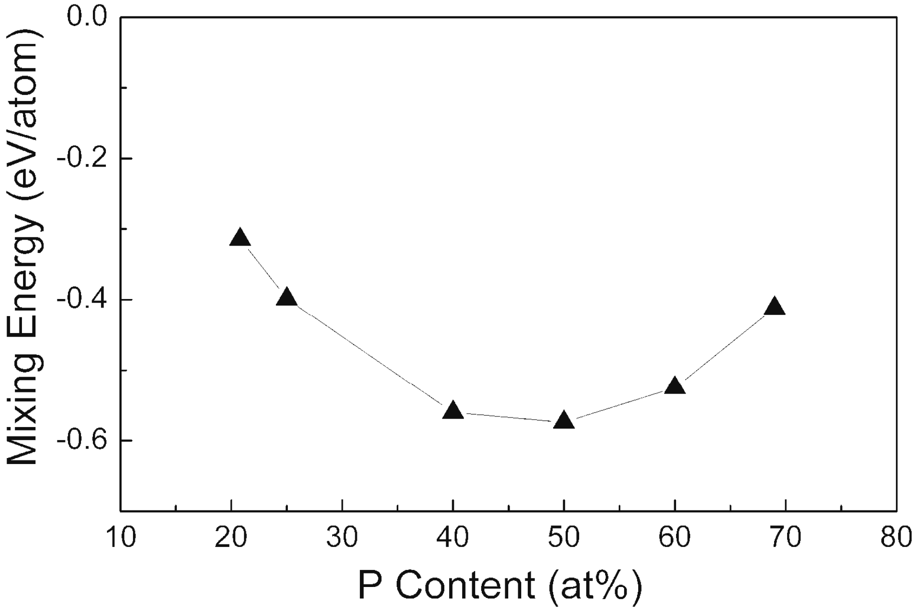

Figure 5.3 Variation of the mixing energy of amorphous Ru(P) alloys in terms of the P content, with respective to amorphous Ru and P structures.

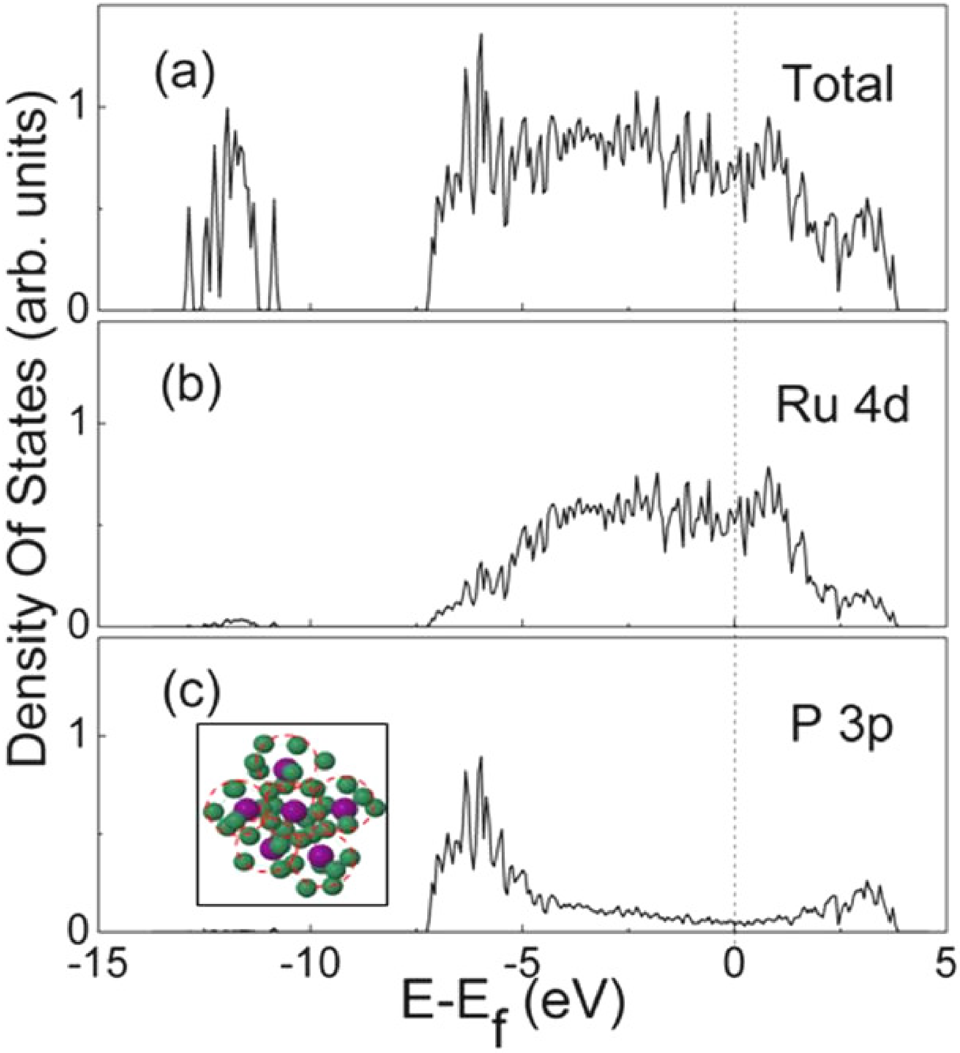

Figure 5.4 Calculated densities of states (DOS) for the $Ru_{80}P_{20}$ alloy, as shown in inset (c): (a) total, (b) Ru 4d, and (c) P 3p. The Fermi level is indicated as a dotted line.

assigned to the P 3s state, and the peaks of occupied state densities above -10 eV mainly originate from the P 3p and Ru 4d orbitals. In the energy range between -4 and -7, we can see a high degree of hybridization of Ru 3d with P 3p states. It is apparent that the p-d hybridization mainly contributes to stabilizing the Ru(P) alloy structure.

The seed layer for Cu plating needs to have as low a resistivity as possible; bulk Ru has a resistivity of ~7 μΩ cm, which makes it a viable seed layer material. The results in Table 5.1 illustrate that resistivity is most sensitive to the C content of the films, as reflected in the Ru 3d peak ratios, increasing with C content. Microstructure is also a factor since films of comparable C content (Samples 3 and 7) illustrate that crystalline films will have a lower resisitivity.

Previous studies have revealed that CVD Ru growth on SiO_2 from $Ru_3(CO)_{12}$ resulted in polycrystalline films having a columnar structure, due to the high surface energy of Ru (3.05 J/m^2 for Ru(0001)). The study also showed that a film greater than 20 nm was needed to fully cover the SiO_2 surface [15]. Herein we show that amorphous Ru(P) films as thin as 7.1 nm are continuous (Figure 5.5). This is established using XPS to follow the intensity changes in the substrate peaks as the Ru(P) films becomes thinned with Ar^+ sputtering and LEISS to monitor the composition of the top most layer. The inelastic mean free path of Si 2p electrons through Ru is used to compute film thickness assuming a uniform and flat film. The lower minimum thickness for continuous

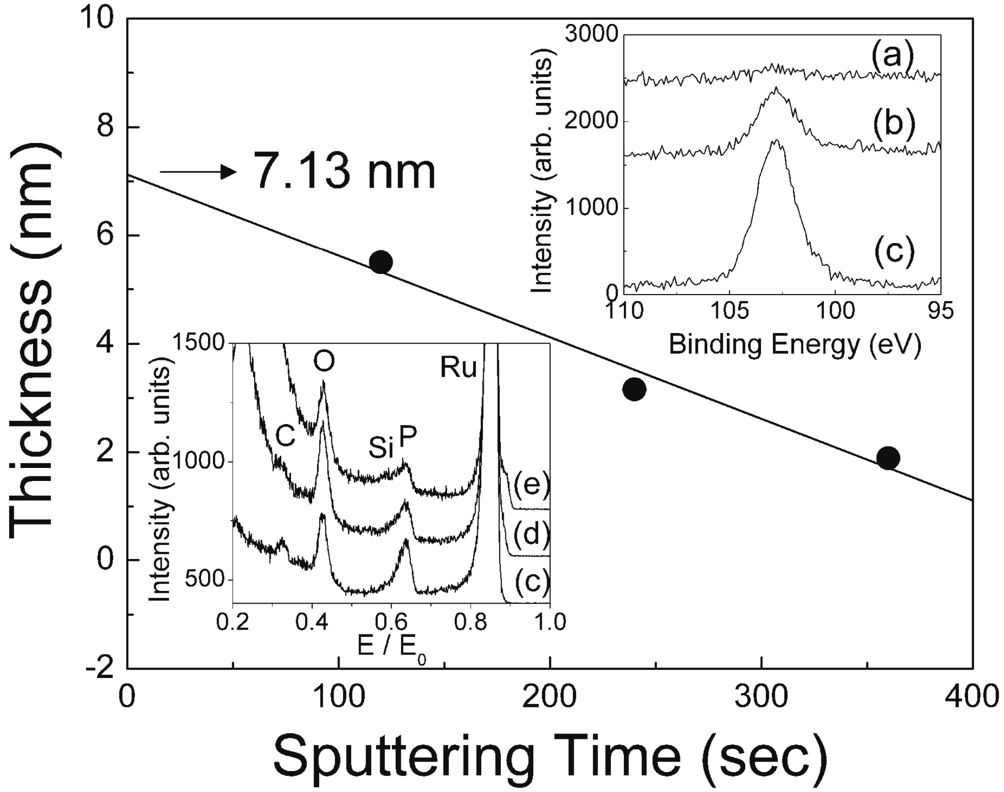

Figure 5.5 Thickness of a Ru(P) film deposited on SiO_2 that was determined by sputtering the film with Ar^+ and monitoring the escape Si 2p XPS peak intensity. The inset (top right) shows the Si 2p peak intensity after sputtering for (a) 120 s, (b) 240 s, and (c) 360 s with 2 kV Ar^+. The points were determined using an electron inelastic mean free path of 1.671 nm. The inset (bottom left) shows the LEISS data after sputtering for (c) 360 s, (d) 480 s, and (e) 600 s with 2 kV Ar^+. The Si feature becomes discernable after 600 s of sputtering, indicating the underlying SiO_2 substrate has been reached.

amorphous Ru(P) films compared to polycrystalline Ru films can be attributed to the lower nucleation energy of the amorphous phase and better wettability because incorporation of P and C lower the surface energy [25].

Strong copper adhesion to the liner material (*i.e.*, diffusion barrier and seed layer(s)) is one metric that is necessary to minimize copper electromigration in copper interconnect applications [26]. Figure 5.6 presents the LEISS results for two different CVD films that contain different amounts of P and C. The conditions used to grow the film with *cis*-$RuH_2(P(CH_3)_3)_4$ are found elsewhere [7, 8]. The Cu is deposited using PVD and the total time is 5 s, making it difficult to realize thinner films. Cu film thickness is established using attenuation of the Ru $3d_{5/2}$ XPS peak and assumes the Cu film is uniform. The LIESS data (Figure 5.6) demonstrate that films as thin as 0.4-0.6 nm completely wet the Ru(P) films, and that the presence of P up to ~ 30% at the surface does not lead to Cu dewetting and forming islands.

5.4 SUMMARY

Chemical vapor deposition growth of amorphous ruthenium-phosphorus films on SiO_2 is demonstrated at 575 K provided the P content is greater than 15%. First-principles density-functional calculations are presented that reveal the interaction of Ru with P, and that predict the amorphous structure should be most stable above 20 at.% P.

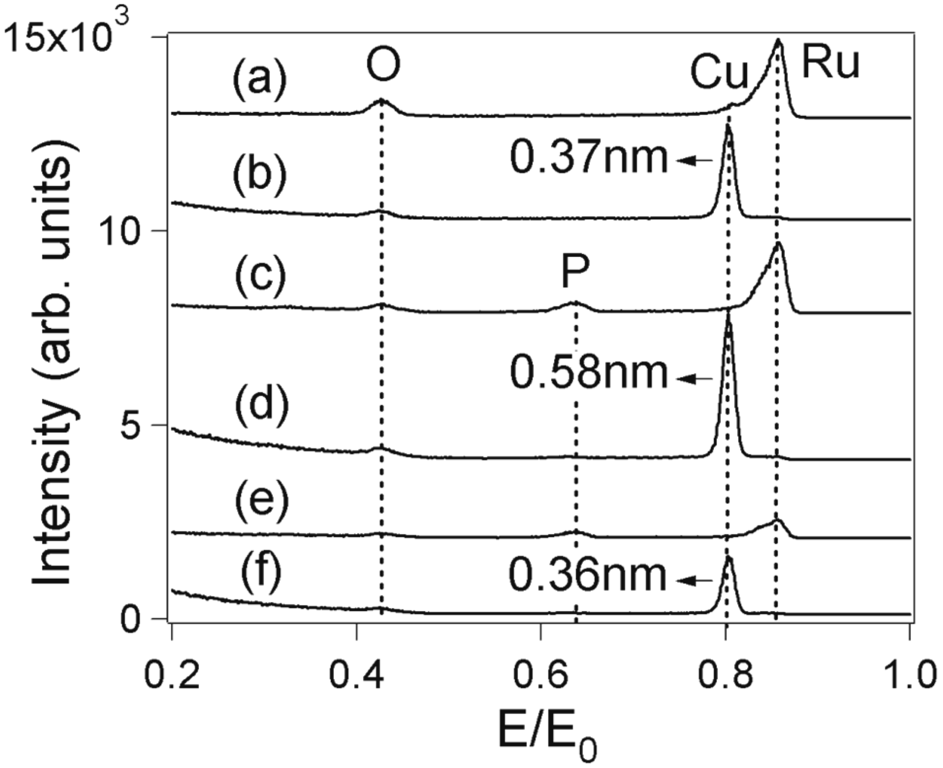

Figure 5.6 LEISS results showing the wettability of Cu on Ru and Ru(P) films. (a) PVD Ru film, (b) 0.37 nm PVD Cu on the PVD Ru film, (c) CVD Ru(P) film grown from $Ru_3(CO)_{12}$ and $P(CH_3)_3$ containing 14.9% P and with a Ru $3d_{5/2}$ to $3d_{3/2}$ ratio of 1.39, (d) 0.58 nm PVD Cu on the CVD Ru(P) film grown from $Ru_3(CO)_{12}$ and $P(CH_3)_3$, (e) CVD Ru(P) film grown with *cis*-$RuH_2(P(CH_3)_3)_4$ containing 28.1% P and with a Ru $3d_{5/2}$ to $3d_{3/2}$ ratio of 1.38, and (f) 0.36 nm CVD Cu on the CVD Ru(P) film grown with *cis*-$RuH_2(P(CH_3)_3)_4$.

5.5 REFERENCES

[1] International Technology Roadmap for Semiconductors, 2006 Update ed, (2007). Available at <http://public/itrs.net>.

[2] I. Goswami and R. Laxman, *Semiconductor International* **27**, 49 (2004).

[3] J. E. Houston, P. J. Berlowitz, J. M. White, and D. W. Goodman, *J. Vac. Sci. Technol. A* **6**, 887 (1988).

[4] Q. Wang, J. G. Ekerdt, D. Gay, Y. Sun, and J. M. White, *Appl. Phys. Lett*. **84**, 1380 (2004).

[5] R. Chan, T. N. Arunagiri, Y. Zhang, O. Chyan, R. M. Wallace, M. J. Kim, and T. Q. Hurd, *Electrochem. Solid-State Lett.* **7**, G154 (2004).

[6] J. Tan, X. Qu, Q. Xie, Y. Zhou, and G. Ru, *Thin Solid Films* **504**, 231 (2006).

[7] J. Shin, A. Waheed, K. Agapiou, W. A. Winkenwerder, H-W. Kim, R. A. Jones, G. S. Hwang, and J. G. Ekerdt, *J. Amer. Chem. Soc*. **128**, 16510 (2006).

[8] J. Shin, A. Waheed, W. A. Winkenwerder, H-W. Kim, R. A. Jones, G. S. Hwang, and J. G. Ekerdt, *Thin Solid Films*, **515**, 5298 (2007).

[9] O. N. Senkov and D. B. Miracle, *Mater. Res. Bull.* **36**, 2183 (2001).

[10] R. Busch, *J. Mater.* **52**, 39 (2000).

[11] J. Basu and S. Ranganathan, *Sadhana* **28, Parts 3 & 4**, 783 (2003).

[12] L. Xia, S. S. Fang, Q, Wang, Y. D. Dong, and C. T. Liu, *Appl. Phys. Lett.* **88**, 171905 (2006).

[13] H.-J. Lee, T. Cagin, W. L. Johnson, and W. A. Goddard III, *J. Chem. Phys.* **119**, 9858 (2003).

[14] H. W. Sheng, W. K. Luo, F. M. Alamgir, J. M. Bai, and E. Ma, *Nature* **439**, 419 (2006).

[15] J. Shin, D. Gay, Y-M. Sun, J. M. White, and J. G. Ekerdt, in: D. G. Seiler, A. C. Diebold, R. McDonald, C. R. Ayre, R. P. Khosla, S. Zollner, and E. M. Secula (Eds.), AIP Conferences Proceedings Vol 788, Melville, NY, 2005, p. 482.

[16] H.-S. Tao, U. Diebold, N. D. Shinn, and T. E. Madey, *Surf. Sci.* **375**, 257 (1997).

[17] J. P. Perdew, J. A. Chevary, S. H. Vosko, K. A. Jackson, M. R. Pederson, D. J. Singh, and C. Fiolhais, *Phys. Rev. B* **46**, 6671 (1992).

[18] G. Kresse and J. Hafner, *Phys. Rev. B* **47**, 553 (1993).

[19] G. Kresse and J. Furthmüller, *Phys. Rev. B* **54**, 11169 (1996).

[20] J. Kojnok, A. Szasz, W. Krasser, G. Mark, V. S. Stepanjuk, and A. A. Kastsnelson, *J. Phys.: Condens. Matter* **4**, 2487 (1992).

[21] E. Belin, A. Traverse, A.Szasz, and F. Hachizaud, *J. Phys. F: Met. Phys.* **17**, 1913

(1987)

[22] E. Cartier, Y. Baer, M. Liard, and H. J. Guntherhodt, *J. Phys. F: Met. Phys.* **10**, L21 (1980).

[23] R. B. Diegle, N. R. Sorensen, C. R. Clayton, M. A. Helfand, and Y. C. Yu, *J. Electrochem. Soc.* **135**, 1085 (1988).

[24] D. Briggs and M. P. Seah, Practical Surface Analysis. Vol 1. Auger and X-ray Photoelectron Spectroscopy, John Wiley and Sons, Chichester, UK, 1990, p. 635.

[25] K. N. Tu, J. W. Mayer, L. C. Feldman, Electronic Thin Film Science, Mcmillian, New York, 1992, p. 246.

[26] H. Kim, Y. Naito, T. Koseki, T. Ohba, T. Ohta, Y. Kojima, H. Sato, Y. Shimogaki, *Jpn. J. Appl. Phys.* **45**. 2497 (2006).

Chapter 6

Effects of P on Amorphous Ruthenium-Phosphorus Alloy Films for Liner Application in Cu Interconnect

6.1 INTRODUCTION

Copper has replaced aluminum as the interconnect material in advanced VLSI devices due to its superior electrical conductivity and intrinsic electromigration (EM) resistance, which brought about significant changes in processes and materials. Liner materials are placed between Cu and intermetal dielectric to prevent Cu diffusion and improve adhesion. The liner can include an adhesion promoting layer, a diffusion barrier, and a Cu seed layer, and currently, a physical vapor deposition (PVD) TaN/Ta/Cu stack is most widely used. However, due to the poor step coverage of PVD, and the thickness requirements for sub 32 nm devices [1], extensive studies have been performed in the search for new liner materials [2,3].

Ru has been considered as a promising liner material for its low resistivity, chemical inertness, strong adhesion with Cu, and low Cu solubility. However, 3D mode (Volmer-Weber) growth of Ru makes it difficult to form conformal and thin films of a few nanometers, especially inside of high aspect ratio damascene features. The microstructure of Ru films, which is polycrystalline with columnar grains, leads poor Cu diffusion barrier performance [4,5]. Alloying Ru to generate an amorphous film is one approach to form conformal thin films that may function as the seed layer and diffusion barrier.

We have recently reported chemical vapor deposition (CVD) amorphous Ru(P) alloy films containing ~15% P (*n.b.*, compositions on an atom basis) grown at 575 K using a single chemical source, $RuH_2(PMe_3)_4$, ($Me=CH_3$), which remain amorphous upon annealing at 675 K for 3 hr [6]. First principles density functional theory (DFT) calculations indicated p – d hybridization between P and Ru atoms, which contributed to stabilizing the Ru(P) alloy structure. Amorphous Ru(P) alloys were energetically favored over crystalline Ru(P) when the percent of P was greater than 20%. Surface studies illustrated that P incorporated by a stepwise demethylation of adsorbed $P(CH_3)_3$ [7], and this suggested the possibility of forming amorphous Ru(P) alloy films using dual chemical sources. Indeed, amorphous Ru(P) films could be formed using $Ru_3(CO)_{12}$ and $P(CH_3)_3$ or $P(C_6H_5)_3$, and a 15 nm amorphous Ru(P) film containing ~15% P was formed at 575 K [8]. Using low energy ion scattering spectroscopy (LEISS) and X-ray photoelectron spectroscopy (XPS), the thinnest continuous Ru(P) film grown from $Ru_3(CO)_{12}$ and $P(CH_3)_3$ on SiO_2 was 7.1 nm, and ~0.4 nm Cu (*i.e.* 2 – 3 monolayers) wetted on the Ru(P) surface having ~15% P.

In this study, we report how film properties, required for barrier/seed application, are affected by the presence of P in Ru(P) films grown with $RuH_2(PMe_3)_4$, or $Ru_3(CO)_{12}$ and $P(CH_3)_3$. The effect of P and C concentrations on microstructure and film resistivity is explored using XPS, X-ray diffraction (XRD), and four point probe. The step coverage of Ru and Ru(P) films are analyzed with cross sectional transmission electron microscopy (TEM). The barrier property and Cu adhesion of amorphous Ru(P) films are evaluated by annealing studies, and first principles DFT calculations are performed to understand the impact of P at the Cu/Ru(P) interface.

6.2 EXPERIMENTAL DETAILS

Film growth was carried out in a deposition and analysis facility consisting of a vacuum sample transfer system, load lock, XPS system (Physical Electronics 3057; Mg Kα), CVD chamber, and a PVD chamber equipped with direct current magnetron sputtering guns. The stainless steel CVD chamber is a cold-wall vessel (base pressure 5×10^{-8} mTorr) and the SiO_2/Si(100) substrates were heated radiatively from below. Thermally grown SiO_2/Si(100) 200 mm wafers were supplied by Sematech. The wafers were cut into 20 × 20 mm pieces and heated to the growth temperature under vacuum. For barrier tests, SiO_2 was removed before Ru(P) deposition using TIMETCH^{TM} solution for 10 min. The synthesis of $RuH_2(PMe_3)_4$ is described elsewhere [9]; the solid compound was sublimed at 355 K to obtain sufficient vapor pressure and delivered to the CVD chamber using flowing Ar through a heated gas line and shower head. $Ru_3(CO)_{12}$ (Strem Chemical; 99%) was sublimed at 355 K and delivered to the CVD chamber using 2.5 – 5.0 standard cm^3 per min (sccm) of flowing H_2 through a heated gas line and shower head. $P(C_6H_5)_3$ (Strem Chemical, 99%) was sublimed at 335 K and delivered using 5 – 10 sccm of flowing Ar through separately heated lines. $P(CH_3)_3$ (Strem Chemical, 99%) was dosed directly into the reaction chamber; the flow was controlled using a leak valve. The deposition was carried out at 200 – 400 mTorr. Ex situ XPS chemical state analysis was performed with a Physical Electronics 5700, which is fitted with a monochromatic Al Kα source. Crystallinity is established using grazing angle (1°) XRD (Bruker-Nonius D8). TEM analysis was performed with JOEL 2010F or FEI TECNAI G2 F20 operated at 200 kV. LEISS was carried out in situ using 1 kV He^+. The samples were sputter cleaned with 2 kV Ar^+ before both XPS and LEISS.

Atomic structure and energy calculations were performed using the DFT program package VASP (Vienna Ab initio Simulation Package) with the generalized gradient approximation (GGA) function derived by Perdew and Wang (PW91). A plane wave basis set for valence electron states and Vanderbilt ultrasoft pseudopotentials for core-electron interactions were employed, and Brillouin zone sampling was performed using Monkhorst-Pack type k-point meshes. A plane-wave cutoff energy of 400 eV was used and the Brillouin zone integration was performed using a 2×2×1 k-point mesh. All atoms were fully relaxed using the conjugated gradient method until residual forces on constituent atoms became smaller than 5×10^{-2} eV/Å.

6.3 RESULTS AND DISCUSSION

Figure 6.1 presents the influence of P and C concentrations on the microstructure and the electrical resistivity of Ru(P) films grown from $Ru_3(CO)_{12}$ and $P(CH_3)_3$ or $P(C_6H_5)_3$ at 575 K. The P and C concentrations are determined by XPS. Due to the overlapping C 1s and Ru 3d XPS peaks and vastly different sensitivity factors, calculating the C concentration in Ru is not straightforward, however this can be overcome by fitting the Ru $3d_{5/2}$ and $3d_{3/2}$ peaks, assuming pure Ru has a peak intensity ratio of 1.5 based on the relative degeneracy of the 3d doublet peaks. Measurement and fitting conditions are carefully optimized using a 99.95% PVD Ru target to minimize possible fitting errors.

The microstructure of Ru(P) alloy films are closely related to P concentration in the films as shown in Figure 6.1 (a). The films containing more than ~13% P, on a C free basis, feature amorphous microstructure. Our previous *ab initio* molecular dynamics calculation demonstrated that the amorphous phase was most stable when more than 20% of P was incorporated [8], and experimentally the minimum P concentration in the amorphous Ru(P) in this study is ~13%, on a C free basis. The difference between

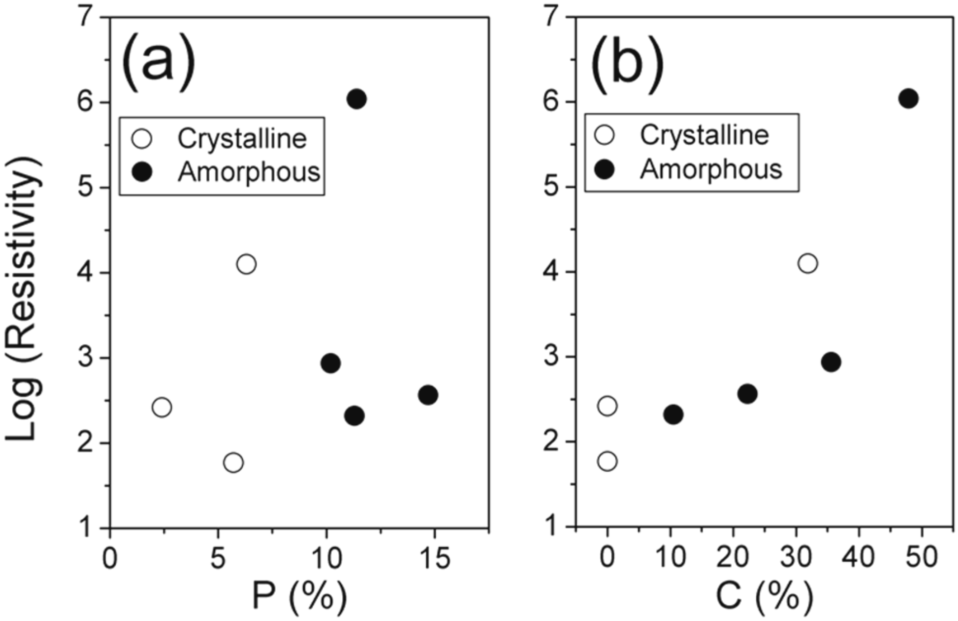

Figure 6.1 Electrical resistivity of amorphous and crystalline Ru(P) films grown with $Ru_3(CO)_{12}$ and $P(CH_3)_3$ or $P(C_6H_5)_3$ at 575 K as a function of (a) P percentage, and (b) C percentage in the films.

the experiment (13% P) and the simulation (20% P) could be attributed to the effect of the C impurity, which was not considered in the calculations, or possible microscopic non-uniform P distribution in the Ru(P) films [10].

Carbon does not have a significant impact on microstructure as shown in Figure 6.1 (b). Possibly because of the small atomic size of C it preferentially locates in interstitial sites in the disordered lattice of Ru(P) rather than substituting for Ru or P sites. Although further study will be needed to understand how C exists in Ru(P) alloys, the lack of Ru-C compounds and strong Ru-Ru and C-C bonds suggest that C would not be an efficient alloying element for a stable amorphous Ru alloy. Unlike Ru-C, the Ru-P system features possible Ru_2P, RuP, and RuP_2 compounds, and this chemical interaction between Ru and P may also be a contributing factor in amorphous alloy formation during CVD [11]. Interactions between Ru and P are also supported by our previous density of state (DOS) analysis of amorphous Ru(P) alloys, which indicates hybridization between Ru 4d and P 3p orbitals [8]. Carbon impurities strongly and negatively impact the electrical resistivity as shown in Figure 6.1 (b); resistivity increases with higher C content in Ru(P) films. According to the DOS analysis, amorphous Ru(P) alloy containing 20% P is metallic, and impurities like C can act as scattering center for electron transfer, degrading electrical conductance of Ru(P) films. The lowest resistivity for an amorphous Ru(P) alloy containing 11.3% P and 10.5% C was 210 $\mu\Omega\cdot$cm.

Figure 6.2 presents the step coverage in trench patterns of the crystalline Ru film grown with $Ru_3(CO)_{12}$ only and the amorphous Ru(P) films from $RuH_2(PMe_3)_4$ and $Ru_3(CO)_{12}$ with $P(CH_3)_3$. The trenches are ~1.0 μm deep and 0.13 – 0.18 μm wide. The substrate temperatures during film growth are 475 K and 575 K for Ru and Ru(P) films, respectively. The lower substrate temperature for Ru from $Ru_3(CO)_{12}$ likely enhances the step coverage by suppressing the reactive sticking coefficient of $Ru_3(CO)_{12}$. Precursor molecules that strike a surface undergo either decomposition (reaction), desorption, or diffusion, and higher substrate temperatures degrade step coverage because the decomposition rate increases much more rapidly than desorption and diffusion rates as temperature increases [12]. However, even with the lower temperature and larger trenches, most of CVD Ru is found near the top of trenches, and only some grains are visible within the trenches. The large size (~15 nm) and low density of grains indicates strong 3D (Volmer-Weber) growth mode of Ru due to its high surface energy ($\gamma_{Ru(001)} = 3.05\ J/m^2$ and $\gamma_{SiO_2} = 1.15 - 2.00\ J/m^2$) [13,14].

Amorphous Ru(P) from $Ru_3(CO)_{12}$ and $P(CH_3)_3$ shows improved coverage compared to Ru, although it is not fully continuous in the trenches. This can be explained by the reduced adsorption/reaction sites available for $Ru_3(CO)_{12}$ in the presence of $P(CH_3)_3$. $P(CH_3)_3$ adsorbs on Ru surface as low as 80 K and undergoes complete demethylation to P by 450 K [7]. Possibly due to the adsorbed $P(CH_3)_3$ molecules, $Ru_3(CO)_{12}$ has less chance of finding an adsorption/reaction site, and will

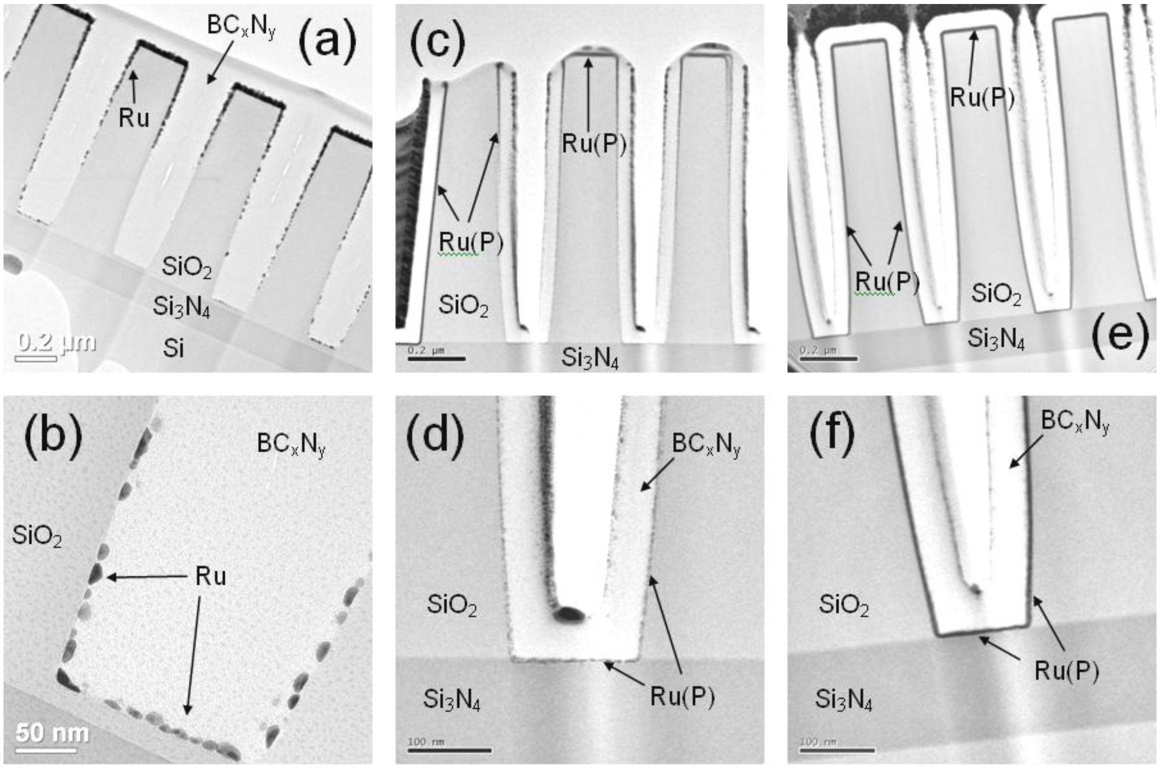

Figure 6.2 Cross sectional TEM images of (a) and (b) the CVD Ru film grown with $Ru_3(CO)_{12}$ only at 475 K, (c) and (d) the CVD Ru(P) film grown with the dual source, $Ru_3(CO)_{12}$ and $P(CH_3)_3$, at 575 K, and (e) and (f) the CVD Ru(P) film grown with the single source, $RuH_2(PMe_3)_4$, at 575K.

have a greater possibility to migrate deeper into the trenches. The reduced reactivity of $Ru_3(CO)_{12}$ with $P(CH_3)_3$ is also supported by the lower growth rate with higher $P(CH_3)_3$ dosing. The growth rates of Ru(P) with 5.7% and 11.3% P are 5.7 Å/min and 2.5 Å/min, respectively.

At the bottom of the trench, Ru(P) from the dual sources also features a 3D growth mode as shown in Figure 6.2 (d), however the grains are much smaller and more crowded than for Ru (Figure 6.2 (b)), which can be explained by the differences in nucleation densities of amorphous and crystalline phases. According to capillary theory of heterogeneous nucleation, nucleation energy and the ratio of nucleation rates of amorphous and crystalline phases can be expressed as [15],

$$G^* = \frac{16\pi}{3}\frac{\gamma^3 v^2}{\Delta G^2} f(\theta) \tag{6.1}$$

$$\frac{N_a}{N_c} = \exp\left[\frac{(G_c^* - G_a^*)}{kT}\right] \tag{6.2}$$

where γ is the surface energy, ν is the molar volume, ΔG is the Gibbs energy for the reaction, $f(\theta)$ is shape factor, which is a function of the contact angle, θ, and N is the nucleation density. Subscripts *a* and *c* denote amorphous and crystalline phases, respectively. Comparing the nucleation energies for amorphous Ru(P) and crystalline Ru is not straightforward because of the different film composition and growing conditions. However, simple arguments can be made by assuming that the molar volumes and shape factors are equal for both films. These are reasonable assumptions considering that the molar volume of amorphous and crystalline metal alloys differs by only a few percents [8], and both Ru(P) and Ru have a 3D growth mode on SiO_2. Therefore, provided that ΔG of both films are similar, the nucleation energy, G^*, strongly depends on the surface energies. The surface energy, and thus the nucleation energy, of amorphous Ru(P) should be lower than those of crystalline Ru because of its random structure and the dilution effect by a low surface energy element, P. Faster nucleation of meta-stable phases than of stable phases is found in many systems, such as condensation of super cooled liquid or saturated gas phases [16], and solid state reactions [17]. This phenomenon is known as Ostwald's step rule, which is explained with the lower nucleation energy and smaller critical nuclei size of meta-stable phases [18,19]. Higher nucleation density is beneficial in forming thinner films, especially when growth follows a 3D mode. Indeed, our previous study shows that ~7 nm Ru(P) grown with the dual sources on SiO_2 is fully continuous based on LEISS analysis [8], while crystalline CVD Ru from $Ru_3(CO)_{12}$ needs ~20 nm of film to become continuous on SiO_2 [20]. The film thickness is established using the attenuation of XPS Si 2p peak, and confirmed with TEM analysis.

The best step coverage is obtained with the Ru(P) films grown with $RuH_2(PMe_3)_4$, as shown in Figure 6.2 (e) and (f). The Ru(P) film is fully continuous within the trenches of a 8:1 aspect ratio, and the film thicknesses at the top and in the trench are 8 nm and 5 nm, respectively. Considering that both single and dual sources have $P(CH_3)_3$ that reduces available adsorption/reaction sites for Ru precursors, the different Ru(P) film step coverage can be explained by differences in the reactive sticking coefficient of the Ru precursors. $Ru_3(CO)_{12}$ can easily lose carbonyl ligands to leave Ru behind, however complete decomposition may be more difficult for $RuH_2(PMe_3)_4$. This is supported by the fact that Ru(P) film can be grown with $RuH_2(PMe_3)_4$ above 525 K, while Ru films are grown with $Ru_3(CO)_{12}$ at temperatures as low as 425 K [21]. The lower reactivity of $RuH_2(PMe_3)_4$ offers more chance to migrate into the trenches and form more conformal films.

The barrier property of CVD Ru(P) film grown with the dual source is compared with PVD Ru films by measuring the sheet resistances with a four point probe after annealing. The films are placed between a Si(100) substrate and 150 nm PVD Cu, and annealed at 575 K under N_2/H_2 gas for various times. Since Ru-silicide, which degrades film integrity, can be formed at ~675 K, a relatively low annealing temperature is used in this study. Several studies show that PVD Ru films have poor barrier property [4,5]. Coincidently, our study shows that 6.5 nm PVD Ru film impeded Cu diffusion for 15 min, but failed after 1 hr based on the resistance as shown in Figure 6.3. An initial decrease in resistance is due to grain growth and defect removal in Cu. As Cu diffuses through the Ru film to form Cu-silicide, a significantly increased resistance is recorded as shown in Figure 6.3. Thicker PVD Ru requires a longer annealing time for failure, and 26 nm

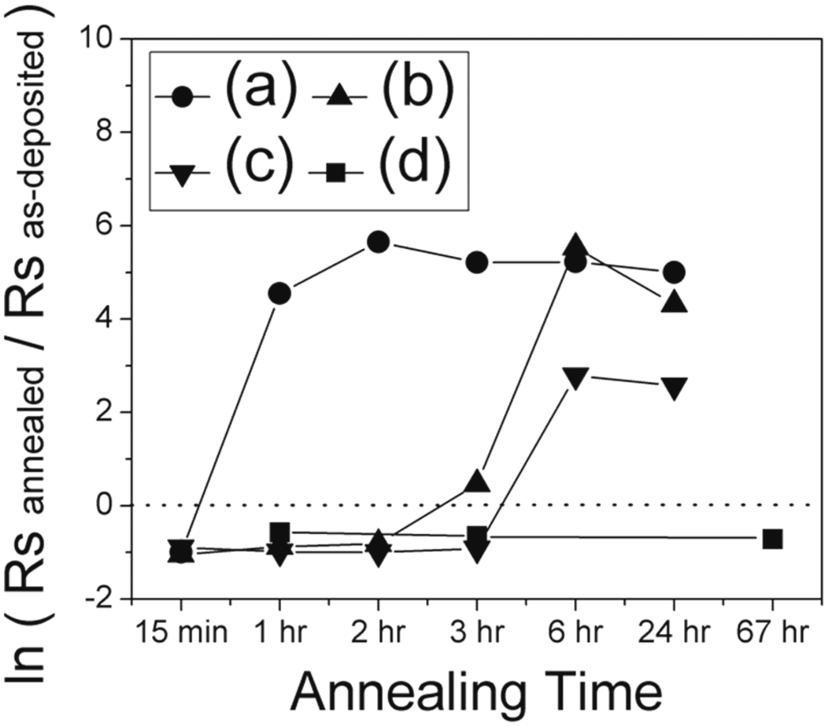

Figure 6.3 Changes in the sheet resistance of 150 nm PVD Cu / PVD Ru or CVD Ru(P) / Si stacks before and after annealing at 575 K for various annealing times. (a) 6.5 nm PVD Ru, (b) 13 nm PVD Ru, (c) 26 nm PVD Ru, and (d) 28 nm amorphous CVD Ru(P) grown with $Ru_3(CO)_{12}$ and $P(CH_3)_3$ at 575 K.

PVD Ru fails after 6 hr annealing. Although the exact failure time is not clear on the annealing study, Cu diffusivity can be roughly estimated. The average diffusion length of Cu can be determined with [22],

$$L^2 = 4Dt \tag{6.3}$$

where L is the diffusion length, D is the Cu diffusivity, and t is the annealing time. The diffusivity of Cu in PVD Ru is determined to be 6.6×10^{-17} cm^2/s at 575 K. Cu diffusivity data in Ru are not reported. Herein we compare it with Cu diffusivity in TaN films (Table 6.1) to illustrate a possible diffusion path. Cu diffusivities are calculated using the reported D_0 and E_a values. The Cu diffusivity in PVD Ru is significantly higher than the diffusivity in a TaN lattice, and comparable to the Cu diffusivities through TaN grain boundaries. This suggests that Cu is penetrating the PVD Ru along the grain boundaries. TaN films (d) and (e) in Table 6.1 are reported to be polycrystalline having disordered grain boundaries, and TaN film (c) has a columnar structure with larger and ordered grain boundaries. Grain boundary diffusion is dependent on the microstructure of barrier films, and the columnar structure is known to have the poorest barrier performance [3]. Cu diffusivity in Ru is even higher than the diffusivity in TaN film (c), confirming that PVD Ru is not an appropriate barrier for Cu diffusion. On the other hand, CVD Ru(P) film, having comparable thickness with the PVD Ru failed after 6 hr annealing, does not show an increase in resistance after 67 hr

Table 6.1 Cu diffusivity in TaN films.

	Barrier	Diffusion path	D_0 (cm^2/s)	E_a (eV)	D_{Cu} at 575 K	Ref.
(a)	PVD	Lattice	160	3.27	3.6×10^{-27}	28
(b)	PVD	Lattice	6.7×10^{-4}	2.7	1.9×10^{-27}	29
(c)	PVD	Grain	2.36×10^{-11}	0.8	2.3×10^{-18}	30
(d)	PVD	Grain	2.8×10^{-10}	1.3	1.1×10^{-21}	29
(e)	ALD	Grain	6.2×10^{-9}	1.2	2.0×10^{-19}	31

annealing. Although Cu diffusivity in CVD Ru(P) film could not be determined because it did not fail, this suggests a superior barrier property over PVD Ru having columnar structure. The advantage of amorphous films in blocking Cu diffusion can be found elsewhere [23,24], and amorphous Ru(P) is expected to have improved barrier capability over polycrystalline Ru. However, to be noted here is that the Ru(P) film grown with the dual source on Si(100) does not feature fully amorphous microstructure, possibly due to the film growth on a single crystalline substrate.

Cu adhesion with CVD Ru(P), PVD Ta, and PVD TaN films was studied using LEISS and XPS after annealing at 675 K for 1 hr with N_2/H_2. Amorphous Ru(P) film containing ~15% P was grown on SiO_2 with $Ru_3(CO)_{12}$ and $P(CH_3)_3$, and the 10nm PVD Cu was deposited on 30 nm Ru(P), Ta, and TaN, without exposure to air. LEISS is very surface sensitive due to the low kinetic energy of He^+ ions. Figure 6.4 (A) shows that the surface is fully covered with Cu atoms before annealing. Ta peaks emerge at $E/E_0 = 0.89$ for the Cu/Ta and Cu/TaN samples after annealing, however only Cu peak is visible at $E/E_0 = 0.80$ for the Cu/Ru(P) sample, indicating stronger Cu adhesion with Ru(P) than Ta or TaN. Assuming the Cu/Ru(P) surface is completely covered with Cu, and ignoring any attenuation effect of photoelectrons, Cu surface coverage can be determined from the intensity ratio of the XPS Cu $2p_{3/2}$ peaks at 932.6 eV referenced against Cu/Ru(P). From Figure 6.4 (B), the Cu coverages on Ta and TaN after annealing are 63% and 26%, respectively. This is consistent with the studies that show stronger Cu

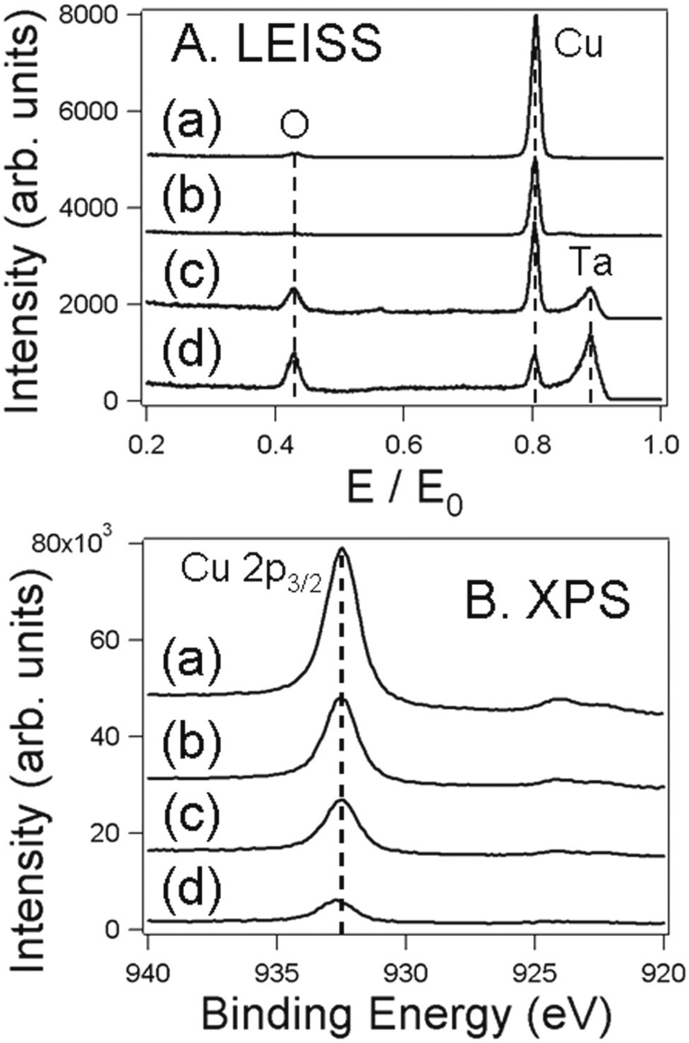

Figure 6.4 LEISS result (A) and XPS Cu $2p_{3/2}$ peak (B) of, (a) PVD Cu without annealing, (b) after annealing PVD Cu / 30 nm CVD Ru(P) grown with $Ru_3(CO)_{12}$ and $P(CH_3)_3$, (c) PVD Cu / 30 nm PVD Ta, and (d) PVD Cu / 30 nm PVD TaN.

adhesion with Ta than TaN; from contact angle measurements, the adhesion energies of Cu/Ta and Cu/TaN were reported to be 2.17 and 1.85 J/m^2 [25], and first principles DFT calculation also showed ~20% lower adhesion strength in Cu/TaN than Cu/Ta [26].

In order to understand the impact of P on Cu adhesion in amorphous Ru(P) films, ideal work of separation, which is the work required to separate unit area of interface, was calculated using the first principles DFT. Ideal work of separation, W_{sp}, can be defined as below,

$$W_{sp} = \frac{\left(E_{Cu} + E_{Ru} - E_{Cu/Ru}\right)}{A} \tag{4}$$

where $E_{\mathrm{Cu/Ru}}$ is the total energy of a Cu/Ru supercell, E_{Cu} and E_{Ru} are the total energies of Ru and Cu slabs with vacuum, respectively, and A is the total interface area. The supercells explored in this study, c-Cu/c-Ru, a-Cu/a-Ru, and a-Cu/a-Ru(P) with 16.7% P, are shown in Figure 6.5. The 16.7% P is at the Cu/Ru interface, and the subscripts a and c denote amorphous and crystalline phases, respectively. The c-Cu/c-Ru and a-Cu/a-Ru supercells are composed of 60 Cu/60 Ru and 60 Cu/72 Ru atoms, respectively, and two Ru atoms at the a-Cu/a-Ru interface are substituted with P atoms to generate the a-Cu/a-Ru(P) supercell. Normalized W_{sp} of a-Cu/a-Ru and a-Cu/a-Ru, based on c-Cu/c-Ru, are 1.06 and 0.88, respectively. Considering that amorphizing Cu and Ru interface enhances adhesion strength (W_{sp}) by 6%, placing 16.7% P at the Cu/Ru interface degraded adhesion strength by 17%, suggesting that P terminates strong Cu-Ru bonds at

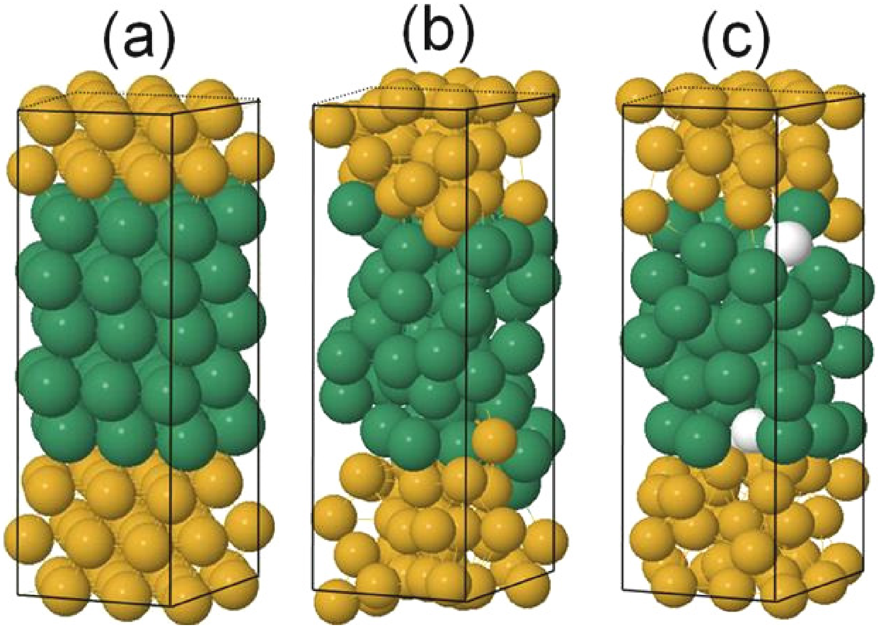

Figure 6.5 Cu/Ru interface model structures used in the DFT calculation for W_{sp}. (a) c-Cu/c-Ru, (b) a-Cu/a-Ru, and (c) a-Cu/a-Ru(P) with 16.7% P. Large grey and dark balls represent Cu and Ru atoms respectively, and small white balls indicate P atoms.

the interface. From the c-Cu/c-Ru contact angle value reported [27], the adhesion energy is determined to be 2.94 J/m^2 assuming the surface energy of Cu is 1.7 J/m^2. Considering the 12% decrease in *Wsp* between c-Cu/c-Ru and a-Cu/a-Ru(P) with 16.7% P at the interface, the adhesion energy of a-Cu/a-RuP is approximated to be 2.59 J/m^2. Although P degrades adhesion with Cu, the adhesion energy is still higher than those of Cu/Ta (2.17 J/m^2) and Cu/TaN (1.85 J/m^2),[25] because of the strong Cu-Ru bonds.

6.4 SUMMARY

Amorphous Ru(P) films are chemically grown at 575 K using a single source, $RuH_2(PMe_3)_4$, or dual sources, $Ru_3(CO)_{12}$ and $P(CH_3)_3$ or $P(C_6H_5)_3$. P concentration shows a dominant impact on the film microstructure, however C impurity which is not an efficient amorphizing element, degrades electrical conductivity. While improved step coverage is obtained in the presence of $P(CH_3)_3$ with $Ru_3(CO)_{12}$, the most conformal Ru(P) film is formed with $RuH_2(PMe_3)_4$. Cu diffusivity in PVD Ru is approximated to be 6.6×10^{-17} cm^2/s at 575 K, suggesting Cu diffusion along PVD Ru grain boundaries. The superior barrier property of amorphous Ru(P) over PVD Ru is observed in the annealing study at 575 K. First principles DFT calculations suggest 12% degraded adhesion strength for the amorphous Cu/Ru(P) with 16.7% P at the interface compared to the crystalline Cu/Ru interface, due to the presence of P at the interface. However, due to the strong Ru-Cu bonds, amorphous Ru(P) still forms stronger adhesion to Cu than do Ta and TaN to Cu, as observed in the annealing study performed at 675 K.

6.5 REFERENCES

[1] International Technology Roadmap for Semiconductors, 2006 Update, http://public.itrs.net (2006).

[2] H. Kim, *J. Vac. Sci. Technol. B*, **21**, 2231 (2003).

[3] A. E. Kaloyeros and E. Eisenbraun, *Annu. Rev. Mater. Sci*. **30**, 363 (2000).

[4] R. Chan, T. N. Arunagiri, Y. Zhang, O. Chyan, R. M. Wallace, M. J. Kim, T. Q. Hurd, *Electrochem. Solid-State Lett.* **7**, G154 (2004)

[5] J. Tan, X. Qu, Q. Xie, Y. Zhou, and G. Ru, *Thin Solid Films*, **504**, 231 (2006).

[6] J. Shin, A. Waheed, W. A. Winkenwerder, H-W. Kim, R. A. Jones, G. S. Hwang, J. G. Ekerdt, *Thin Solid Films*, **515**, 5298 (2007).

[7] H.-S. Tao, U. Diebold, N. D. Shinn, and T. E. Madey, *Surf. Sci*. **375**, 257 (1997)

[8] J. Shin, H-W. Kim, G. S. Hwang, J. G. Ekerdt, *Surf. Coat. Technol.* **201**, 9256 (2007).

[9] J. Shin, A. Waheed, K. Agapiou, W. A. Winkenwerder, H-W. Kim, R. A. Jones, G. S. Whang, and J. G. Ekerdt, *J. Amer. Chem. Soc.* **128**, 16510 (2006).

[10] T. Egami and Y. Waseda, *J. Non-Cryst. Solids*, **64**, 113 (1984).

[11] V. B. Chernogorenko, V. G. Ivanchenko, L. Ya. Kulik, in Binary Phase Diagrams, edited by. T. B. Massalski, H. Okamoto, P. R. Subramanian, and L. Kacprzak, (ASM International, Materials, Park, OH 1990) p 2979.

[12] G. B. Raupp and T. S. Cale, *Chem. Mater* **1**, 207 (1989).

[13] H. L. Skriver and N. M. Rosengaard, *Phys. Rev. B* **46**, 7157 (1992).

[14] P. Staszczuk, B. Janczuk, and E. Chibowski, *Mater. Chem. Phys* **12**, 469 (1985).

[15] H. Ohring, Materials Science of Thin Films, 2nd ed. Academic Press, San Diego, CA 2002.

[16] M. Birkholz, B. Selle, W. Fuhs, S. Christiansen, H. P. Strunk, and R. Reich, *Phys. Rev. B* **64**, 085402 (2001).

[17] K. N. Tu, S. R. Herd, and U. Gösele, *Phys. Rev. B* **43**, 1198 (1991).

[18] W. Ostwald, *Z. Phys. Chem.* **22**, 306 (1897)

[19] I. N. Stranski and D. Totomanow, *Z. Phys, Chem.* **A168**, 399 (1933).

[20] J. Shin, D. Gay, Y-M. Sun, J.M. White, J.G. Ekerdt, in: D.G. Seiler, A.C. Diebold, R. McDonald, .R. Ayre, R.P. Khosla, S. Zollner, E.M. Secula (Eds.), *AIP Conf. Proc.* **788**, 482 (2005).

[21] Q. Wang, J. G. Ekerdt, D. Gay, Y. Sun, and J. M. White, *Appl. Phys. Lett*. **84**, 1380 (2004).

[22] P. Shewmon, Diffusion in Solids, 2nd ed. The Minerals, Metals, and Materials Society, Warrendale, PA 1989.

[23] H. Kim, C. Cabral, Jr., C. Lavoie, and S. M. Rossnagel, *J. Vac. Sci. Technol. B* **20**, 1321 (2002).

[24] R. Hübner, M. Hecker, N. Mattern, A. Voss, J. Acker, V. Hoffmann, K. Wetzig, H. –J. Engelmann, E. Zschech, H. Heucer, and Ch. Wenzel, *Thin Solid Films* **468**, 183 (2004).

[25] O. Straten, Y. Zhu, J. Rullan, K. Dunn, and K. E. Kaloyeros, *J. Mater. Res*. **21**, 255 (2006).

[26] H. Simka, S. Shankar, C. Duran, and M. Haverty, *Mater. Res. Symp. Proc.* **863**, B9.2.1 (2005).

[27] H. Kim, Y. Naito, T. Koseki, T. Ohba, T. Ohta, Y. Kojima, H. Sato, and Y. Shimogaki, *Jpn. J. Appl. Phys.* **45**, 2497 (2006).

[28] H. Wang, A. Tiwari, X. Zhang, A. Kvit, and J. Narayan, *Appl. Phys. Lett*. **81**, 1453 (2002).

[29] T. Oku, E. Kawakami, M. Uekubo, K. Takahiro, S. Yamaguchi, and M. Murakami, *Appl. Surf. Sci.* **99**, 265 (1996).

[30] J. Lin and C. Lee, *J. Electrochem. Soc.* **146**, 3466 (1999).

[31] H. Kim, C. Lavoie, M. Copei, W. Narayanan, D. G. Park, and S. M. Rossnagel, *J. Appl. Phys*. **95**, 5848 (2004).

Chapter 7

Summary

7.1 CONCLUSION

A screening study of CVD/ALD Ru precursors was performed. The Ru precursors studied include: dodecacarbonyltriruthenium (Ru-carbonyl), $Ru_3(CO)_{12}$, (η^6-benzene)(η^4-1,3-cyclohexadiene)ruthenium, $Ru(C_6H_6)(C_6H_8)$, (2,4-dimethyl-pentadienyl(ethyl-cyclopentadienyl)ruthenium (DER), $Ru(C_7H_{11})(C_7H_9)$, and bis(2,4-dimethylpentadienyl)-ruthenium (DMPD), $Ru(C_7H_{11})_2$. CVD growth with $Ru_3(CO)_{12}$ at 425 – 475 K resulted in poor step coverage due to the high sticking coefficient of $Ru_3(CO)_{12}$. $Ru(C_6H_6)(C_6H_8)$ starts to decompose to form Ru film at 450 K, and, compared to $Ru_3(CO)_{12}$, smoother film and improved step coverage are obtained due to its higher nucleation density. The DER precursor needs oxygen to form Ru at 475 K. Film growth in the ALD mode with DER resulted in the growth of multi atomic layers per a cycle (~1.2 nm/cycle), suggesting that the film follows CVD mode growth due to the non self-limiting adsorption character of DER molecules. The DMPD precursor starts decomposition to form polycrystalline Ru from 475 K. No precursor shows self-limiting adsorption behavior and reactivity with H_2, indicating that the precursors are not available for thermal ALD in reducing chemistry. Also, all films grown with the precursors studied are polycrystalline Ru with columnar structure, which is not suited for a Cu diffusion barrier.

Chemical and physical methods are used to deposit Ru films on a SiO_2 substrate with the goal of realizing ultrathin (3-5 nm) and continuous Ru films for Cu metallization. CVD Ru films are grown from $Ru_3(CO)_{12}$ precursor at 425 – 525 K, and PVD Ru films are grown with a DC magnetron sputtering system at room temperature. AFM reveals the CVD Ru films to have a rougher surface than PVD Ru; RMS roughness of CVD and PVD Ru films are 1.43 nm and 0.11 nm, respectively. Surface coverage versus XPS intensity study illustrate that CVD Ru follows strong 3D growth mode. The thickness for the thinnest continuous CVD Ru film on SiO_2 is determined to be ~20 nm by TEM analysis. Film thickness and continuity established by XPS and LEISS shows considerable deviation form the TEM analysis result because of the shadowing effect of He^+ ions by columnar Ru grains.

Amorphous Ru(P) films containing ~15% P grown from *cis*-dihydridotetrakis-(trimethylphosphine)ruthenium(II), *cis*-$RuH_2(P(CH_3)_3)_4$ at 525 – 575 K are developed. XPS shows Ru $3d_{5/2}$ and P $2p_{3/2}$ peaks at 280.0 and 129.8 eV, indicating that both Ru and P are in zero-valent states. The films contain ~10% C as impurity. Amorphous microstructure of Ru(P) films are determined by XRD and TEM. The films are metastable; remain amorphous upon heating for 3 hr at 675 K, and starts recrystallization at ~ 775 K. Separate surface studies illustrate the trimethylphosphine ligands undergo demethylation and desorb at the growth conditions and readsorb, and subsequently incorporate the P into the Ru film. A first principles molecular dynamics study shows that Ru(P) alloys with moderate P content can result in glassy structure exhibiting the topological and strong chemical short-range order. In the $Ru_{80}P_{20}$ structure, the P-centered polyhedra prefer the tri-capped trigonal prism packing (TTP) phase with Veronoi index <0,3,6,0>. Phosphorus and its manner of incorporatation appear responsible for the amorphous-like character of CVD Ru(P) films.

Amorphous/crystalline Ru(P) films are grown from dual chemical sources, $Ru_3(CO)_{12}$ and $P(CH_3)_3$ or $P(C_6H_5)_3$ with flowing H_2 or Ar at 575 K. The amount of P and C in Ru(P) films depends on the delivery gas and the alkylphoshphine source. The microstructure changed with the percentage P; amorphous films formed provided the percentage of P exceeded ~13%, in a C free basis. Film resistivity was most sensitive to the C impurity, and a 15 nm amorphous film with 11.2% P and 10.5% C has a resistivity of 210 μΩ·cm. Amorphous Ru(P) films as thin as 7 nm are grown on SiO_2 using $Ru_3(CO)_{12}$ and $P(CH_3)_3$ with H_2. Ion scattering studies reveal that ~0.4 nm PVD Cu wets amorphous Ru(P) surface. DOS analysis of the Ru(P) alloy reveals metallic character of the alloy and hybridization between Ru 4d and P 3p orbitals, which contributes stabilizing the amorphous structure. First principles DFT calculations show

Ru and P are intermixable, and predict the amorphous structure should be most stable above 20% P.

Amorphous Ru(P) films grown at 575 K using a single source precursor, *cis*-$RuH_2(P(CH_3)_3)_4$, or dual sources, $Ru_3(CO)_{12}$ and $P(CH_3)_3$ or $P(C_6H_5)_3$, are studied to explore the effect of P on the film properties required for liner applications. Co-dosing $P(CH_3)_3$ with $Ru_3(CO)_{12}$ improves film step coverage, however the most conformal Ru(P) film is obtained with *cis*-$RuH_2(P(CH_3)_3)_4$. A fully continuous 5 nm Ru(P) film is formed within 1 μm deep, 8:1 aspect ratio trenches. Cu diffusion studies at 575 K suggest improved barrier properties of amorphous Ru(P) films compared to PVD Ru. Cu diffusivity in PVD Ru is approximated to be 6.6×10^{-17} cm^2/s at 575 K, indicating fast Cu diffusion along grain boundaries. While 26 nm PVD Ru failed after 6 hr annealing by Cu penetration, 28 nm amorphous Ru(P) survived after 67 hr annealing. First principles DFT calculations illustrate degraded Cu/Ru adhesion by the presence of P at the interface, however, due to the strong Ru-Cu bonds, amorphous Ru(P) forms a stronger interface with Cu than Ta and TaN do. From the contact angle data reported and the DFT calculation in this study, adhesion energies of Cu/Ru(P), Cu/Ta, and Cu/TaN are approximated to be 2.59, 2.17, and 1.85 J/m^2, respectively, which are consistent with the annealing study that showed Cu adhesion strength in the order of Ru(P) alloy > PVD Ta > PVD TaN.

7.2 RECOMMENDATIONS FOR FUTURE WORK

This work was performed to explore liner materials targeting the Cu interconnect for sub 32 nm node devices. Formation of the amorphous Ru(P) films suggests the possibility of modifying the film microstructure and properties of Ru films. While amorphous Ru(P) films show promising improvements over polycrystalline Ru films, especially in the film conformality and the barrier property, further studies remain to be done to make this a technological application. Foremost, the impact by P incorporation on the electrical conductivity and the Cu adhesion property needs to be fully understood. The stability of P in Ru(P) films and its interaction with the to Cu and dielectric interfaces at elevated temperatures need to be studied. Especially, interactions of Ru(P) films with ultra low-k materials, which have a porous matrix and low surface energy, are recommended for exploration.

The barrier property of the amorphous Ru(P) film was evaluated using an annealing experiment at 575 K employing Cu/Ru(P)/Si(100) stacks. While the temperature was high enough for Cu penetration through polycrystalline PVD Ru films, the amorphous Ru(P) film did not fail after 67 hr annealing because of the low annealing temperature and slow Cu diffusion. Failure might happen when a thinner Ru(P) film is used, however forming ultrathin amorphous film on single crystalline Si substrate might also be challenging. Ultimately, the barrier property of Ru(P) films should be evaluated by electrical tests under a bias temperature stress (BTS) condition, and compared to conventional Ta and TaN barriers. BTS test is a more standard and practical method for barrier property characterization than the annealing method. It is also more suited for studying the effect of microstructure on barrier property because test temperatures are significantly lower than the recrystallization temperature of the amorphous Ru(P) alloy and the films are grown on amorphous SiO_2 substrates.

One of the issues of the Ru(P) films is the degradation in electrical conductivity. This can be related to the amorphous structure and impurities. Carbon incorporated by incomplete demethylation of $P(CH_3)_3$ ligands, and it considerably increases film resistivity. Carbon incorporation is expected to be suppressed by using C-free PH_3 instead of $P(CH_3)_3$. Reducing C content will also be beneficial in improving the adhesion properties of Ru(P) with Cu. First principles calculations will be helpful in understanding the impact of C at the Ru/Cu interface on the adhesion strength. The influence of C on the microstructure of the Ru(P) alloy by first principles calculations and DOS analysis should also be examined.

In this work, XPS was used to determine the C content in the Ru(P) films. However, due to the overlapping between XPS C 1s and Ru $3d_{3/2}$ peaks and the vastly different sensitivity factors, fitting and calculation errors with C content is nearly inevitable, even with careful optimization of measurement and curve fitting process.

Many studies in the literatures ignore this problem, and it is recommended that a different method, like secondary ion mass spectroscopy (SIMS), be attempted. Although SIMS requires control experiments, it should be able to offer more accurate C concentration in the films.

First principle calculations suggest that B is more effective in amorphizing Ru than P, because less B is required. Considering that B is a safer material than P and a high purity B PVD target is available, PVD Ru(B) films should be able to be formed without much difficulty. Since PVD films have low C impurity levels and B content can be easily controlled in the PVD process, it can offer valuable information on the formation mechanism of amorphous Ru based alloys and on the first principles calculations.

Lastly, the usefulness of the computational analysis method should be noted. The computational power of workstations are increasing dramatically and continuously, and first principles calculations that require extensive calculations becomes less time consuming and more practical. Considering that computational power will continue to improve and semiconductor research is already at the atomic scale, the importance and usefulness of the computational analysis will keep increasing. Since data obtained by the calculations need to be carefully examined and verified by experimental results, experimental and computational approaches are complementary. Combining these two approaches should offer various advantages, and will be a powerful approach in exploring scientific problems.

Bibliography

T. Aaltonen, P. Alen, H. Ritala, M. Leskela, *Chem. Vap. Dep.* **9**, 45 (2003).

J. Basu, and S. Ranganathan, *Sandhana 28,* Parts 3 & 4, 783 (2003).

G. Bai, S. Wittenbrock, V. Ochoa, M. Bohr, *Mater. Res. Soc. Symp. Proc.* **403**, 501 (1996).

E. Belin, A. Traverse, A.Szasz, and F. Hachizaud, *J. Phys. F: Met. Phys.* **17**, 1913 (1987)

M. Birkholz, B. Selle, W. Fuhs, S. Christiansen, H. P. Strunk, and R. Reich, *Phys. Rev. B* **64**, 085402 (2001).

M. T. Bohr, *IEEE IEDM Tech. Dig.* 241 (1995).

D. Briggs and M. P. Seah, Practical Surface Analysis. Vol 1. Auger and X-ray Photoelectron Spectroscopy, John Wiley and Sons, Chichester, UK, 1990, p. 635.

R. Busch, *J. Mater.* **52**, 39 (2000).

E. Cartier, Y. Baer, M. Liard, and H. J. Guntherhodt, *J. Phys. F: Met. Phys.* **10**, L21 (1980).

R. Chan, T. N. Arunagiri, Y. Zhang, O. Chyan, R. M. Wallace, M. J. Kim, T. Q. Hurd, Electrochem. *Solid-State Lett.,* **7**, G154 (2004)

X. Chen, H. L. Frisch, A. E. Kaloyeros, and B. Arkles, *J. Vac. Sci. Technol. B* **16**, 2887 (1998)

W. Cheng, L. Hong, J. Jiang, Y. Chi, and C. Lin, *Thin Solid Films* **483**, 31 (2005).

V. B. Chernogorenko, V. G. Ivanchenko, and L. Ya. Kulik, in Binary Phase Diagrams, edited by. T. B. Massalski, H. Okamoto, P. R. Subramanian, and L. Kacprzak, (ASM

International, Materials, Park, OH 1990) p 2979.

O. Chyan, T. N. Arunagiri, and T. Ponnuswamy, *J. Electrochem. Soc.* **150**, C347 (2003).

M. Damayanti, T. Sritharan, Z. H. Gan, S. G. Mhaisalkar, N. Jian, and L. Chan, *J. Electrochem. Soc.* **153**, J41 (2006).

R. B. Diegle, N. R. Sorensen, C. R. Clayton, M. A. Helfand, and Y. C. Yu, *J. Electrochem. Soc.* **135**, 1085 (1988).

D. Duan, D. Xu, Q. Zhang, Q. Zhang, T. Cagin, W. L. Johnson, and W. A. Goddard III, *Phys. Rev. B* **71**, 224208 (2005).

T. Egami and Y. Waseda, *J. Non-Cryst. Solids* **64**, 113 (1984).

C. M. Eichfeld, M. A. Horsey, S. E. Mohney, A. V. Adedeji, and J. R. Williams, *Thin Solid Films* **485**, 207 (2005).

E. Eisenbraun, A. Upham, R. Dash, W. X. Zeng, J. Hoefnagels, S. Lane, D. Anjum, K. Dovidenko, A. Kaloyeros, B. Arkles, and J. J. Sullivan, *J. Vac. Sci. Technol. B* **18**, 2011 (2000).

P. Giauque and M. Nicolet, *J. Appl. Phys.* **93**, 4576 (2003).

I. Goswami and R. Laxman, *Semiconductor International* **27**, 49 (2004).

M. Green, M. Gross, L. Papa, K. Schnoes, and D. Brasen, *J. Electrochem. Soc.* **132**, 2677 (1985).

F. Q. Guo, S. J. Poon, and G. J. Shiflet, *J. Appl. Phys.* **97**, 013512 (2004).

Ch. Hausleitner and J. Hafner, *Phys. Rev. B* **47**, 5689 (1993).

K. Holloway, P. M. Fryer, C. Cabral, J. M. Harper, P. J. Bailey, K. H. Kelleher, *J. Appl.*

Phys. **71**, 5433 (1992).

J. E. Houston, P. J. Berlowitz, J. M. White, and D. W. Goodman, *J. Vac. Sci. Technol. A* **6**, 887 (1988).

C.-K. Hu, L. M. Gignac, E. Liniger, C. Detavernier, S. G. Malhotra, and A. Simon, *J. Appl. Phys.* **98**, 124501 (2005).

C.-K. Hu, L. Gignac, R. Rosenberg, E. Liniger, J. Rubino, C. Sambucetti, A. Domenicucci, X. Chen, and A. K. Stamper, *Appl. Phys. Lett.* **81**, 1782 (2002).

R. Hübner, M. Hecker, N. Mattern, A. Voss, J. Acker, V. Hoffmann, K. Wetzig, H. –J. Engelmann, E. Zschech, H. Heucer, and Ch. Wenzel, *Thin Solid Films* **468**, 183 (2004).

A. Inoue, N. Nishiyama, H. Kimura, *Mater. Trans. JIM* **38**, 179 (1997).

International Technology Roadmap for Semiconductors, 2006 Update, http://public.itrs.net (2006).

V. M. Jiménez, J. P. Espinós, and A. R. González-Elipe, Appl. Surf. Sci. **141**, 186 (1999).

Powder Diffraction File, Joint Committee on Powder Diffraction Standards, ASTM, Philadelphia, PA, 1967, Card 06-0663.

C-S., Jun, and T. P. Fehlner, *Chem. Mater.* **4**, 440 (1992).

A. E. Kaloyeros, X. Chen, K. Kumar, S. Seo, G. Peterson, H. Frisch, B. Arkles, and J. Sullivan, *J. Electrochem. Soc.* **146**, 170 (1999).

A. E. Kaloyeros and E. Eisenbraun, *Annu. Rev. Mater. Sci.* **30**, 363 (2000).

H. Kim, *J. Vac. Sci. Technol. B* **21**, 2231 (2003).

H. Kim, C. Cabral, Jr., C. Lavoie, and S. M. Rossnagel, *J. Vac. Sci. Technol. B* **20**, 1321

(2002).

H. Kim, C. Detavenier, O. van der Straten, S. M. Rossnagel, A. J. Kellock, and D. G. Park, *J. Appl. Phys.* **98**, 017308 (2005).

H. Kim, A. J. Kellock, and S. M. Rossnagel, *J. Appl. Phys.* **92**, 7080 (2002).

H. Kim, C. Lavoie, M. Copei, W. Narayanan, D. G. Park, and S. M. Rossnagel, *J. Appl. Phys.* **95**, 5848 (2004).

H. Kim, Y. Naito, T. Koseki, T. Ohba, T. Ohta, Y. Kojima, H. Sato, and Y. Shimogaki, *Jpn. J. Appl. Phys.* **45**, 2497 (2006).

S. Kim, S. Oh, H. Kim, D. Kang, K. Kim, W. Li, S. Haukka, and M. Tuominen, *J. Electrochem. Soc.* **151**, C272 (2004).

H. Kizil, and C. Steinbruchel, *Thin Solid Films* **449**, 158 (2004).

W. Klement, R. H. Willens, P. Duwez, *Nature* **187**, 869 (1960).

A. Kohn, M. Eizenberg, and Y. Shacham-Diamand, *Appl. Surf. Sci.* **212**, 367 (2003).

A. Kohn, M. Eizenberg, and Y. Sacham-Diamand, *J. Appl. Phys.* **94**, 3810 (2003).

A. Kohn, M. Eizenberg, and Y. Shacham-Diamand, B. Israel, and Y. Sverdlov, *Microelectron. Eng.* **55**, 297 (2001).

W. Kohlmann, and H. Werner, *Z. Naturforsch.* **48b**, 1499 (1993).

J. Kojnok, A. Szasz, W. Krasser, G. Mark, V. S. Stepanjuk, and A. A. Kastsnelson, *J. Phys.: Condens. Matter* **4**, 2487 (1992).

G.. Kresse, and J. Furthmüller, *Comput. Mater. Sci.* **6**, 15 (1996).

G.. Kresse, and J. Furthmüller, *Phys. Rev. B* **54**, 11169 (1996).

G.. Kresse, and J. Hafner, *Phys. Rev. B* **47**, 553 (1993).

M. Y. Kwak, D. H. Shin, T. W. Kang, and K. N. Kim, *Thin Solid Films* **339** 290 (1999).

O. Kwon, J. Kim, H. Park, and S. Kang, *J. Electrochem. Soc.* **151**, G109 (2004).

O. Kwon, S. Kwon, H. Park, and S. Kang, *J. Electrochem. Soc.* **151**, C753 (2004).

M. W. Lane, C. E. Murray, F. R. McFeely, P. M. Vereecken, and R. Rosenberg, *Appl. Phys. Lett.* **83**, 2330 (2003).

M. Lashdaf, T. Hatanpää, A. O. I. Krause, J. Lahtinen, M. Lindblad, and M. Tiitta, *Appl. Cata. A* **241**, 51 (2003).

Y. Lai, Y. Chen, Y. Chi, C. Liu, A. J. Carty, S. Peng, and G. Lee, *J. Mater. Chem.* **13**, 1999 (2003).

H.-J. Lee, T. Cagin, W. L. Johnson, and W. A. Goddard III, *J. Chem. Phys.* **119**, 9858 (2003).

H. Li, H. Li, W. Dai, W. Wang, Z. Fang, and J. Deng, *Appl. Sur. Sci.* **152**, 25 (1999).

J. Lin, and C. Lee, *J. Electrochem. Soc.* **146**, 3466 (1999).

Mass Spectra in NIST Chemistry Webbook, NIST Standard Database Number 69, Eds. P. J. Linstrom and W. G. Mallard, June 2005, NIST, Gaithersburg, MD 20899 (http://webbook.nist.gov).

T-M. Lu, and J. J. Senkevich, Worldwide Patten Application Number WO2004035858 (2004).

H. Ma, L. L. Shi, J. Xu, Y. Li, E. Ma, *Appl. Phys. Lett.* **87**, 181915 (2005).

S. Mader, *J. Vac. Sci. Technol.* **2**, 35 (1964).

N. Magen, A. Kolodny, U. Weiser, and N. Shamir, Proceedings of the 2004 international workshop on System level interconnect prediction, 7 (2004).

Y. Matsui, M. Hiratani, T. Nabatame, Y. Shimamoto, S. Kimura, *Electrochem. Solid-State Lett.* **5**, C18 (2002).

G. E. Moore, *Electronics* **38**, 114 (1965).

G. C. Nelson, *J. Appl. Phys.* **47**, 1253 (1976).

H. Ohring, Materials Science of Thin Films, 2nd ed. Academic Press, San Diego, CA 2002.

T. Oku, E. Kawakami, M. Uekubo, K. Takahiro, S. Yamaguchi, and M. Murakami, *Appl. Surf. Sci.* **99**, 265 (1996).

N. Oshima, T. Shibutami, K. Kawano, S. Yokoyama, and H. Funakubo, *Electrochemical Society Proceedings* **28**, 277 (2002).

W. Ostwald, *Z. Phys. Chem.* **22**, 306 (1897)

E. J. O'Sullivan, A. G. Schrott, M. Paunovic, C. J. Sambucetti, J. R. Marino, P. J. Baily, S. Kaja, and K. W. Semkow, *IBM J. Res. Dev.* **42**, 607 (1998).

A. Peker and W. L. Johnson, *Appl. Phys Lett.* **63**, 2342 (1993).

J. P. Perdew, J. A. Chevary, S. H. Vosko, K. A. Jackson, M. R. Pederson, D. J. Singh, and C. Fiolhais, *Phys. Rev. B* **46**, 6671 (1992).

L. Peters, *Semiconductor International* **21**, 64 (1998).

J. L. Pinney, *Proc. R. Soc. A* **319**, 479 (1970).

Y. Qi, T. Cagin, Y. Kimura, and W. A. Goddard III, *Phys. Rev. B* **59**, 3527 (1999).

G. B. Raupp and T. S. Cale, *Chem. Mater.* **1**, 207 (1989).

S. K. Rha, W. J. Lee, S. Y. Lee, Y. S. Hwang, Y. J. Lee, D. I. Kim, D. W. Kim, S. S. Chun, and C. O. Park, *Thin Solid Films* **320**, 134 (1998).

S. M. Rossnagel and H. Kim, *Proceedings of the IEEE 2001 International Interconnect Technology Conference* 3 (2001)

S. M. Rossnagel, Solid State Technology, February 2005 Exclusive online feature#1: Deposition, www.solid-state.com 01 – 04 (2005).

H. Schmidbauer, and G. Blaschke, *Z. Naturforsh.* **35b**, 584 (1980).

J. Schroers and W. L. Johnson, *Appl. Phys. Lett.* **84**, 3666 (2004).

O. N. Senkov, and D. B. Miracle, *Mater. Res. Bull.* **36**, 2183 (2001).

H. W. Sheng, W. K. Luo, F. M. Alamgir, J. M. Bai, and E. Ma, *Nature* **439**, 419 (2006).

T. Shibutami, K. Kawano, N. Oshima, S. Yokoyama, and H. Funakubo, *Electrochem. Solid-State Lett.* **6**, C117 (2003).

J. Shin, D. Gay, Y-M. Sun, J.M. White, J.G. Ekerdt, in: D.G. Seiler, A.C. Diebold, R. McDonald, .R. Ayre, R.P. Khosla, S. Zollner, E.M. Secula (Eds.), *AIP Conf. Proc.* **788**, 482 (2005).

J. Shin, H-W. Kim, G. S. Hwang, J. G. Ekerdt, *Surf. Coat. Technol.* **201**, 9256 (2007).

J. Shin, A. Waheed, K. Agapiou, W. A. Winkenwerder, H-W. Kim, R. A. Jones, G. S. Hwang, and J. G. Ekerdt, *J. Amer. Chem. Soc.* **128**, 16510 (2006).

J. Shin, A. Waheed, W. A. Winkenwerder, H-W. Kim, R. A. Jones, G. S. Hwang, and J. G.

Ekerdt, *Thin Solid Films,* **515**, 5298 (2007).

H. W. Sheng, W. K. Luo, F. M. Alamgir, J. M. Bai, and E. Ma, *Nature* **439**, 419 (2006).

P. Shewmon, Diffusion in Solids, 2nd ed. The Minerals, Metals, and Materials Society, Warrendale, PA 1989.

H. Simka, S. Shankar, C. Duran, and M. Harverty, *Mater. Res. Soc. Symp. Proc.* **863**, 283 (2005).

H. L. Skriver, N. M. Rosengaard, *Phys. Rev. B* **46**, 7157 (1992).

P. Staszczuk, B. Janczuk, and E. Chibowski, Mater. *Chem. Phys* **12**, 469 (1985).

I. N. Stranski and D. Totomanow, *Z. Phys, Chem.* A**168**, 399 (1933).

O. Straten, Y. Zhu, J. Rullan, K. Dunn, and K. E. Kaloyeros, *J. Mater. Res.* **21**, 255 (2006).

Y-M. Sun, S. Y. Lee, A. M. Lemonds, E. R. Engbrecht, S. Veldman, J. Lozano, J. M. White, J. G. Ekerdt, I. Emesh, and K. Pfeifer, *Thin Solid Films* **397**, 109 (2001).

J. Tan, X. Qu, Q. Xie, Y. Zhou, and G. Ru, *Thin Solid Films* **504**, 231 (2006).

H.-S. Tao, U. Diebold, N. D. Shinn, and T. E. Madey, *Surf. Sci.* **375**, 257 (1997)

S. Tougaard, *Vac. Sci. Technol. A* **14**, 1415 (1996).

M. Traving, G. Schindler, G. Steinlesberger, W. Steinhoegl, M. Engelhardt, *Semiconductor International* **26**, 73 (2003).

K. N. Tu, J. W. Mayer, L. C. Feldman, Electronic Thin Film Science, Mcmillian, New York, 1992, p. 246.

K. N. Tu, S. R. Herd, and U. Gösele, *Phys. Rev. B* **43**, 1198 (1991).

I. E. Wach, Characterization of Catalytic Materials, Boston, Butterworth-Heinemann, 1992, pp 172.

C. D. Wagner, L. E. Davis, M. V. Zeller, J. A. Taylor, R. H. Raymond, and L. H. Gale, *Surf. Interface Anal.* **3**, 211 (1981).

D. Wang, U. Geyer, and S. Schneider, *J. Non-Cryst. Solids* **221**, 222 (1997).

H. Wang, A. Tiwari, X. Zhang, A. Kvit, and J. Narayan, *Appl. Phys. Lett.* **81**, 1453 (2002).

Q. Wang, J. G. Ekerdt, D. Gay, Y. Sun, J. M. White, *Appl. Phys. Lett.* **84**, 1380 (2004).

Y. H. Wang, M. R. Moitreyee, R. Kumar, L. Shen, K. Y. Zeng, J. W. Chai, and J. S. Pan, *Thin Solid Films* **460**, 211 (2004).

L. Xia, S. S. Fang, Q, Wang, Y. D. Dong, and C. T. Liu, *Appl. Phys. Lett.* **88**, 171905 (2006).

P. Xu, K. Huang, A. Patel, S. Rathi, B. Tang, J. Ferguson, J. Huang, C. Ngai, and M. Laboda, Proceedings of the IEEE 1999 International Interconnect Technology Conference, 109 (1999).

Z. L. Yuan, D.H. Zhang, C.Y. Li, K. Prasad, C.M. Tan, and L.J. Tang, *Thin Solid Films* **434**, 126, 2003.

F. Yubero, A. R. González-Elipe, and S. Tougaard, *Surf. Sci.* **457**, 24 (2000).

Vita

Jinhong Shin was born in Seoul, Korea, on August 12th, 1972, the son of Samkyu Shin and Sookja Yoon. He graduated Sehwa high school in Seoul, Korea, in February 1991. He earned his Bachelor of Science degree in Ceramic Engineering from Yonsei University, Seoul, Korea, in February 1995. He joined Dr. Kihyun Yoon's lab in 1995, and earned his Master's degree from Yonsei University in February 1997. The title of his thesis was "Photoelectrochemical properties of textured *n*-WO_3/*p*-Si electrodes".

After graduating from Yonsei University, he started working for Hynix Semiconductor Inc. (formerly named Hyundai Electronics) from 1997 to 2003. From 1997 to 2001, he worked as a process development engineer in the System IC Research Center. He was responsible for developing and qualifying etch and cleaning processes for gate spacer, metal contact, and via for 0.5 – 0.13 μm node VLSI devices. He was assigned to International SEMATECH, Austin, TX, as a project engineer from 2002 to 2003, and worked on plasma etch process development for up to 90 nm node dual damascene structures with Cu and porous ultra low-k dielectrics.

Jinhong started his doctoral study at the University of Texas at Austin in January 2004 under the supervision of Dr. John G. Ekerdt. His research focuses on growing and characterizing ultrathin Ru and Ru based amorphous alloy films for the liner application in Cu interconnect for sub 32 nm devices. His research was supported by the Advanced

Materials Research Center, the National Science Foundation, and the Semiconductor Research Corporation.

Jinhong authored or coauthored nine publications submitted to refereed journals. Research results during the doctoral study were presented at the AIChE Annual Meeting in Austin, TX in November 2004, SRC-CAIST Annual Review Meetings in Albany, NY in October 2005, the 7th International Conference on Microelectronics and Interfaces in Austin, TX in March 2006, SRC-CAIST Annual Review Meetings in Albany, NY in October 2006, Spring MRS Conference in San Francisco, CA in April 2007, SRC TECHCON in Austin, TX in September 2007, the 54th American Vacuum Society International Symposium in Seattle, WA in October 2007.

Jinhong has accepted a position with Intel Corporation.

Permanent address: 12100 Metric Blvd #925, Austin, TX 78758

This dissertation was typed be the author.